UNIVERSITÀ DEGLI STUDI DI MILANO

PhD degree in Medical Nanotechnology (ciclo 28)

European School of Molecular Medicine (SEMM)

Settore disciplinare: FIS/03

An innovative strategy for adipose tissue reconstruction

Eleonora Rossi

Matricola n. R10344

SUPERVISOR: Prof.ssa Cristina Lenardi

University of Milan, Milan

Anno accademico 2015-2016

An innovative strategy for adipose tissue reconstruction

Eleonora Rossi

Ph.D. thesis in Medical Nanotechnology

European School of Molecular Medicine, Milan, Italy

Università Degli Studi Di Milano, Milan, Italy

October 2016

Supervisor: CRISTINA LENARDI

Internal Co-supervisor: PAOLO MILANI

External Co-supervisor: IVAN MARTIN

The research in this thesis was carried out from November 2012 until January 2015 in the research group Advanced Biomaterials of Fondazione Filarete for Biosciences and Innovation in collaboration with The Interdisciplinary Centre for Nanostructured Materials and Interfaces (CIMAINA) of the University of Milan. From February 2015 until October 2016 the research was carried out in the Department of Biomedicine at the University Hospital of Basel, Switzerland.

ABSTRACT

Despite clinical treatments for adipose tissue defects, in particular breast tissue reconstruction, have certain grades of efficacy, many drawbacks are still affecting the long-term survival of new formed fat tissue. To overcome this problem, in the last decades, several scaffolding materials have been investigated in the field of adipose tissue engineering. However, a strategy able to recapitulate a suitable environment for adipose tissue reconstruction and maintenance is still missing.

Synthetic polymers gather a series of advantages because they can be chemically modified obtaining hydrogels with desired biochemical, mechanical and degradation properties. Among the synthetic class of polymer, poly(amidoamine)s (PAAs) based hydrogels, containing the 2,2-bisacrylamidoacetic acid-agmatine monomeric unit, are known to have promising biological properties because they can enhance cellular adhesion by interacting with the arginine-glycine-aspartate (RGD)-binding motif of integrins. In this thesis, we first exploited the potential of RGD-mimetic PAA based hydrogels for the establishment of three dimensional (3D) cell culture systems with tunable mechanical and degradation properties. We presented two different approaches for the fabrication of PAA based hydrogels. In the first approach, we copolymerized the PAA oligomers (OPAA) with poly(ethylene glycol) (PEG) to fabricate hydrogels with improved biological, mechanical and optical transparency properties. In the second approach, a synthetic polymeric precursor for cell encapsulation was realized with the aim to combine, by grafting, the adhesive properties of PAAs with the good mechanical integrity of poly(2-hydrox-yethyl)methacrylate (PHEMA) based hydrogels. We demonstrated that with our approaches it is possible to tune the mechanical properties of our hydrogels keeping the adhesive properties typical of pure PAA and providing a tunable platform for 3D cell culture.

Once evaluated the PAA potential to support 3D cell culture, we adopted a biologically and mechanically driven design to fabricate OPAAs macroporous foam (OPAAF) for adipose tissue reconstruction. The scaffold was designed to fulfil three fundamental criteria: capability to induce cell adhesion and proliferation, support of *in vivo* vascularization and match of native tissue mechanical properties. OPAAs were formed into soft scaffolds with hierarchical porosity through a combined free radical polymerization and foaming reaction. OPAAF is characterized by a high water uptake capacity, progressive degradation

kinetics and ideal mechanical properties for adipose tissue reconstruction. Furthermore, OPAAF supported cell adhesion, proliferation and adipogenesis *in vitro* together with adipose tissue and vessels infiltration *in vivo*.

ECM is known to be the ideal scaffold for tissue engineering application. In the detail, decellularized adipose tissue proved to have an adipoinuctive effect on adipose stromal cells. Therefore we decided to further implement the biological properties of the OPAAF by decoration with a devitalized adipose tissue matrix.

We first optimized a protocol for the 3D adipogenic differentiation of human primary cells *in vitro* using a perfusion bioreactor system. The OPAAF efficiently supported human adipose stromal cells (hASCs) differentiation into mature adipocytes. We then decorated the OPAAF with engineered devitalized adipose tissue matrix deposited by hASCs. Two different protocols have been adopted for the decoration, in order to investigate the role of a differentiated and stromal matrix in adipogenic induction. With our approach we efficiently generated hybrid scaffolds combining the positive features of both synthetic and natural biomaterials. The obtained hybrid constructs showed to have an adipoinductive effect on hASCs in absence of any growth factor *in vitro* and promoted adipogenesis *in vivo*.

Overall, these results proved that our approach can provide an alternative strategy for adipose tissue reconstruction based on the use of patients cells for the generation of custom made hybrid scaffolds. The engineered adipose tissue could also serve as a 3D model of fat tissue at different stages of differentiation with potential use in drug testing.

Figures index vii

Abbreviation list ix

1 General introduction 1

1.1 Adipose Tissue 1

1.1.1 Treatment of adipose tissue defects 5

1.2 Tissue Engineering Paradigm 6

1.2.1 The ideal scaffold for adipose tissue engineering 7

1.3 Aim of the study and outline 9

1.4 References 10

2 RGD-mimetic poly(amidoamine) based hydrogels with tunable mechanical and degradation properties for the fabrication of cell laden constructs 15

2.1 Introduction 15

2.1.1 PAA-Jeffamine®-PAA triblock copolymer (PJP) 17

2.1.2 PAA based grafting of non-adhesive synthetic polymer 18

2.2 Materials and methods for PJP 18

2.2.1 Materials 18

2.2.2 Glass slides silanization and mold fabrication 19

2.2.3 PAA oligomer (OPAA) synthesis 19

2.2.4 PJP oligomer synthesis 20

2.2.5 Hydrogels fabrication and characterization 20

2.2.6 Degradation test 21

2.2.7 Cell culture 22

2.2.8 2D cell culture on hydrogel discs 22

2.2.9 Cell attachment/spreading assay 22

2.2.10 Fluorescent staining 22

2.2.11 Cell encapsulation 23

2.2.12 Statistical analysis 23

2.3 Materials and methods for PAA based grafting of non-adhesive synthetic polymer 23

2.3.1 Materials 23

2.3.2 Syntheses 24

2.3.3 Size Exclusion Chromatography (SEC) and NMR Spectroscopy 25

2.3.4 Hydrogels Preparation 26

2.3.5 Degradation Tests 26

2.3.6 Compression Tests 26

2.3.7 In vitro 3D Cell Culture 27

2.4 Results and Discussion for PJP 28

2.4.1 Hydrogel preparation 28

2.4.2 Optical properties 28

2.4.3 Mechanical properties 29

2.4.4 Swelling and degradation characteristics 30

2.4.5 NIH 3T3 cell adhesion to 2D PJP surfaces 31

2.4.6 HUVECs cell adhesion to 2D PJP surfaces 32

2.4.7 3D cell encapsulation in PJP-4 33

2.4.8 Conclusions 34

2.5 Results and Discussion for PAA based grafting of non-adhesive synthetic polymer 35

2.5.1 Syntheses of the Comb-Like Polymers: P(HEMA-CO-APM)/PAAs 35
2.5.2 Mechanical Properties 36
2.5.3 Degradation Kinetics 38
2.5.4 *In vitro* 3D Cell Culture 39
2.5.5 Conclusions 40
2.6 Summary 41
2.7 References 41

3 Biologically and mechanically driven design of an RGD-mimetic Macroporous Foam for Adipose Tissue Engineering Applications 48
3.1 Introduction 48
3.2 Materials and Methods 51
3.2.1 Materials 51
3.2.2 Synthesis of diacrylamide-terminated poly(amidoamine)s oligomer OPAA 51
3.2.3 OPAAF fabrication 51
3.2.4 Scanning electron microscopy 52
3.2.5 Size Exclusion Chromatography 52
3.2.6 Nuclear magnetic resonance NMR 52
3.2.7 Equilibrium swelling and weight loss measurements 52
3.2.8 Mechanical characterization 53
3.2.9 Cell culture and seeding 53
3.2.10 Live/Dead assay 54
3.2.11 BODIPY staining 54
3.2.12 Gene expression analysis 55
3.2.13 In vivo biocompatibility, adipose and vascular tissue infiltration 55
3.2.14 Statistical analysis 56
3.3 Results 56
3.3.1 OPAAF synthesis and morphology 56
3.3.2 Swelling Capacity and Degradation Kinetics 57
3.3.3 Mechanical properties 58
3.3.4 In vitro evaluation of cells adhesion, viability and adipogenesis 60
3.3.5 In vivo biocompatibility, adipose and vascular tissue infiltration 64
3.4 Discussion 67
3.5 Conclusion 70
3.6 References 71

4 Decoration of RGD-mimetic porous scaffold with engineered devitalized adipose matrix 77
4.1 Introduction 77
4.2 Materials and Methods 78
4.2.1 OPAA Syntheses and OPAAF Fabrication 78
4.2.2 Cell source and expansion 79
4.2.3 Generation of decellularized Hybrid ECM-OPAAF 79
4.2.4 Evaluation of hASCs-OPAAF interaction in vitro 80
4.2.5 ECM characterization 81
4.2.6 Gene expression analysis 81
4.2.7 In vivo implantation 82
4.3 Results 82
4.3.1 In vitro Evaluation of cell-polymer interaction 82
4.3.2 In vitro adipogenesis 84
4.3.3 OPAAF decoration and generation of decellularized hybrid ECM-OPAAF 84

4.3.4 In vitro evaluation of the adipoinductive potential of the hybrids ECM-OPAAF 88
4.3.5 In vivo evaluation of the adipoinductive potential of the hybrid constructs . 89
4.4 Discussion 90
4.5 Conclusion 92
4.6 References 93

5 Conclusion and future perspectives 97

6 A 3D in vitro bone model for the investigation of the role of triggering receptor expressed on myeloid cells 2 (TREM-2) in bone homeostasis 99
6.1 Introduction 99
6.2 Materials and Methods 101
6.2.1 Cell source and expansion 101
6.2.2 Peripheral blood derived CD14+ monocytes 101
6.2.3 3D co-culture system 101
6.2.4 In vitro functionality of the 3D co-culture system 102
6.2.5 Stimulation with TREM-2 agonist 103
6.2.6 Statistical analyses 103
6.3 Results 103
6.3.1 Establishment of the 3D co-culture system 103
6.3.2 Evaluation of osteoclast differentiation and TREM-2 monitoring 105
6.3.3 Assessment of ECM turnover using non-invasive tools 106
6.3.4 3D co-culture stimulation with TREM-2 agonist 107
6.4 Discussion 108
6.5 Conclusion 109
6.6 References 109

FIGURES INDEX

Figure 1-1 Determination of adipocytes fate from mesenchymal precursors 3
Figure 1-2 Schematic representation of the players involved in the different steps of adipogenesis. 4
Figure 1-3 Sketch of a lobule of adipose tissue 4
Figure 2-1 Synthetic scheme of the triblock diacrylamido-terminated (PJP) oligomer 29
Figure 2-2 Degradation curves of 15% (w/v) PJP-4 and OPAA-2 hydrogels. Storage modulus of 15% (w/v) OPAA-2 and PJP-4 hydrogels obtained by DMA in unconfined compression at different solicitation frequencies. 31
Figure 2-3 Cell proliferation values of NIH 3T3 cells cultured for 48 h on hydrogels using glass slide as a control 32
Figure 2-4 Cell proliferation of HUVECs cultured for 48 h on PJP-4 hydrogels at different concentrations. Confocal microscopy images of HUVECs morphology on PJP-4 33
Figure 2-5 Characterization of encapsulated cell behaviour. NIH 3T3 fibroblasts embedded in PJP-4 at 7.5%, 10%, 15% (w/v) and in agarose. Quantification of encapsulated cells viability for different PJP-4 concentration, at 48 h compared to AGAR. 34
Figure 2-6 Synthetic route for the preparation of P(HEMA-co-APM)/PAA 36
Figure 2-7 Compression elastic modulus of P(HEMA-co-APM)/PAA and PAAdiAc hydrogels 38
Figure 2-8 Degradation kinetics of the P(HEMA-co-APM)/PAA hydrogels 39
Figure 2-9 Confocal microscopy images, live/dead assay for 3T3-NIH fibroblasts 48 h after encapsulation in different hydrogels substrates 40
Figure 3-1 Schematic representation of OPAA synthesis and OPAAF fabrication 57
Figure 3-2 OPAAF structural and chemico-physical characterization. SEM micrographs of OPAAF. Swelling and degradation kinetics of OPAAF in PBS 1X at 37°C. Mechanical characterization of OPAAF. Representative Stress vs Time curve during compression test in controlled strain; Table with Young's Moduli at different level of strain 58
Figure 3-3 Dynamic mechanical analysis. Representative Stress vs Time curve and table with Dynamic, Storage, Loss moduli and Tanδ respectively at 0.1Hz, 1Hz and 5Hz. 60
Figure 3-4 MDCK and 3T3L1 cells viability. Confocal microscope images, live/dead assay for MDCKs and 3T3L1s seeded on OPAAF after 1, 3 and 9 days of culture 62
Figure 3-5 3T3L1 adipogenic differentiation. Confocal microscope images, BODIPY/DAPI staining for 3T3L1s during the adipogenic differentiation protocol. qRT-PCR analysis for PPARγ during the adipogenic differentiation 63
Figure 3-6 HUVEC cells viability. Confocal microscope images, live/dead assay for HUVECs seeded on OPAAF after 1, 3 and 9 days of culture 64
Figure 3-7 Histological examination of OPAAF at 14 and 50 days after implantation. H&E staining and immunoperoxidase staining for anti-Iba1, and CD31 66
Figure 3-8 Host vessels infiltration at 50 days after implantation. Immunofluorescent and H&E images for blood vessels 67
Figure 4-1 In vitro 3D model for adipose tissue generation. Schematic representation of the perfusion culture system. Live/dead staining for cells viability 1 week after culture in proliferation medium. IF analysis for actin, vinculin and nuclei 1 week after culture in proliferation medium. BODIPY/DAPI staining for FA after the adipogenic differentiation protocol. qRT-PCR analysis for PPARg and FABP4 after the differentiation protocol 83
Figure 4-2 Schematic representation of the decoration protocols 85
Figure 4-3 SEM analysis of the decorated constructs. Adipogenic and stromal constructs before and after devitalization 86
Figure 4-4 IF analysis for the ECM proteins. Adipogenic constructs IF analysis for collagen IV and laminin before and after decellularization. Stromal constructs IF analysis for fibronectin before and after decellularization 87
Figure 4-5 Quantitative analysis of ECM composition for Adipo-OPAAF and Stromal-OPAAF. Luminex analysis for collagen IV and ELISA analysis for collagen 1A1, fibronectin and laminin 87

Figure 4-6 In vitro adipoinductive potential of hybrids ECM-OPAAF. Schematic representation of culture protocol. BODIPY/Actin/DAPI staining for OPAAF, Adipo-OPAAF and Stromal-OPAAF. qRT-PCR analysis for PPARg, CEBPA and FABP4 89
Figure 4-7 In vivo adipoinductive potential of hybrids ECM-OPAAF. H&E staining for OPAAF, Adipo-OPAAF and Stromal-OPAAF one month after implantation. 90
Figure 6-1 3D co-culture system. hBMCs seeding and differentiation in osteogenic medium. CD14+ cells seeding and differentiation in osteoclastogenic medium on the osteogenic construct. 104
Figure 6-2 Histological analysis for ECM deposition. H&E staining for the monoculture with hBMCs and for the co-culture over time 105
Figure 6-3 Histological analysis for osteogenic construct. Alizarin red staining for the monoculture with hBMCs and for the co-culture over time. BSP immunohistochemistry for the monoculture and for the co-culture 105
Figure 6-4 Analysis of OCs differentiation and TREM-2 levels. TRAP staining for OCs activity over time. TREM-2 FACS analysis at 1 and 2 weeks of co-culture 106
Figure 6-5 ECM turnover in the co-culture system 107
Figure 6-6 ECM turnover after stimulation with the agonist. 108

ABBREVIATION LIST

WAT: white adipose tissue

BAT: brown adipose tissue

TNF-α: tumour necrosis factor α

ECM: extracellular matrix

PPARg: peroxisome proliferator-activated receptor gamma

CEBPs: CCAAT/enhancer-binding proteins

FABP4: fatty acid-binding protein 4

GLUT4: glucose transporter

TG: triglyceride

hASCs: human Adult Sromal Cells

MSCs: mesenchymal stem cells

RGD: arginine-glycine-aspartate

PAA: poly(amidoamine)

OPAA: poly(amidoamine) oligomer

OPAAF: poly(amidoamine)s oligomers foam

TREM-2: transmembrane receptor expressed on myeloid cells 2

sTREM-2: shed TREM-2

AD: Alzheimer Disease

3D: three-dimensional

PEG: poly(ethylene glycol)

PHEMA: poly(2-hydrox-yethyl)methacrylate

ABG: 4-aminobutylguanidine

BAC: bisacrylamidoacetic acid

P(HEMA-co-APM): poly((2-hydroxyethyl)methacrylate-co-(3-aminopropyl)methacrylamide)

DMA: Dynamic mechanical analysis

BD: branching degree

MDCK: Madin-Darby canine kidney

HUVEC: Human Vein Endothelial cell

GAPDH: glyceraldehyde-3-phosphate dehydrogenase

H&E: haematoxylin and eosin

IF: immunofluorescence

IHC: immunohistochemistry

OC: osteoclast

OB: osteoblast

hBMC: human bone marrow cell

CICP: C-terminus procollagen type I

NTx-I: crosslinked N-telopeptides of collagen type I (both from TecoMedical

TRAP5b: tartrate-resistant acid phosphatase isoform 5

CHAPTER 1

1 GENERAL INTRODUCTION

Eleonora Rossi [a,b]

a) SEMM, European School of Molecular Medicine, Campus IFOM-IEO, Via Adamello 16, 20139 Milano, Italy. b) Department of Biomedicine, University Hospital of Basel, Hebelstrasse 20, 4031 Basel, Switzerland.

1.1 ADIPOSE TISSUE

The adipose tissue is an important metabolic organ composed of two different tissues, namely the white and brown adipose tissue (WAT and BAT, respectively). The WAT is the predominant type of fat in adult humans and serves as storage depot for excess energy, while the BAT generates heat in newborns via mitochondrial uncoupling of lipid oxidation (1). The WAT also secretes autocrine and paracrine factors that play an active role in regulating whole body metabolism and homeostasis. Most famous among these factors is leptin, an adipocyte-derived hormone that acts in the hypothalamus to decrease food intake and increase energy expenditure, and in peripheral tissues to affect metabolism and other cellular functions. Apart from leptin, many other factors, such as resistin, tumour necrosis factor α (TNF-α), adiponectin and angiotensinogen, are produced by fat cells and are proposed to regulate energy homeostasis (2-4).

The adipose tissue is distributed throughout the body and can be categorized by type and depot in subcutaneous, intra abdominal, and other sites (5). The adipose tissue parenchyma is predominantly composed of mature adipocytes containing large lipid droplets, in addition to stromal-vascular cells such as preadipocytes, interstitial cells, endothelial cells, and pericytes (6). The adipose tissue also contains an extensive system of blood vessels, lymph nodes, and nerves supported within an extracellular matrix (ECM)(7).

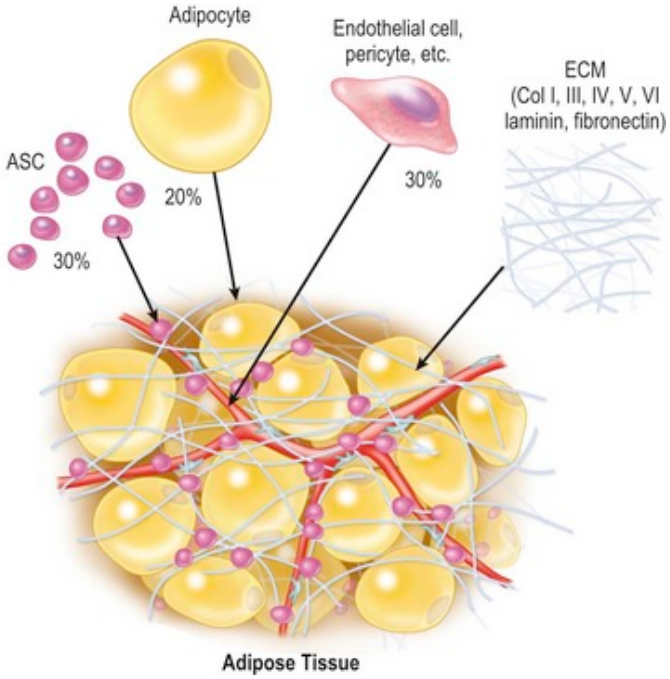

Figure 1-1 Schematic representation of adipose tissue composition (54).

During adipogenesis stem cells become fibroblast-like preadipocytes loosing the ability to differentiate into other mesenchymal lineages (such as myocytes, chondrocytes or osteocytes) and thus become committed to the adipocytes lineage differentiating into lipid-laden and insulin-responsive adipocytes (8). This process occurs in several stages and involves a cascade of transcriptional factors, among which peroxisome proliferator-activated receptor gamma (PPARg) and CCAAT/enhancer-binding proteins (CEBPs) are considered the crucial determinants of adipocytes fate (8). The differentiation is initiated upon inhibition of both Wnt and Hedgehog (Hh) signaling and the activation of PPARg and CEBPa (Figure 1-2)(9). PPARg is both necessary and sufficient for adipocyte differentiation and, to date, no factor has been identified that can rescue adipogenesis in absence of PPARg (10). CEBPa is induced late in adipogenesis and is most abundant in mature adipocytes, where it is crucial for insulin-dependent glucose uptake (11).

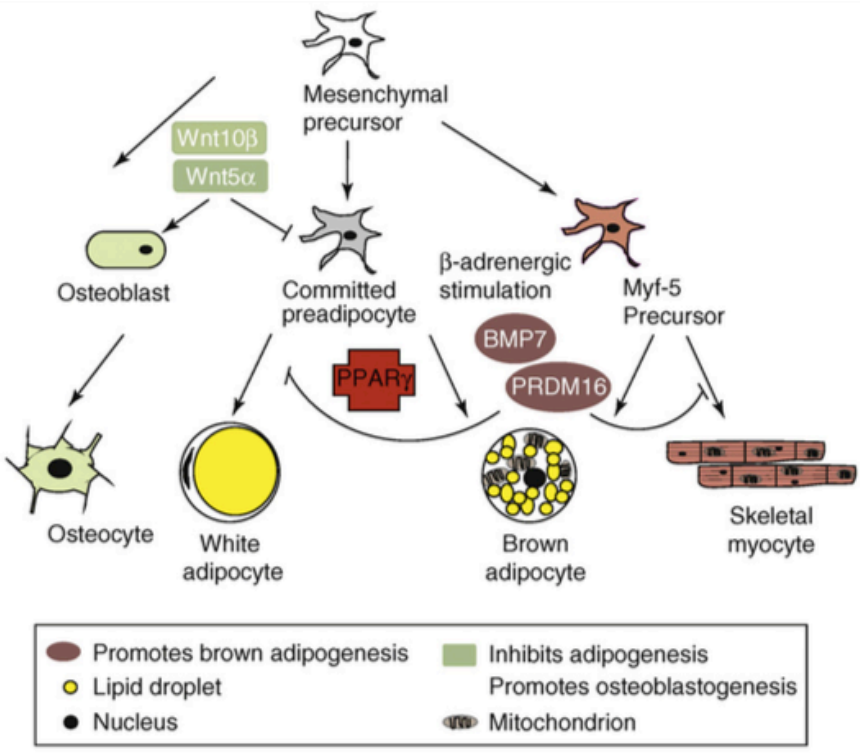

Figure 1-2 Determination of adipocytes fate from mesenchymal precursors (12).

There are two types of adipocytes, which have distinct morphology and function: white adipocytes, which store triglycerides in a single large lipid droplet, and brown adipocytes, which have multiple small lipid droplets and are rich in mitochondria. Brown and white adipocytes can originate from different precursors (Figure 1-1)(12).

Once preadipocytes have committed to the adipogenesis programme, a transcriptional cascade is activated that induces the expression of metabolic genes and adipokines associated with the adipocyte phenotype, such as fatty acid-binding protein 4 (FABP4), glucose transporter 4 (GLUT4), leptin and adiponectin; this is known as the terminal differentiation stage (13). After this stage, triglyceride (TG) synthesis occurs, causing mature adipokines to be secreted and ECM production (Figure 1-2).

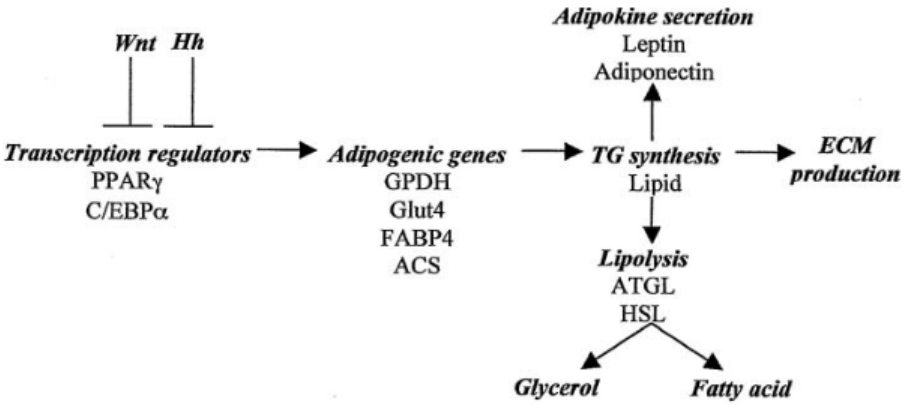

Figure 1-3 Schematic representation of the players involved in the different steps of adipogenesis (14).

Mature adipocytes are supported externally by two collagen-based structures: a collagen mesh which surrounds each adipocyte, termed reinforced basement membrane, and a predominantly type I collagen fibre network termed the interlobular septa (15). Mature adipocytes are arranged within lobules of diameter about 1 mm. Each adipocyte is in contact with at least one capillary and is entirely surrounded by reinforced basement membrane, a woven filamentous collagenous structure (15). This structure can be divided in two distinct regions of collagen, a basement membrane of sheet-like type IV collagen adjacent to the phospholipid membrane of the adipocyte (16), and an outer sheath of fibrillar collagen (Figure 1-4)(17).

In general, the ECM of the adipose tssue is composed of collagen types I, III, IV, V, and VI and other ECM proteins such as laminin and fibronectin (8, 15).

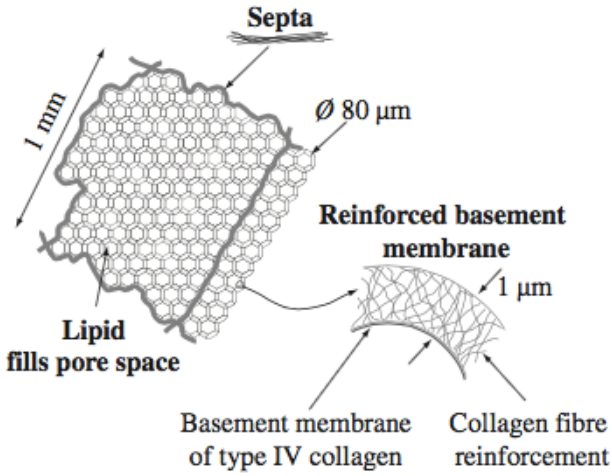

Figure 1-4 Sketch of a lobule of adipose tissue (15).

ECM proteins play a pivotal role in adipose tissues regulating mechanical

properties, adipogenesis and lipid droplets growth (18). During adipocyte differentiation, cells convert from a fibroblastic to a spherical shape, and dramatic changes occur in cell morphology, cytoskeletal components, and the level and type of ECM components (8,18). Therefore, maintaining a high degree of flexibility of the ECM allows a physiological expansion of the adipose tissue, without adverse metabolic consequences.

Since the function of the ECM depends tightly on its molecular assembly, it is important to know which components are involved in the formation of adipose ECM. Studies indicate that collagen V and collagen VI are essential for proper adipogenesis and that disruption of collagens impairs triglyceride storage during adipocyte differentiation (18). Fibronectin and collagens are the most abundant proteins of interstitial fibers and pericellular basement membranes in adipose tissue. Among these components, type I collagens provide the major ECM framework necessary to sustain the structure and function of mesenchymal tissues (18).

1.1.1 Treatment of adipose tissue defects

Adipose tissue replacement is often required after trauma, congenital abnormalities, and especially after tumour resection in patients affected by breast cancer (14). Current techniques for the treatment of adipose tissue defects, especially for breast reconstruction, are mainly relying on the use of synthetic prosthesis or autologous reconstruction (19). Breast implants have been used for years in plastic surgery but are still hampered by a series of drawbacks such as rupture, capsule contracture and their incompatibility with radiotherapy (19-21). On the other hand, autologous fat reconstruction is a promising technique that sought to provide a more aesthetic and natural alternative using adipose tissue from patients (19). In this field, we can distinguish between the flap reconstruction and the fat grafting or lipofilling. In the flap-reconstruction a huge mass of adipose tissue is transplanted from one site to another, with or without its vascular supply. Although this technique remains the gold standard, it is a costly surgical procedure with lengthy operative time and the need of microsurgical expertise (22). Moreover, the flap reconstruction can carry significant donor-site morbidity together with necrosis of the implant due to the lack of vascular supply (23, 24). On the other hand, fat grafting has the advantage of using the patient's own tissue with minimal donor-site morbidity and eliminating the issues of

foreign body reaction or rejection associated with synthetic implants. This new technique relies on the detection and use of Adult Sromal Cells (ASCs) in adipose tissue and has been widely used in breast reconstruction especially after tumour resection (25). Indeed, ASCs are mesenchymal stem cells (MSCs) with multipotency of differentiation (26) that can be easily retrieved from adult adipose tissue.

Unfortunately, despite the widespread use of autologous fat grafting in both reconstructive and cosmetic surgery, volume retention remains a significant problem (9, 27). Indeed, long term follow up studies revealed a 20-70% volume loss after fat grafting mainly because of the lack of vascular supply that underpins resorption (28). Due to the abovementioned issues, there is increasing interest in the use of tissue-engineered autologous solutions for breast defects following oncologic resection (27, 29).

1.2 TISSUE ENGINEERING PARADIGM

Tissue engineering is a multidisciplinary field combining the knowledge of biology, engineering and biomaterials science and aiming at replacing in function and volume damaged or lost human tissue (30). Current tissue engineering approaches include: i) the use of cells isolated from the patient and then injected in a desired location of the body; ii) the design of biomimetic scaffolding material to be injected or implanted in the patient; iii) their combination to create *in vitro* functional tissues to be used as transplants or *in vitro* test systems (30-32). Typically, cells are firstly isolated from the patient and subsequently expanded *in-vitro*. When the sufficient amount of cells is reached, they are seeded and cultured on a scaffold in a controlled culture environment. Once the construct become mature, it is implanted in the desired site of the patient's body to complete the tissue regeneration (Figure 1-5)(32).

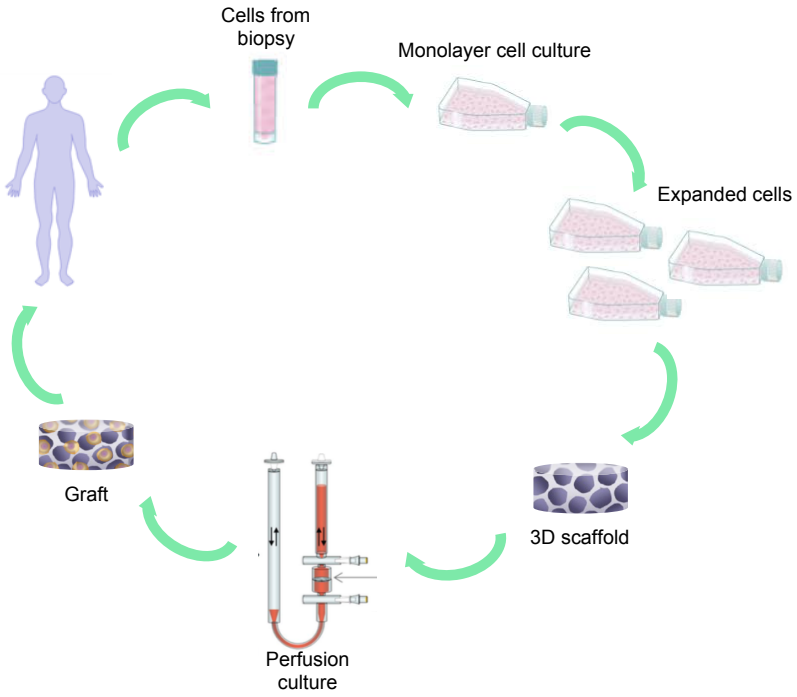

Figure 1-5 Schematic representation of the tissue engineering paradigm.

In this method the scaffold acts as a support for tissue growth and maturation both *in vitro* and when implanted *in vivo*, degrading as cells deposit their ECM (33). However, despite significant successes have been achieved with this approach over the last 20 years, number of challenges still remain, preventing a pervasive clinical application of tissue engineering (34, 35). Among all the scientific issues, one of the main challenges is the development of biomaterials able both to support and guide cell growth, providing the appropriate biochemical and mechanical stimuli for the specific engineered tissue (36, 37). Another key issue lays in the design of biomaterials with a complex three-dimensional architecture able to match the requirements of hierarchical porosity and roughness, and which mimic the complexity of the *in vivo* milieu (33, 38).

1.2.1 THE IDEAL SCAFFOLD FOR ADIPOSE TISSUE ENGINEERING

Ideally, a scaffold should reproduce a 'native like tissue' with equivalent physiological, biochemical and mechanical properties. Synthetic polymers are appealing for tissue engineering applications because their chemistry can be tuned to fabricate scaffold with controllable and reproducible properties from the degradation and mechanical point of view (39, 40). Indeed, the mechanical cues are key factors in the differentiation process of each tissue (41, 42) and it has been showed that culturing ASCs on surfaces mimicking the stiffness of the adipose

tissue, namely in a range of 2-4 kPa, can spontaneously induce adipogenesis (Figure 1-6)(43).

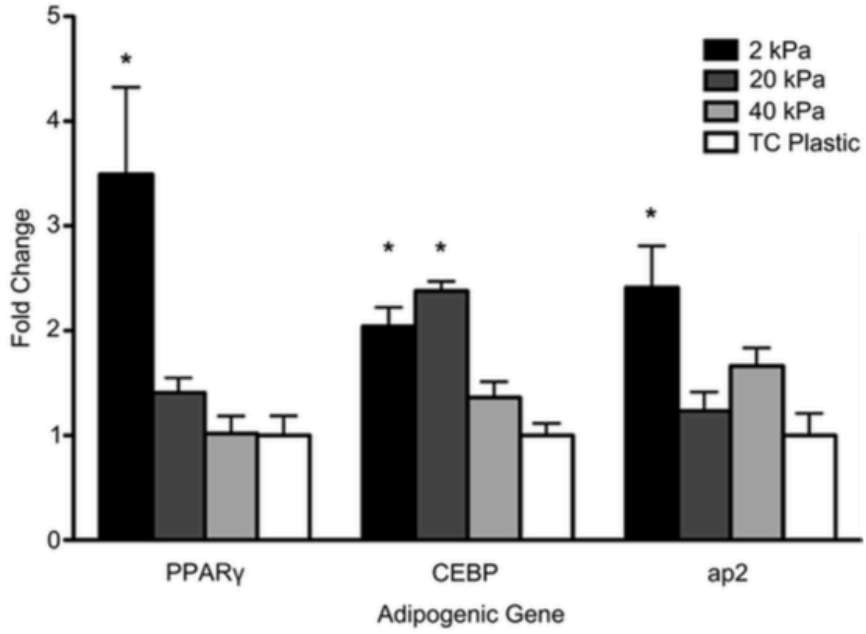

Figure 1-6 Adipogenic induction mediated by mechanical stimuli (43). Real-time PCR analysis for three key genes of the adipogenic differetniation: PPARg, CEBPa and fatty acid binding protein 4 (ap2 or FABP4). Results highlight an upregulation of adipogenic genes after culture on substrates with a stiffness of 2 kPa.

Adhesive properties are also among the fundamental criteria that should be taken in account when designing a scaffold. Indeed, 3D synthetic hydrogels have been engineered in the past decades with several adhesive motifs in order to present a more realistic environment to cells (42). In details, one of the most widely used adhesive peptide in the biomaterials field is the tri-amino acid sequence, arginine-glycine-aspartate (RGD) that is the primary integrin-binding domain present on the ECM proteins (44, 45).

An ideal biomaterial should also be adipoinductive by itself. In this sense, it has been recently demonstrated that scaffolds obtained out of decellularized adipose matrix could provide an adipoinductive substrate for hASCs differentiation in absence of differentiation factors (46-49). Biologic scaffolds composed of ECM are commonly used for a variety of reconstructive surgical applications and are increasingly used in regenerative medicine strategies for tissue and organ replacement (50, 51). The ECM represents the secreted products of resident cells of each tissue and organ and has been shown to provide cues that affect cell migration, proliferation, and differentiation in a tissue specific manner (51-53).

In conclusion, scaffolding material integrating all the abovementioned properties

could provide a promising tool in the field of adipose tissue reconstruction.

1.3 AIM OF THE STUDY AND OUTLINE

In the light of this overview, it is evident that a successful approach for the treatment of adipose tissue defect, based on the principles of tissue engineering, should integrate the properties of synthetic and natural biomaterials together with patient's cells contribution. The aim of this study is to design a synthetic scaffold mimicking the mechanical and structural properties of native adipose tissue and to combine it with adipose ECM in order to obtain a hybrid material. Our hypothesis is that the hybrid material could provide a useful solution to the current limitations in the field of adipose tissue reconstruction providing the mechanical and adipogenic stimuli necessary for a stable adipose tissue formation.

In details, the study is structured as it follows:

In **Chapter 2** the design of novel RGD-mimetic poly(amidoamine) oligomers (OPAA) based hydrogels with controlled degradation rate and improved mechanical and biological properties is presented. Two different approaches for the fabrication of OPAAs based hydrogels are presented. The results reported in this study indicate that the obtained hydrogels are promising biomaterials for the fabrication of tissue engineering scaffolds. The results support the use of OPAA hydrogels as tunable and inexpensive biomaterials for the creation of cell-laden constructs for the establishment of *in vitro* 3D model.

In **Chapter 3** the biologically and mechanically driven design of a macroporous scaffold started from RGD-mimetic OPAAs is presented. OPAAs are formed into a soft macroporous foam (OPAAF) by free-radical polymerization. An extensive screening of the biological, chemical and mechanical properties is performed. The results confirmed that the OPAAF is a suitable scaffold for adipose tissue engineering application being able to support adipogenesis *in vitro* and adipose tissue infiltration *in vivo*.

In **Chapter 4** the OPAAF is further engineered by decoration with devitalized adipose matrix. The decoration and decellularization protocols are optimized and characterized in detail. Two different protocols are adopted for the ECM decoration in order to investigate the effect of a differentiated and stromal matrix on adipogenic commitment. The adipoinductive potential of the hybrids ECM-OPAAF is widely demonstrated both *in vitro* and *in vivo*.

In **Chapter 5** there is a general review of the results obtained in this work and the possible future perspectives.

In the **Appendix** an *in vitro* 3D bone model starting from human progenitors is established to investigate the role of the transmembrane receptor expressed on myeloid cells 2 (TREM-2) in bone metabolism. Human progenitors are differentiated into osteoblasts and osteoclasts reproducing the complex interplay occurring in bone tissue. ECM turnover and TREM-2 levels are monitored over time. Being TREM-2 a possible target for the treatment of Alzheimer Disease (AD) in the central nervous system, our model aim at investigating possible side effects on bone metabolism by the stimulation of this receptor.

1.4 REFERENCES

1. Farmer SR. Molecular determinants of brown adipocyte formation and function. (0890-9369 (Print)).
2. Ailhaud G. Cross talk between adipocytes and their precursors: relationships with adipose tissue development and blood pressure. (0077-8923 (Print)).
3. Kahn BB, Flier JS. Obesity and insulin resistance. (0021-9738 (Print)).
4. Steppan CM, Bailey St Fau - Bhat S, Bhat S Fau - Brown EJ, Brown Ej Fau - Banerjee RR, Banerjee Rr Fau - Wright CM, Wright Cm Fau - Patel HR, et al. The hormone resistin links obesity to diabetes. (0028-0836 (Print)).
5. Hausman DB, DiGirolamo M Fau - Bartness TJ, Bartness Tj Fau - Hausman GJ, Hausman Gj Fau - Martin RJ, Martin RJ. The biology of white adipocyte proliferation. (1467-7881 (Print)).
6. Gesta S, Tseng Yh Fau - Kahn CR, Kahn CR. Developmental origin of fat: tracking obesity to its source. (0092-8674 (Print)).
7. Flynn L, Semple Jl Fau - Woodhouse KA, Woodhouse KA. Decellularized placental matrices for adipose tissue engineering. (1549-3296 (Print)).
8. Gregoire FM SC, and Sul HS. Understanding Adipocyte Differentiation. American Physiology Society. 1998.
9. Ross SE, Hemati N Fau - Longo KA, Longo Ka Fau - Bennett CN, Bennett Cn Fau - Lucas PC, Lucas Pc Fau - Erickson RL, Erickson Rl Fau - MacDougald OA, et al. Inhibition of adipogenesis by Wnt signaling. (0036-8075 (Print)).

10. Tontonoz P, Spiegelman BM. Fat and beyond: the diverse biology of PPARgamma. (0066-4154 (Print)).
11. Otto TC, Lane MD. Adipose development: from stem cell to adipocyte. (1040-9238 (Print)).
12. Lefterova MI, Lazar MA. New developments in adipogenesis. (1043-2760 (Print)).
13. Cristancho AG, Lazar MA. Forming functional fat: a growing understanding of adipocyte differentiation. (1471-0080 (Electronic)).
14. Choi JH, Gimble JM, Lee K, Marra KG, Rubin JP, Yoo JJ, et al. Adipose tissue engineering for soft tissue regeneration. Tissue engineering Part B, Reviews. 2010;16(4):413-26.
15. Comley K, Fleck NA. A micromechanical model for the Young's modulus of adipose tissue. International Journal of Solids and Structures. 2010;47(21):2982-90.
16. Abrahamson DR. Recent studies on the structure and pathology of basement membranes. (0022-3417 (Print)).
17. Ikuyo Nakajima TYKO, Hisashi Aso. Adipose tissue extracellular matrix: newly organized by adipocytes during differentiation. Differentiation. 1998.
18. Sun K, Tordjman J Fau - Clement K, Clement K Fau - Scherer PE, Scherer PE. Fibrosis and adipose tissue dysfunction. (1932-7420 (Electronic)).
19. Combellack EJ, Jessop ZM, Naderi N, Griffin M, Dobbs T, Ibrahim A, et al. Adipose regeneration and implications for breast reconstruction: update and the future. (2227-684X (Print)).
20. Holmes JD. Capsular contracture after breast reconstruction with tissue expansion. (0007-1226 (Print)).
21. Pajkos A, Deva Ak Fau - Vickery K, Vickery K Fau - Cope C, Cope C Fau - Chang L, Chang L Fau - Cossart YE, Cossart YE. Detection of subclinical infection in significant breast implant capsules. (0032-1052 (Print)).
22. Wu LC, Bajaj A Fau - Chang DW, Chang Dw Fau - Chevray PM, Chevray PM. Comparison of donor-site morbidity of SIEA, DIEP, and muscle-sparing TRAM flaps for breast reconstruction. (1529-4242 (Electronic)).
23. Bajaj AK, Chevray Pm Fau - Chang DW, Chang DW. Comparison of donor-site complications and functional outcomes in free muscle-sparing TRAM flap and free DIEP flap breast reconstruction. (1529-4242 (Electronic)).

24. Tachi M, Yamada A. Choice of flaps for breast reconstruction. (1341-9625 (Print)).

25. Toyserkani NM, Quaade ML, Sorensen JA. Cell-Assisted Lipotransfer: A Systematic Review of Its Efficacy. (1432-5241 (Electronic)).

26. Tsuji W, Rubin JP, Marra KG. Adipose-derived stem cells: Implications in tissue regeneration. (1948-0210 (Electronic)).

27. Chan CW, McCulley Sj Fau - Macmillan RD, Macmillan RD. Autologous fat transfer--a review of the literature with a focus on breast cancer surgery. (1878-0539 (Electronic)).

28. Eto H, Kato H Fau - Suga H, Suga H Fau - Aoi N, Aoi N Fau - Doi K, Doi K Fau - Kuno S, Kuno S Fau - Yoshimura K, et al. The fate of adipocytes after nonvascularized fat grafting: evidence of early death and replacement of adipocytes. (1529-4242 (Electronic)).

29. Ross RJ, Shayan R Fau - Mutimer KL, Mutimer Kl Fau - Ashton MW, Ashton MW. Autologous fat grafting: current state of the art and critical review. (1536-3708 (Electronic)).

30. Langer R, Vacanti JP. Tissue engineering. Science (New York, NY). 1993;260(5110):920-6.

31. Nerem RM, Sambanis A. Tissue engineering: from biology to biological substitutes. (1076-3279 (Print)).

32. Lalan S, Pomerantseva I Fau - Vacanti JP, Vacanti JP. Tissue engineering and its potential impact on surgery. (0364-2313 (Print)).

33. Lavik E, Langer R. Tissue engineering: current state and perspectives. (0175-7598 (Print)).

34. Khademhosseini A, Langer R Fau - Borenstein J, Borenstein J Fau - Vacanti JP, Vacanti JP. Microscale technologies for tissue engineering and biology. (0027-8424 (Print)).

35. Viswanathan S, Joshi C. Regenerative medicine: challenges and perspectives for successful therapies. (0070-217X (Print)).

36. Borenstein JT, Weinberg Ej Fau - Orrick BK, Orrick Bk Fau - Sundback C, Sundback C Fau - Kaazempur-Mofrad MR, Kaazempur-Mofrad Mr Fau - Vacanti JP, Vacanti JP. Microfabrication of three-dimensional engineered scaffolds. (1076-3279 (Print)).

37. Geckil H, Xu F Fau - Zhang X, Zhang X Fau - Moon S, Moon S Fau - Demirci U, Demirci U. Engineering hydrogels as extracellular matrix mimics. (1748-6963 (Electronic)).

38. Hollister SJ. Porous scaffold design for tissue engineering. Nature materials. 2005;4(7):518-24.

39. Drury JL, Mooney DJ. Hydrogels for tissue engineering: scaffold design variables and applications. Biomaterials. 2003;24(24):4337-51.

40. Martello F, Tocchio A, Tamplenizza M, Gerges I, Pistis V, Recenti R, et al. Poly(amido-amine)-based hydrogels with tailored mechanical properties and degradation rates for tissue engineering. Acta Biomater. 2014;10(3):1206-15.

41. Gardel M, Schwarz U. Cell-substrate interactions. Journal of physics Condensed matter : an Institute of Physics journal. 2010;22(19):190301-.

42. Caliari SR, Burdick JA. A practical guide to hydrogels for cell culture. (1548-7105 (Electronic)).

43. Young DA, Choi YS, Engler AJ, Christman KL. Stimulation of adipogenesis of adult adipose-derived stem cells using substrates that mimic the stiffness of adipose tissue. Biomaterials. 2013;34(34):8581-8.

44. Plow EF, Haas Ta Fau - Zhang L, Zhang L Fau - Loftus J, Loftus J Fau - Smith JW, Smith JW. Ligand binding to integrins. (0021-9258 (Print)).

45. von der Mark K, Park J Fau - Bauer S, Bauer S Fau - Schmuki P, Schmuki P. Nanoscale engineering of biomimetic surfaces: cues from the extracellular matrix. (1432-0878 (Electronic)).

46. Cheung HK, Han TT, Marecak DM, Watkins JF, Amsden BG, Flynn LE. Composite hydrogel scaffolds incorporating decellularized adipose tissue for soft tissue engineering with adipose-derived stem cells. Biomaterials. 2014;35(6):1914-23.

47. Flynn LE. The use of decellularized adipose tissue to provide an inductive microenvironment for the adipogenic differentiation of human adipose-derived stem cells. Biomaterials. 2010;31(17):4715-24.

48. Flynn LE, Prestwich GD, Semple JL, Woodhouse KA. Proliferation and differentiation of adipose-derived stem cells on naturally derived scaffolds. Biomaterials. 2008;29(12):1862-71.

49. Han TT, Toutounji S, Amsden BG, Flynn LE. Adipose-derived stromal cells mediate in vivo adipogenesis, angiogenesis and inflammation in decellularized adipose tissue bioscaffolds. Biomaterials. 2015;72:125-37.

50. Badylak SF. The extracellular matrix as a biologic scaffold material. Biomaterials. 2007;28(25):3587-93.

51. Badylak SF, Freytes Do Fau - Gilbert TW, Gilbert TW. Extracellular matrix as a biological scaffold material: Structure and function. (1878-7568 (Electronic)).

52. Bissell Mj Fau - Hall HG, Hall Hg Fau - Parry G, Parry G. How does the extracellular matrix direct gene expression? (0022-5193 (Print)).

53. Ingber D. Extracellular matrix and cell shape: potential control points for inhibition of angiogenesis. (0730-2312 (Print)).

54. Yoshimura Kato and Yuko Asano, Fat injection. Plastic and reconstructive surgery, 2015.

CHAPTER 2

2 RGD-MIMETIC POLY(AMIDOAMINE) BASED HYDROGELS WITH TUNABLE MECHANICAL AND DEGRADATION PROPERTIES FOR THE FABRICATION OF CELL LADEN CONSTRUCTS

Eleonora Rossi [a,b,c] et al.

a) Fondazione Filarete, Viale Ortles 22/4, 20139 Milano, Italy; b) SEMM, European School of Molecular Medicine, Campus IFOM-IEO, Via Adamello 16, 20139 Milano, Italy; c) CIMaINa, Dipartimento di Fisica, Università degli Studi di Milano, Via Celoria 16, 20133 Milano, Italy

The work presented in this this chapter has been published in two different papers:

1. Alessandro Tocchio, Federico Martello, Margherita Tamplenizza, Eleonora Rossi, Irini Gerges, Paolo Milani, Cristina Lenardi."RGD-mimetic poly(amidoamine) hydrogel for the fabrication of complex cell-laden micro constructs". *Acta Biomaterialia*, 2015.

2. Irini Gerges*, Margherita Tamplenizza*, Eleonora Rossi*, Alessandro Tocchio, Federico Martello, Camilla Recordati, Deepak Kumar, Nicholas R. Forsyth, Yang Liu, Cristina Lenardi. "A Tailor-Made Synthetic Polymer for Cell Encapsulation: Design Rationale, Synthesis, Chemical–Physics and Biological Characterizations ", Macromolecular Bioscience, 2016.

2.1 INTRODUCTION

In past years much attention has been paid to three-dimensional (3D) cell culture as a tool for the establishment of *in vitro* biological models (1). In fact, researchers have come to appreciate the different biological response between cells cultured in monolayers and in 3D, which is more consistent with the environment in which cells physiologically operate (2,3). It is well known that the interplay between cells and the extracellular matrix (ECM) *in vivo* play critical roles in controlling their behaviour and functioning (4). Therefore, much effort has been made to design synthetic 3D ECMs able to mimic the properties of natural cellular milieu, thus providing a more realistic environment to cells *in*

vitro (5). The 3D cell culture approach is a useful tool to create *in vitro* models for the investigation of cells behaviour in specific disease and for drug screening (6,7). For this reason, several materials with controllable biological, chemical and mechanical properties have been developed (8,9) in order to recapitulate natural ECM microstructures, with the ultimate goal of controlling cell and tissue functions (5,10–13). In this context, hydrogels have proved to be desirable biomaterial systems for guiding 3D cell behaviour to specific functions (14) thanks to their hydrophilicity and biocompatibility. Naturally derived molecules are commonly used to create cell-laden hydrogels thanks to their intrinsic bioactivity, biocompatibility and biodegradability (15–22). In particular, cell-laden hydrogels have been created from a wide range of native ECM molecules, including collagen (15), fibrin (16,17), hyaluronic acid (18,19), Matrigel (20,21), and gelatine (22). These biomolecules naturally contain cell-signalling attributes that enable high cellular viability and proliferation. Nevertheless, the cues that enable cells to prosper in these materials are so abundant that it is not easy to accurately control and assess their effects on cellular behaviour (5). In addition, their intrinsic batch-to-batch variability results in hydrogels with physic-chemical properties difficult to reproduce and engineer (5).

In general, this leads to the inability to reliably control the hydrogels' mechanical properties thus limiting their versatility for creating 3D cellular constructs. In the attempt to solve some of the above issues, synthetic polymer-based hydrogels have been increasingly studied as 3D culture platforms, due to simple synthetic process, low costs and ease of functionalization, resulting in high tunability of the chemical and biophysical properties (8,9,12–14). On the other hand, hydrogels from synthetic molecules generally lack a mechanical behaviour comparable to natural origin materials such as, for instance, strain stiffening as observed for collagen and fibrin (23,24).

A promising class of synthetic polymers for cell culture applications are poly(amidoamine)s (PAAs). They are obtained by Michael-type addition of bis-acrylamides to primary amines and/or secondary diamines, under mild conditions (25). Their simple synthetic process allows for the incorporation of various bioactive molecules in the PAA's backbone through covalent attachment (26–28). In general, PAA-based hydrogels have good biocompatibility and are easily modifiable by introducing different co-monomers such as carboxylic acids, thiols

and amino groups (29–34) that provide additional chemical functions. In order to improve the cell adhesion properties of PAA hydrogels, Ferruti and co-workers developed an Arg-Gly-Asp (RGD) mimetic PAA with a repeating unit composed of 2,2-bisacrylamidoacetic acid (BAC) and 4-aminobutylguanidine (ABG, agmatine) (35). In particular, it was observed that introduction ABG units in a cross-linked amphoteric PAA hydrogel increased fibroblasts adhesion (35). Moreover, it has been demonstrated that the ABG residue in PAA hydrogels maintains cell adhesion properties even when copolymerized with other monomers (33). Notably, despite their interesting biological properties, various limitations have been observed when using PAA hydrogels for cell encapsulation such as limited transparency, poor mechanical properties and the need of several washing cycles to eliminate unreacted monomers (35). These issues have prevented them from being used for developing *in vitro* models for 3D cell culture.

Here we present two different approaches for the fabrication of RGD-mimetic PAA based hydrogels with tunable mechanical and degradation properties. In the first study, we copolymerized the RGD-mimetic PAA oligomers (OPAAs) with poly(ethylene glycol) (PEG) to fabricate hydrogels with improved biological, mechanical and optical transparency properties. In the second part, a synthetic polymeric precursor for cell encapsulation was realized with the aim to combine, by grafting, the adhesive properties of RGD-mimetic PAAs with the good mechanical integrity of poly(2-hydrox-yethyl)methacrylate (PHEMA)-based hydrogels.

2.1.1 PAA-JEFFAMINE®-PAA TRIBLOCK COPOLYMER (PJP)

Among synthetic hydrogels, poly(ethylene glycol) (PEG) is considered to be the gold standard thanks to its high hydrophilicity and its inert network resistant to protein adsorption (4,11). However, pure PEG hydrogel lacks the cell-responsive features able to promote cell adhesion, viability and migration, that are crucial for the creation of organized 3D cellular constructs. In order to overcome these limitations, modifications with binding motif RGD (36–38), incorporation of proteolytically degradable peptide backbone (39,40) or physical mixing with ECM components (19) have been investigated. In particular, PEG hydrogels containing both cell binding RGD motifs and matrix metalloproteinase (MMP)-sensitive degradation regions have been shown to promote cell elongation,

migration and interconnection *in vitro* with different cell lines (41–47). In this study, we report the synthesis of a new photocrosslinkable, biomimetic PAA-Jeffamine®-PAA triblock copolymer (PJP) hydrogel in order to provide an inexpensive alternative to the use of RGD peptide-based hydrogels. In particular, we presumed that by copolymerizing the PAA-based ABG with Jeffamine® it would be possible to obtain a hybrid RGD-mimetic PAA macromer to be used in the synthesis of hydrogels with improved biocompatibility, cell-adhesion, optical and mechanical properties. The physic-chemical properties of PJP hydrogels are extensively discussed. An in-depth analysis was carried out on 2D cell culture and 3D cell encapsulation behaviour with different cell types.

2.1.2 PAA BASED GRAFTING OF NON-ADHESIVE SYNTHETIC POLYMER

In this work, a new synthetic polymeric precursor for cell encapsulation was realized with the aim to gather the promising cell adhesion property of RGD-mimetic PAAs and the good mechanical integrity of poly(2-hydroxyethyl)methacrylate (PHEMA)-based hydrogels (55,56). The polymeric precursor is characterized by a comb-like structure, where an acrylic mother backbone, poly((2-hydroxyethyl)methacrylate-co-(3 aminopropyl)methacrylamide)-(P(HEMA-co-APM)), was grafted by acrylamide-terminated RGD-mimetic PAA moieties. The sol–gel transition of the polymer solution takes place by photo-cross-linking under mild conditions (57). The study describes the rationale behind the comb-like structure design, the role of P(HEMA-co-APM) mother backbone in the regulation of the grafting density and hence the modulation of degradation kinetics and compression properties of P(HEMA-co-APM)/PAA photo-cross-linked hydrogels (58). The capability of P(HEMA-co-APM)/PAA hydrogels to support 3D cell encapsulation was preliminary investigated, using NIH3T3 cell line, and was qualitatively compared to that of a gelatine methacrylate-based hydrogel, a widely studied chemically modified natural polymer for cell encapsulation (59,60).

2.2 MATERIALS AND METHODS FOR PJP

2.2.1 MATERIALS

4-Aminobutylguanidine sulfate (ABG, agmatine, Biosynth/ Sigma Aldrich), ammonium persulfate (APS), O,O-Bis(2-amino- propyl) poly(propylene glycol)-

block-poly(ethylene glycol)-block- poly(propylene glycol) with molecular weight of 600 (Jeffamine 600), 2-hydroxy-1-(4-(hydroxyethoxy)phenyl)-2- methyl-1-propanone (Irgacure 2959, CIBA Chemicals), low-melting point agarose, dimethyl sulfoxide (DMSO), lithium hydroxide monohydrate (LiOH), hydrochloric acid 37% (HCl), trichlorododecylsilane (TCS), and tetramethylethylenediamine (TEMED), sodium chloride (NaCl), sodium phosphate dibasic (Na_2HPO_4), potassium phosphate monobasic (KH_2PO_4) were purchased from Sigma– Aldrich at the highest degree of purity available and used as received. Milli-Q grade water was used for all the experiments. The phosphate buffered saline (PBS) used in the experiments contained 2.69 mM KCl, 136.89 mM NaCl, 3.21 mM Na_2HPO_4, 1.47 mM KH_2PO_4. Lastly, 2,2-bis(acrylamido)acetic acid (BAC) was prepared as previously reported and its purity (99.9%) was determined both by acid–base titration and by NMR spectroscopy (33). The materials were all purchased from Sigma Aldrich and used as supplied, unless otherwise stated.

2.2.2 Glass slides silanization and mold fabrication

Glass slides were silanized for fabricating cylindrical molds. In short, the glass slides were washed with acetone, activated by plasma oxygen (70 W, 70 s) and immersed in a TCS solution (5% v/v in petroleum ether) for 10 min. The slides were then repeatedly washed with petroleum, ether, ethanol and water, and dried with a gentle airflow and stored at room temperature. Different-sized molds were prepared by interposing preformed silicone spacers (1.0, 3.0 and 6.0 mm thick) between two silanized glass slides. It is important to note that void circles (Ø of 6, 10 and 12 mm, respectively) had previously been cut into the preformed silicone spacers.

2.2.3 PAA oligomer (OPAA) synthesis

In a 2 mL glass tube, BAC (200 mg, 1.0 mM), water (333 lL), LiOH (48.8 mg, 1.14 mM) and ABG (for OPAA-2: 168.8 mg, 0.717 mM) were added in this order and the resulting pH 9 mixture was stirred at 35 °C for 7 days in the dark and under inert atmosphere. The mixture was then diluted 1:50 with bi-distilled water and brought to pH 4.0 by adding concentrated HCl. The solution was purified by eliminating unreacted BAC through ultrafiltration on membrane with a cut-off of 1 kDa and subsequently freeze-dried (Telstar Cryodos 50). The oligomers'

chemical structure was confirmed by HNMR spectroscopy. GPC data: OPAA, Mn = 2100, d = 1.31. The average molecular weight of the obtained OPAA was 2 kDa, therefore the polymer was termed OPAA-2.

2.2.4 PJP OLIGOMER SYNTHESIS

The PJP diacrylamide terminated oligomers were synthesized by Michael-type addition of PAA to Jeffamine®. In brief, in a 5 mL vial, OPAA-2 (600 mg, 0.3 mmol) was added followed by LiOH-saturated water (850 lL) and Jeffamine® 500, 50.0 mg, 0.1 mmol. The pH of the mixture was adjusted to 10.5 by adding LiOH and HCl until a transparent solution was obtained. The reactant solution was stirred in the dark at 35 °C for 24 h under inert atmosphere and pH was monitored. The solution was then diluted 1:50 with bi-distilled water, acidified to pH 7.0 with a few drops of HCl (37%), ultra-filtrated (5 kDa cut-off membrane) and freeze-dried. The oligomers' chemical structure was confirmed by HNMR spectroscopy. Approx. Yield of PJP: 85%. The average molecular weight of the obtained PJP was 4 kDa, therefore the obtained copolymer was termed PJP-4.

2.2.5 HYDROGELS FABRICATION AND CHARACTERIZATION

Freeze-dried OPAA-2 and PJP-4 oligomer were mixed into PBS. Irgacure 2959 (1000 mg/mL in 100% DMSO) was added as a photo-initiator to the hydrogel pre-polymer solution in order to obtain final concentrations of 0.5% (w/v). The reacting mixture was stirred for 1 min, injected into the glass mold and photopolymerized by exposing it to UV light (365 nm, 10 mW/cm2) for 3 min. The hydrogels were then gently extracted from the mold.

2.2.5.1 CHEMICAL CHARACTERIZATION

Size exclusion chromatography (SEC) traces of PAA-based polymers were obtained with Tosoh-Haas 486 columns using 0.1 M Tris buffer pH 8.00 ± 0.05 as a mobile phase, with a UV detector operating at 230 nm. Molecular weight determination was based on pullulan standards. Proton nuclear magnetic resonance (HNMR) analyses were run on a Bruker Avance 400 spectrometer operating at 400.132 MHz. Fourier-transform infrared spectroscopy (FTIR) spectra of dry hydrogel samples were measured using a Jasco ATR-FTIR 300 spectrophotometer.

2.2.5.2 OPTICAL CHARACTERIZATION

Photographs of the hydrogels were taken with a digital single-lens reflex camera (Canon EOS 1000D, Canon).

2.2.5.3 MECHANICAL CHARACTERIZATION

The hydrogels were mechanically tested in unconfined compression with a standard material testing machine with a 5 N load cell (Dynamic Mechanical Thermal Analyser, Mk III, Rheometric Scientific). All tests were performed at 37 °C and a preload of 0.05 N was applied to ensure that the surfaces of the hydrogels were in direct contact with the loading plate. Dynamic mechanical analysis (DMA) was performed with ±2% displacement amplitude of the unloaded height in a range of frequencies ranging from 0.1 to 50 Hz and Storage modulus was calculated. The hydrogels were prepared at 15% (w/v) concentration by injection molding into respectively 6 mm diameter, 3 mm height cylinders for PJP-4, and 12 mm diameter, 6 mm height cylinders for OPAA-2. The obtained hydrogels were equilibrated in PBS for at least 2 h before the DMA.

2.2.5.4 SWELLING TEST

The cylindrical hydrogel samples measuring 10 mm in diameter and 1 mm in thickness, were previously dried at 20 °C and 0.1 Torr. They weighed 20 mg ± 2 mg. The specimen was placed inside a 24-multiwell plate containing 3 mL PBS per each well (pH 7.0), incubated at 37 °C and weighed at regular intervals. Their water uptake was measured until the maximum mass was obtained. The percentage of water absorbed was calculated with the following formula:

Swelling (%) = W_{wt}/W_d x 100,

where W_{wt} is the water mass absorbed at time t and W_d is the mass of the dry sample at time zero.

2.2.6 DEGRADATION TEST

The 1-mm-thick hydrogel cylindrical slabs measuring 10 mm in diameter were placed inside a 10 mL test tube containing 5 mL PBS (pH 7.0) and incubated at 37 °C. At fixed time point they were freeze-dried and weighed. The per cent degradation was calculated with the following formula:

Degradation (%) W_f/W_d x 100,

where W_f is the dry weight at time t, W_d is the mass of the dry sample at time zero.

2.2.7 CELL CULTURE

NIH 3T3 murine embryonic fibroblasts (CRL-1658, ATCC, Manassas, Virginia) were kept at 37 °C in a 5% CO_2 98% air-humidified incubator. The cells were cultured in Dulbecco's Modified Eagle's Medium (DMEM) supplemented with 10% Fetal Bovine Serum (FBS), 2 mM L-Glutamine, 100 units/mL penicillin and 100lg/mL–streptomycin. When they were 80% confluent, the 25-cc flasks were passaged (subculture ratio 1:4 for multiple flasks) every 2–3 days for both experiments. Human umbilical vein endothelial cells (HUVECs) were obtained from PromoCell Gmbh (Heidelberg, Germany). The cells were cultured in M199 medium supplemented with 2 mM L-Glutamine, 100 units/mL penicillin and 100 lg/mL–streptomycin and 20% FBS, 50 ng/mL ECGF and 100lg/mL Heparin were freshly added.

2.2.8 2D CELL CULTURE ON HYDROGEL DISCS

NIH 3T3 and HUVEC (cell density: 10^4 cells/cm^2) cells were seeded on UV-sterilized hydrogel disks containing multiwell plates (24–48 wells), incubated in 5% CO_2 at 37 °C and 98% air- humidified. The cells were cultured for 24–48 h during which their growth was monitored with an inverted phase contrast microscope (Leica micro systems, Germany) equipped with a digital Leica DFC 295 camera.

2.2.9 CELL ADHESION AND PROLIFERATION

After 48 h the hydrogel disk cells were washed with PBS solution, fixed with 4% paraformaldehyde for 15 min at room temperature, rinsed with PBS, permeabilized with 0.1% Triton X-100 and finally stained with BisBenzimide H 33258 (Hoechst) 5 lg/mL. Images were then collected with a Leica SP5 confocal microscope (5 fields for disk, 10X magnification zoom 2) and cell proliferation over time was evaluated by means of ImageJ software.

2.2.10 FLUORESCENT STAINING

After 48 h in culture, the cells were fixed in situ with 4% paraformaldehyde, rinsed with PBS, permeabilized with 0.1% Triton X-100, blocked with 2% BSA and then incubated with Alexa fluor 555 directly conjugated to phalloidin, 0.11 lm, (Invitrogen, Inc., Eugene, OR) for 40 min at room temperature for filamentous actin staining. After washing in PBS, the cells were stained with Hoechst, 5

lg/mL. Images were captured along the channel length and channel depth (at 0.2–0.5 mm depth intervals) with a Leica SP5 confocal microscope. All scaffolds were imaged through the glass cover slip wall. HUVEC cultured on gelatine-coated glass served as a positive control.

2.2.11 CELL ENCAPSULATION

The murine fibroblasts were trypsinized, counted and suspended in PJP-4 macromer solution containing 0.5% (w/v) photoinitiator at a concentration of 5 x 10^6 cells/mL. Several macromer concentrations (7.5, 10, 15% w/w) were tested. The cell-macromer solution was injected into the glass mold and photopolymerized by exposing it to long-wavelength UV light (365 nm, 10 mW/cm^2) for 1 min. Agarose hydrogel (AGAR) was used as a control. In this case low-melting point agarose was dissolved in sterile PBS (pH 7.4) in order to obtain a final concentration of 2.5% (w/v) which was then heated to 70 °C. NIH 3T3 fibroblasts were trypsinized, counted and suspended in the agarose solution at 5 x 10^6 cells/mL which was cooled to 42 °C and pipetted to ensure even cell distribution. The agarose solution was injected in the glass mold and cooled to 4 °C for 20 min. The hydrogels were then extracted from the mold and incubated in DMEM under standard culture conditions. The media was changed every 48 h. Murine fibroblast viability within the hydrogels was quantified as the number ratio of viable cells to total cells by live/dead fluorescence assay (Calcein AM/Propidium Iodide, Life Technology).

2.2.12 STATISTICAL ANALYSIS

Each hydrogel type was tested at least 4 times obtaining similar results. All data are expressed as 100 / sample arithmetic mean/control arithmetic mean ± standard deviation. The significance of differences was determined by means of one-way ANOVA test ($p < 0.05$).

2.3 MATERIALS AND METHODS FOR PAA BASED GRAFTING OF NON-ADHESIVE SYNTHETIC POLYMER

2.3.1 MATERIALS

N-(2-Hydroxyethyl)methacrylate (HEMA) 97%, 2-mercaptoethanol (EtSH), agmatine, 97%, *N*,*N*-dimethylformamide (DMF) Chromasolv Plus ≥99%, dimethyl sulfoxide (DMSO) ≥99%, diethyl ether 99%, LiOH, Irgacure 2959 98% were purchased from Sigma Aldrich and used without further purification. 2,2′-

Azobis(2-methylpropionitrile) (AIBN) Fluka 98% has been recrystallized twice from methanol and kept in dark at 5 °C prior to use. *N*-(3-aminopropyl)methacrylamide hydrochloride (APM) 98%, was purchased from Polysciences Europe GMBH. BAC was synthesized as previously described and purity was determined by back-titration against HCl (33). All reagents were used as received without further purification unless otherwise stated.

2.3.2 Syntheses

2.3.2.1 Syntheses of P(HEMA-co-APM)s Oligomers

Three oligomers were prepared with different ratios between HEMA and APM. The amounts of reagents (g, mol), initial molar ratios, the average molecular weights of the oligomers and the yields are reported in Table 1. General procedure: APM, AIBN, EtSH, and DMF were introduced under stirring in 100 mL round bottomed flask, equipped with magnetic stirrer and hydrogen inlet. The reactor was degassed by repeated vacuum nitrogen cycles, and preceded in inert atmosphere at 70 °C for 24 h. During the polymerization process, it was observed that the colour of the reacting mixture changed gradually from colourless (at time zero) to yellow (after 12 h) to orange (after 24 h). As the reaction ended, the reaction was brought to room temperature, precipitated in four folds volume diethyl ether in order to eliminate DMF, EtSH before purification in distilled water through a semi permeable membrane of nominal molecular weight cut off 1000 Da. The polymers were obtained as yellowish powder after freeze-drying.

Reagents and product specifications	**P(HEMA$_{83}$-co-APM$_{17}$)**	**P(HEMA$_{77}$-co-APM$_{23}$)**	**P(HEMA$_{71}$-co-APM$_{29}$)**
HEMA [g], [mol]	3.67, 27.41	3.67, 27.41	3.67, 27.41
APM [g], [mol]	1.00, 5.48	1.50, 8.22	2.00, 10.96
EtSH [g], [mol]	0.44, 5.57	0.48, 6.04	0.51, 6.50
DMF [g], [mol]	17.65, 239.08	17.65, 239.08	17.65, 239.08
AIBN [g], [mol]	0.05, 0.28	0.05, 0.31	0.06, 0.33
[HEMA$_0$]/[M_0]	0.83	0.77	0.71
[APM$_0$]/[M_0]	0.17	0.23	0.29
$\left(\frac{[\text{HEMA}]}{[M]}\right)_{\text{HNMR}}$	0.90	0.82	0.77
$\left(\frac{[\text{APM}]}{[M]}\right)_{\text{HNMR}}$	0.10	0.18	0.23
Mn; Mw; P.D.	6390; 6750; 1.05	6650; 7890; 1.18	5930; 7250; 1.22
Yield [%]	55.18	50.94	49.32

Table 1. Syntheses of the mother backbone P(HEMA-co-APM) oligomers: reagents amounts, the molar ratios of HEMA and APM in the reactions feed and in the final products and reactions yields.

2.3.2.2 Grafting of P(HEMA-co-APM) with Acrylamide- Terminated RGD-Peptidomimetic PAA Moieties

The amounts of reagents (g, mol) used in the grafting reaction of the three oligomers P(HEMA-co-APM) are reported in Table 2. General procedure: In a round bottomed two-necked flask, equipped with magnetic stirrer and nitrogen inlet, P(HEMA-co- APM) was dissolved in distilled water. BAC and LiOH were added to P(HEMA-co-APM) solution under magnetic stirring. Finally, agmatine was added to the reacting mixture. The reactions pH at starting time was 9.5 and reached the value 8 after 2 d. The reactions were kept in dark under inert atmosphere, and continued for 7 d at 35 °C. The comb-like polymers: P(HEMA-co- APM)/PAA were purified through 3000 cut off semi-permeable membrane and obtained as yellowish powder by freeze drying. The chemical synthesis and the structural formula of the comb- like polymer P(HEMA-co-APM)/PAA is illustrated in Figure 2-6.

Reagents and products specifications	**P(HEMA$_{83}$-co-APM$_{17}$)/PAA**	**P(HEMA$_{77}$-co-APM$_{23}$)/PAA**	**P(HEMA$_{71}$-co-APM$_{29}$)/PAA**
P(HEMA-co-APM) [g]	2.00	2.00	2.00
BAC [g] [mol]	3.40, 17.00	3.80, 19.00	4.10, 20.05
Agmatine [g] [mol]	2.65, 11.25	2.65, 11.25	2.65, 11.25
LiOH·H_2O [g] [mol]	0.82, 19.25	0.91, 21.25	0.97, 22.75
H_2O [mL]	12.06	12.68	13.13
BD [%]	18.20	30.50	37.40
Yield [%]	70.00	80.00	80.00

Table 2. Syntheses of P(HEMA-co-APM)/PAA comb-like polymers: reaents amounts, BD and reactions yields.

2.3.2.3 Synthesis of Diacrylamide-Terminated RGD- mimetic PAA Oligomers (PAA-diAC)

In a round-bottomed flask, equipped with magnetic stirrer, BAC (3 g, 14.98 mmol) and LiOH (0.74 g, 16.69 mmol) were dissolved in 5 mL distilled water. Agmatine (2.01 g, 8.54 mmol) was then added to the reacting mixture. The reaction was kept in dark under inert atmosphere, and proceded for 7 d at 35 °C. PAAdiAc oligomer was purified through 1000 cut off semi-permeable membrane and obtained as yellowish powder by freeze-drying. The reaction yield was 70%. The average molecular weight, calculated from HNMR, in a semi-quantitative manner, was 1,2 kDa. The stoichiometric ratio "*r*" between amino and acrylamide functional groups was 0.57, with molar excess of acrylamide functional groups.

2.3.3 Size Exclusion Chromatography (SEC) and NMR Spectroscopy

Traces were obtained using: Waters 515 HPLC pump; 3 STYRAGEL HR4 columns and 1 STYRAGEL HR3 in series; Waters 410 Refractive Diffractometer detector. The mobile phase was DMF. The follow rate was 1 mL min^{-1}. The average molecular weights of P(HEMA-co-APM) oligomers were calculated using PS standard calibration curve.

HNMR spectra were acquired on Bruker Avance 400 spectrometer, operating at 400.133 MHz.

2.3.4 Hydrogels Preparation

Polymers solution was photo-crosslinked using UVP Black-Ray B-100AP High Intensity, 100 Watt/365 nm, 230 V, 50 Hz, 2.0 Amps. The distance between UV source and the polymeric solution was 12 cm. The polymer solution was exposed to UV source for 2 min. The photo-initiator was Irgacure and its final concentration in the polymers solutions was 0.5% (w/v).

2.3.5 Degradation Tests

Degradation tests were carried out for hydrogels obtained from the three comb-like formulations, prepared as described above, at the concentrations: 5, 7.5, 10, 12.5, and 15 (w/v) of the polymers solutions in Phosphate buffer saline PBS 1×. The hydrogel samples, of 10 mm average diameter and 3 mm thickness, were carefully extracted from the multi-well, washed in pure ethanol for an hour and dried under reduced pressure of 0.01 mbar, for 2 weeks. The study was carried out for seven time points: 3, 7, 15, 30, 45, 60, and 75 d. Each time point was carried out in three replicates. At each time point, hydrogels were removed from PBS, washed in pure ethanol for an hour and dried, as described above. Weight loss was calculated according to Equation (1) Weight loss% = $(W_0 - W_d) \times 100/W_0$

where W_0 and W_d are the initial and dried weight, respectively.

2.3.6 Compression Tests

Compression mechanical properties have been measured using a testing machine equipped with a 100 N load cell (model BR EMT503 A, MP Strumenti, Pioltello (MI), Italy). Cylindrical samples of 8 mm diameter and 3 mm height were analysed due to ISO 604-1993 protocol, compression speed was 0.5 mm min^{-1}. Elastic modulus has been calculated as the slope of stress–strain curve at deformation range from 5 to 10%. Measurements were carried out at room

temperature of 25 °C using acellular P(HEMA-co-APM)/PAA hydrogels, produced at 5, 7.5, 10, and 15% (w/v) concentration of the polymers solutions in PBS 1×. Six replicates were analysed for each test. All data are expressed as arithmetic mean ± SD. Significance of differences was determined using one-way ANOVA test ($p < 0.05$).

2.3.7 In vitro 3D Cell Culture

NIH 3T3 murine embryonic fibroblasts (CRL-1658, ATCC, Manassas, Virginia) were cultured under standard conditions (37 °C in 5% CO_2 98% air-humidified incubator). Cells were cultured in DMEM supplemented with 10% fetal bovine serum (FBS), 2× 10^{-3} m L-Glutamine, 100 units mL^{-1} penicillin and 100 μg mL^{-1}–streptomycin. Once 80% confluent, cells were passaged (subculture ratio 1:4 for multiple flasks) every 2–3 d for both experiments. For 3D encapsulation: NIH 3T3 fibroblasts were trypsinized, counted, and suspended in the comb-like polymer solutions, containing 0.5% (w/w) Irgacure, at a concentration of 5 × 10^6 cells mL^{-1}. The three comb-like formulations were photo-cross-linked and tested at the concentration of 15% (w/v). The cell–polymer solution was injected in a glass mold and photo-polymerized by exposure to long-wave length UV light (365 nm, 10 mW cm^{-2}) for 2 min. Hydrogels were then extracted from the mold and incubated in DMEM under standard culture conditions. Gelatine methacrylate (GelMa) was synthesized as described previously (18) and used as a control against the three comb-like formulations. GelMa was photo-cross-linked at the same concentration and experimental conditions described above. Murine fibroblast viability within the hydrogels was verified by live/dead fluorescence assay (Calcein AM/Propidium Iodide, Life Technology) after 48 h. Cell laden hydrogels were imaged using a confocal microscope (Leica Microsystems, Leica SP5) and z-stack acquisitions. Max projections were obtained by LAS AF software (Leica Microsystems). For cell viability quantification, nine images for each hydrogel group were acquired (three different fields for each hydrogel disc in triplicate) with a 10× magnification at zoom 2. Cell viability within the hydrogels was quantified as the number ratio of viable cells to total cells. All data are expressed as arithmetic mean ± SD. Significance of differences was determined using one-way ANOVA test ($p < 0.05$).

2.4 Results and Discussion for PJP

2.4.1 Hydrogels preparation

In this study, a new series of photo-crosslinkable hydrogels based on PJP-4 oligomers was designed, synthesized and compared with the relevant PAA and AGAR hydrogels in order to study the positive effects on biological properties resulting from the innovative polymeric structure. As reference material, diacrylamido-terminated PAA oligomer with average molecular weight of 2 kDa (OPAA-2) was synthesized by Michael-type addition between BAC and ABG, and subsequently purified by ultrafiltration and freeze-drying (Figure 2-1 A). In order to obtain a PAA-Jeffamine®-PAA tri-block copolymer (PJP) terminated with acrylamide functions, the synthesized OPAA-2 was coupled by means of the Michael-type addition with Jeffamine® (Figure 2-1 B). The resulted PJP copolymer, with average molecular weight of 4.6 kDa (PJP-4), was produced by coupling OPAA-2 and Jeffamine® with average molecular weight of 600 Da. After ultrafiltration and freeze-drying, the final triblock oligomer was photopolymerized through free-radical polymerization in order to obtain degradable hydrogels for cell encapsulation with RGD-mimetic monomeric units (Figure 2-1 C).

2.4.2 Optical properties

High optical transparency in hydrogels is a desirable feature for monitoring cellular processes *in vitro* (48). In order to determine the effect of Jeffamine® on the optical properties, PJP-4 hydrogel was qualitatively evaluated on pure OPAA-2 hydrogel as a negative control. 15% w/v concentration was selected in view of the cellular experiments. The optical images confirm that pure OPAA-2 hydrogels obtained are not transparent (Figure 2-1 D). This is probably due to the formation of acrylic chains during radical polymerization causing a phase separation in the reacting mixture (49,50). Interestingly, the presence of Jeffamine® was found to positively influence the optical properties. In particular, a higher level of transparency was observed in the PJP-4 hydrogel (Figure 2-1 E) when compared to the OPAA-2 hydrogel. We presume that the presence of Jeffamine® hinders the formation of microdomains responsible for light scattering in opaque hydrogels.

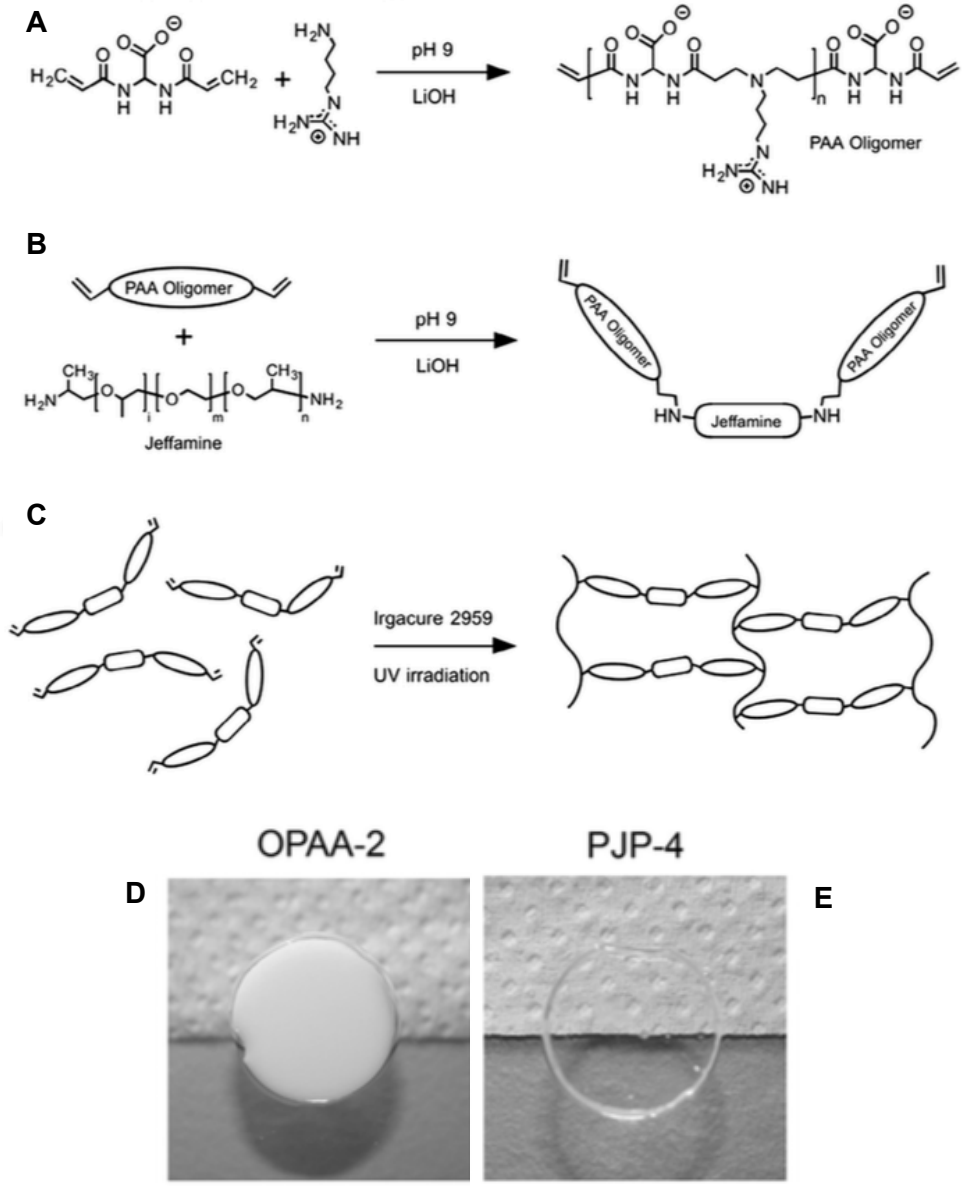

Figure 2-1 Synthetic scheme of the PJP oligomer. (A) Michael polyadditon of ABG and BAC yielded PAA oligomers. (B) After ultrafiltration PAA oligomers were left to react with Jeffamine® for 24 h in order to obtain PJP macromer. (C) The diacrylamido-terminated PJP macromer was crosslinked using UV irradiation in the presence of a photoinitiator yielding a hydrogel network. Comparison of the optical transparency of OPAA-2 and PJP-4 hydrogels (D and E respectively).

2.4.3 MECHANICAL PROPERTIES

It has been proved that the mechanical properties of the extracellular environment determine cellular behaviour and fate (8,9). To evaluate the effect, related to mechanical properties, of Jeffamine's insertion in PAA-based chemical structure, unconfined compression was performed on OPAA-2 and PJP-4 hydrogels, with a polymer concentration of 15% w/v. PJP-4 hydrogels showed storage modulus values four times higher than those of OPAA-2 (Figure 2-2 B) and range between

144 and 215 kPa, in accordance with the value interval of hydrogels used for tissue engineering applications (51). This enhanced storage behaviour of PJP-4 hydrogels, when compared to OPAA-2, emphasizes the role that Jeffamine® segments play in the contrast of non-covalent interaction among PAA micro-domains.

2.4.4 SWELLING AND DEGRADATION CHARACTERISTICS

The swelling characteristics of a polymer network are important in various applications as they affect solute diffusion, surface properties, mechanical properties, and surface mobility. The degree of hydrogel swelling depends on the pore size of the polymer network and the interaction between the polymer and the solvent. As hydration can have a significant effect on the physical properties of the hydrogel, e.g. the replication fidelity of the desired micropattern, the PJP's swelling ratio was investigated in respect to the hydrogel concentration. The hydrogels were made as previously described at 15% (w/v) PJP-4. The hydrogels were allowed to reach equilibrium over a 24 h incubation period at room temperature in PBS, we then calculated the mass swelling ratio of the swollen mass to the dry mass of polymer and the degradation rate at 37 °C in PBS. At 24 h the swelling ratio was 257% ± 6% for OPAA-2 and 404% ± 10% for PJP-4. These data show a higher swelling ratio of PJP-4 compared to OPAA-2, thus demonstrating the significant effect of the conjugation with Jeffamine® on the ability of hydrogel for storing water within the polymer network. The degradation rate was higher for PJP-4 hydrogel than for control OPAA-2 hydrogel, which was consistent with the higher swelling ratio of the studied polymers (Figure 2-2 A). This result demonstrated that the diacrylamide-terminated PJP, contained the ABG-BAC monomeric unit, acts both as an RGD-mimetic site and as a hydrolytically degradable function.

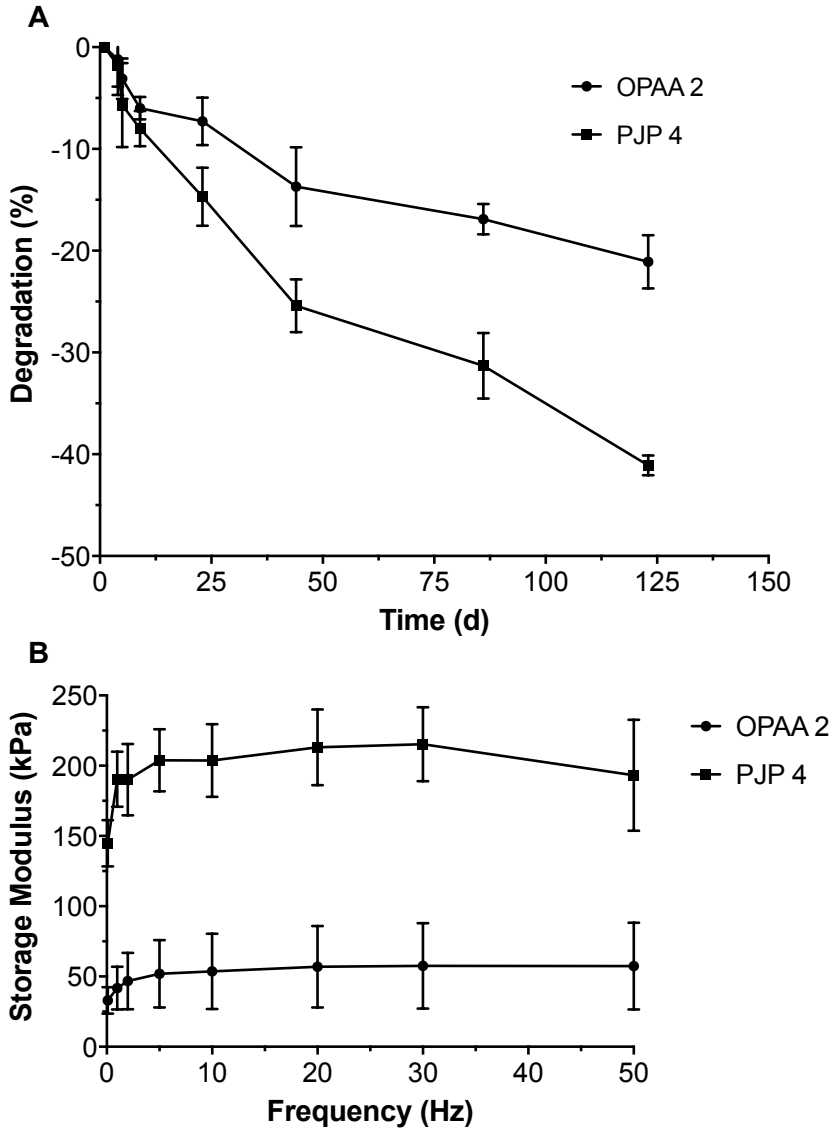

Figure 2-2 Degradation curves (A) of 15% (w/v) PJP-4, and control OPAA-2 hydrogels. Storage modulus (B) of 15% (w/v) OPAA-2 and PJP-4 hydrogels obtained by from DMA in unconfined compression at different solicitation frequencies. Error bars represent the SD of measurements performed on at least 3 samples.

2.4.5 NIH 3T3 CELL ADHESION TO 2D PJP SURFACES

The ability of a biomaterial in promoting cell binding strongly affects cell behaviour and is an essential requirement in tissue engineering and in the development of in vitro models for 3D cell culture (52). In order to validate hydrogels for these applications, we measured their cell adhesion properties using murine fibroblasts as a model cell type. Fibroblast adhesion was determined as a number of Hoechst positive cells per fixed area on PJP-4 hydrogels setting the concentration at 15% (Figure 2-3 A) and 30% (w/v) (Figure 2-3 B). Cell adhesion was also investigated on pure OPAA-2 hydrogels and glass. OPAA-2 hydrogels

showed the highest concentration levels of RGD-mimetic sites. Glass was used as positive control. NIH 3T3 readily bound to PJP-4 surfaces at all concentrations with roughly the same affinity following initial seeding but some differences were observed after 48 h. As we can see in Figure 2-3 A, OPAA-2 showed a better cell adhesion, as expected for the RGD-mimetic binding sites abundance (more than 3 times compared to glass), compared to PJP-4. Doubling the macromer concentration of PJP-4 from 15% to 30% (w/v) improved the performances with PJP-4 hydrogel (Figure 2-3 B). The significant differences in cell density, defined as the number of Hoechst positive cells per fixed area, demonstrated that cell density increases linearly with PJP-4 concentration. This behaviour is probably due to the increased stiffness of the PJP-4 surfaces and the density of RGD-mimetic sequences with increased macromer concentrations.

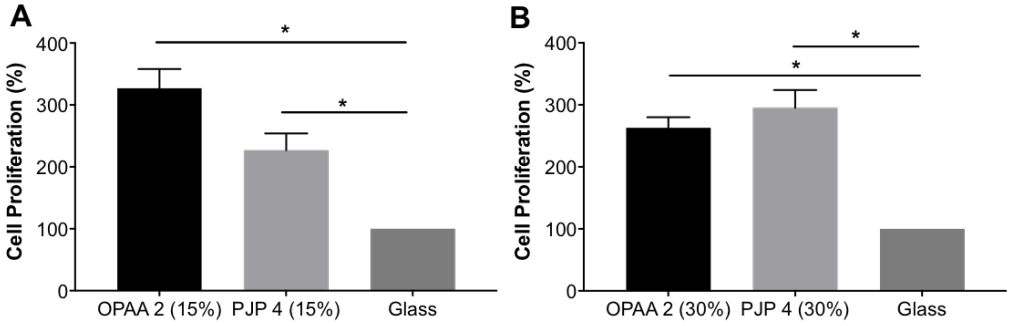

Figure 2-3 Cell proliferation values of NIH 3T3 cells cultured for 48 h on hydrogels using glass slide as a control: (A) OPAA-2 and PJP-4 at 15% (w/v) concentration; (B) OPAA-2 and PJB at 30% (w/v) concentrations.

2.4.6 HUVECs CELL ADHESION TO 2D PJP SURFACES

The surface adhesion characteristics of PJP-4 were determined at 15%, and 30% (w/v) concentration, by evaluating the number of Hoechst positive cells per fixed area. In this experiment, HUVECs were selected as a model cell type due to the possibility of using PJP-4 in vascularized tissue models, as well as to explore the compatibility of PJP-4 with a human cell type. The cells on the 15% and 30% PJP-4 surfaces attached and proliferated better than on the control (Figures 2-4). Endothelial phenotype seems to be maintained at all concentrations as suggested by the appearance of lumen-like ring structures (Figures 2-4 B and C). Significant differences in cell density, defined as the number of Hoechst positive cells per fixed area, demonstrated that cell density increases according to PJP-4 concentration. This behaviour is probably due to the increased stiffness of the PJP-4 surfaces and density of RGD-mimetic sequences with increased macromer

concentration.

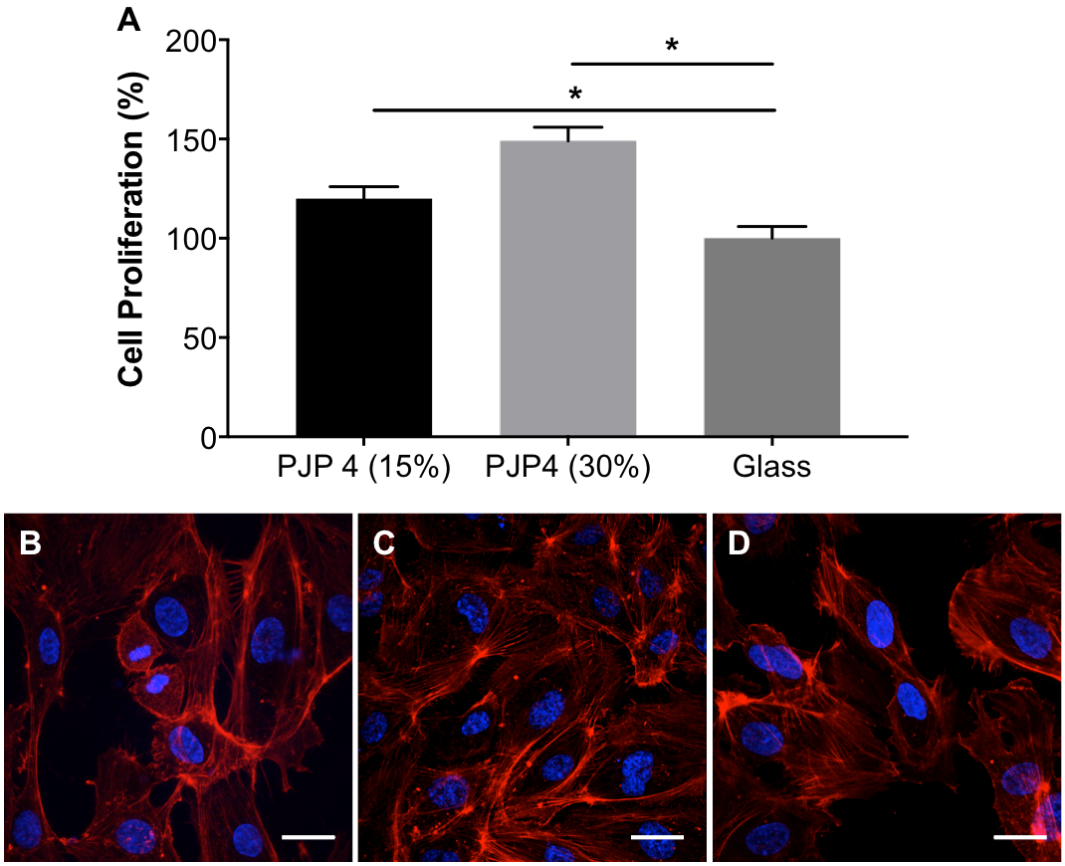

Figure 2-4 Cell proliferation of HUVECs cultured for 48 h on hydrogels of increasing PJP-4 concentrations (A). The symbol ‘‘*’’ represents statistical significance by students t-test ($p < 0.05$), comparing each sample against the gelatine-coated glass control (C-GLASS). Confocal microscopy images of HUVECs morphology on PJP-4 at 15% (B) and 30% (w/v) (C) on gelatine-coated glass (D) and (scale bar, 20 μm). The cytoskeleton is stained with phalloidin (red) and the nuclei with Hoechst (blue).

2.4.7 3D CELL ENCAPSULATION IN PJP-4

In order to confirm the use of PJP-4 as a hydrogel for tissue engineering, encapsulated cell behaviour was studied. In these experiments NIH 3T3 fibroblasts were encapsulated in a 0.3-mm-thick and 10-mm-diameter PJP-4 slab at 7.5%, 10% and 15% concentrations (w/v). Pure OPAA-2 hydrogel was not tested in 3D cell encapsulation experiments due to its mediocre optical transparency, hindering the viability assay with confocal microscopy. PJP-4 hydrogels gels performed similarly to PEG in terms of pattern replication accuracy and UV exposure time (data not shown). Viability at 4 h after encapsulation was 92% ± 1% in 7.5% PJP-4, 91% ± 3% in 10% and 90% ± 1% in 15% (w/v) hydrogel samples. Initial viability was similar to that observed in agarose hydrogels (95 ± 1%), demonstrating that UV polymerization and

micropatterning did not considerably alter cell state. In previous studies cell viability has been proved to decrease with macromer concentration in different hydrogel matrices (11,53). This viability loss is caused by encapsulation stress, nutrient limitations and swelling stress following polymerization. Cells viability in bulk PJP-4 up to 15% was similar to or better than the viability of agarose gel (Figure 2-5). Thanks to its optimal mechanical properties, PJP-4 formed solid cell laden hydrogels at all the concentrations tested. This allowed us to alter the number of cross-links in order to increase hydrogel permeability (53) and therefore the viability of the encapsulated cells. As a result, encapsulated fibroblasts showed cell viability comparable or better to the ones embedded in agarose gels, making PJP-4 a suitable material as platform for cell encapsulation. However, cells did not migrate or degrade the PJP-4 gels in any of the encapsulation experiments. This is due to the fact that although PJP-4 hydrogels are hydrolytically degradable, they lack enzymatic degradation motifs. Therefore cells cannot degrade and remodel the matrix, and cell movement and organization in 3D is limited. In order to solve this issue, PJP-4 could be modified by incorporating protease-sensitive regions (54).

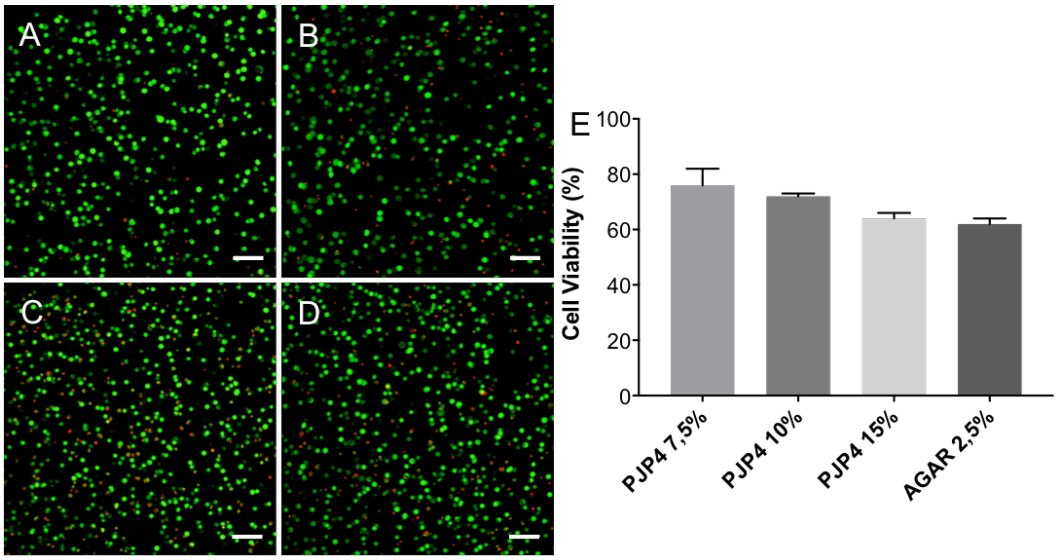

Figure 2-5 Characterization of encapsulated cell behaviour. NIH 3T3 fibroblasts embedded in PJP-4 at 7.5% (A), 10% (B), 15% (C) (w/v) and in agarose (D) microgel were stained with live/dead assay at 48 h after encapsulation (scale bar, 100 μm). The murine fibroblasts were stained with fluorescent live/dead assay (green: Calcein; red: Propidium iodide). Quantification of encapsulated cells viability (E) for different PJP-4 concentration, at 48 h compared to AGAR.

2.4.8 CONCLUSIONS

In this study, photo-crosslinkable PAA-based oligomer (PJP-4) was synthesized

as precursor of matrices for 3D cell culture and its physicochemical and mechanical properties were studied in comparison to cell adhesion, viability and proliferation with NIH 3T3 fibroblasts and HUVECs. In particular, extensive physicochemical measurements revealed that the presence of Jeffamine® segments in the PAA oligomer produced three main effects: (1) enhanced optical transparency, due to a more homogeneous polymeric network allowing for the monitoring of cellular processes using traditional optical techniques; (2) improvement of the mechanical properties, supposedly due to crystalline domains in the crosslinked network generated by the Jeffamine® segments that increased the hydrogel storage modulus; (3) increased swelling ratio, caused by the intrinsic hydrophilicity of Jeffamine®, that resulted in a high degradation rate which improved the limited degradation ability of PAA crosslinked by free-radical polymerization. Overall these results demonstrated that PJP-4 is a suitable material for the fabrication of cell-laden construct and could ultimately become a tool for the creation of *in vitro* models for tissue engineering application.

2.5 Results and Discussion for PAA based grafting of non-adhesive synthetic polymer

2.5.1 Syntheses of the Comb-Like Polymers: P(HEMA-CO-APM)/PAAs

P(HEMA-co-APM) mother backbone was obtained from a random copolymerization of HEMA and APM. The average molecular weights of P(HEMA-co-APM) were set to be lower than the glomerular filtration molecular weight cut-off (61), using 2-mercaptoethanol as a chain transfer agent. The oligomeric mother backbones P(HEMA-co-APM) were synthesized in molar excess of HEMA, in order to minimize the steric hindrance between the acrylamide-terminated PAA moieties, grafted on P(HEMA-co-APM) by Michael type I addition reaction between the acrylamide functional groups of BAC and the primary amino groups of APM units and agmatine. Grafting of P(HEMA-co-APM) mother backbones by acrylamide-terminated PAA moieties were shown to take place in a selective manner through the primary amino groups (APM units) without involving the primary hydroxide group (HEMA units) and accordingly confirm the success of our synthetic approach. The branching degree (BD) of the three comb-like polymers, prepared in this study, was calculated according to equation reported below (62,63):

$$BD(\%) = [(D+T)/(D+T+L)] \times 100$$

where "*D*", "*T*," and "*L*" are the ratios of branched, terminal, and linear units in the branched polymer, respectively. *D*, *T*, and *L* were estimated, semi-quantitatively, from HNMR spectra of the purified comb-like polymers (data not shown).

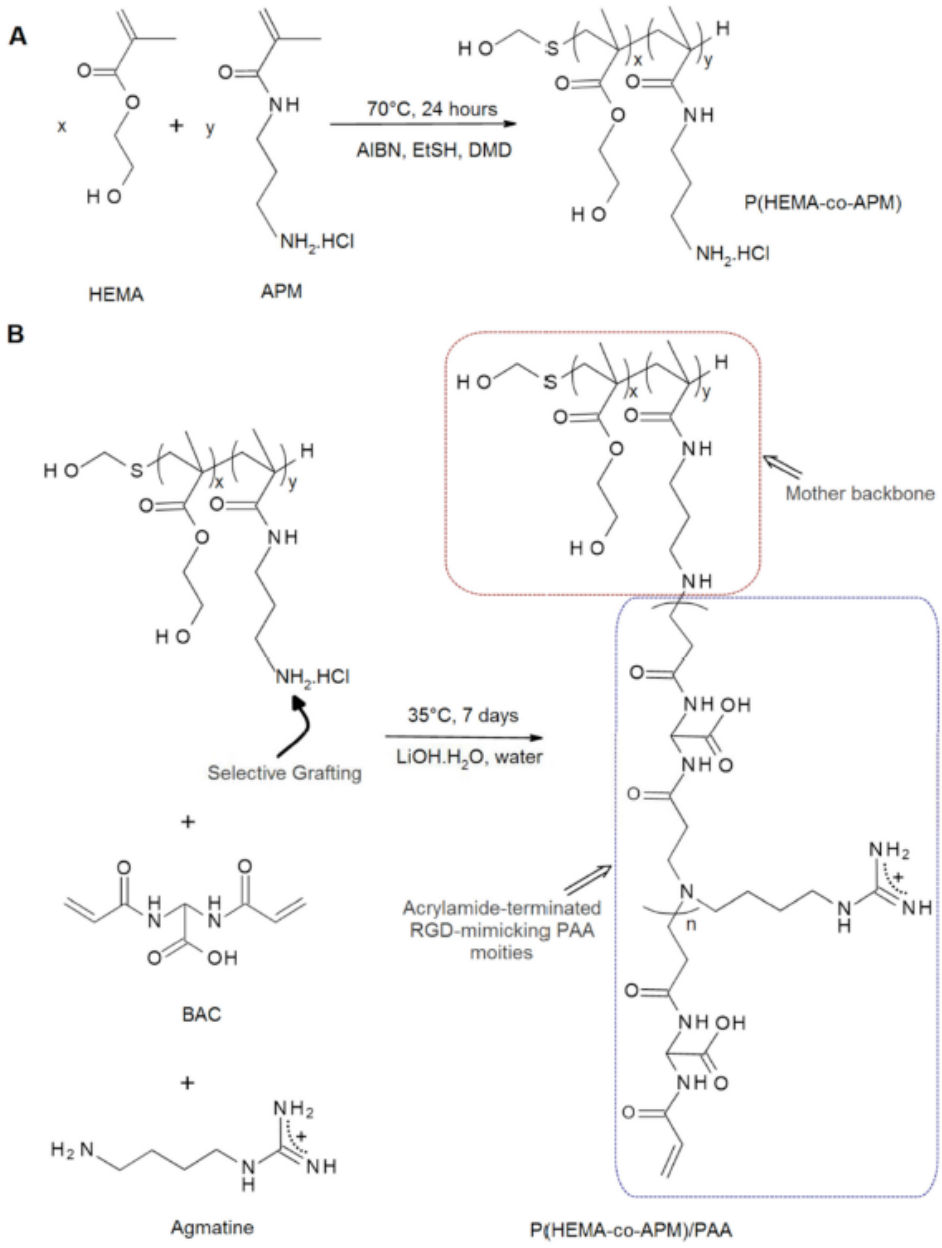

Figure 2-6 Synthetic route for the preparation of P(HEMA-co-APM)/PAA. Synthesis of the oligomeric mother backbone P(HEMA-co-APM) (A). Grafting of the mother backbone with acrylamide-terminated RGD-mimetic PAA moieties by Michael type addition reaction, between the amine functional groups of APM units of P(HEMA-co-APM), agmatine and BAC, in basic aqueous solution (B).

2.5.2 Mechanical Properties

Herein we investigated the role played by the mother backbone P(HEMA-co-

APM) on the modulation of the mechanical properties of P(HEMA-co-APM)/PAA hydrogels. Whereas we demonstrated experimentally that the grafting process takes place selectively through APM units, we assumed that slight variations of the BD might affect the mechanical properties of the photo-cross-linked hydrogels, due to variations of the hydrogels mesh size (64). For this purpose, a screening compression test was carried out on a series of comb-like polymers, where the mother backbones have different ratios between HEMA and APM. Results show that the Young's modulus of P(HEMA-co-APM)/PAA hydrogels is directly related to the BD of the polymeric precursors (Figures 2-7 A–C, Table 2). Moreover, we investigated the role of the PHEMA-based mother backbone on the mechanical integrity of P(HEMA-co-APM)/PAA hydrogels by comparing their Young's moduli to that of PAAdiAc hydrogel, at crescent concentrations (Figure 2-7 C). Results demonstrated that P(HEMA-co-APM)/ PAA hydrogels were stiffer than PAAdiAc ones at all of the concentrations. We have also observed that firm hydrogels could be obtained by photo-cross-linking of P($HEMA_{77}$- co-APM_{23})/PAA even at the concentration of 5% (w/v) (Young's modulus = 6.8 ±0.25), while it was not possible to do the same for up to 15% (w/v) in case of PAAdiAc (Figure 2-7 C). These results, align with literature, where it was demonstrated that hydrogen bonding between HEMA hydroxide groups can play a significant role in the reinforcement of the macromolecular network and hence the enhancement of their mechanical integrity (65-67). This effect was shown to depend also on the polymer concentration in solution (68-71).

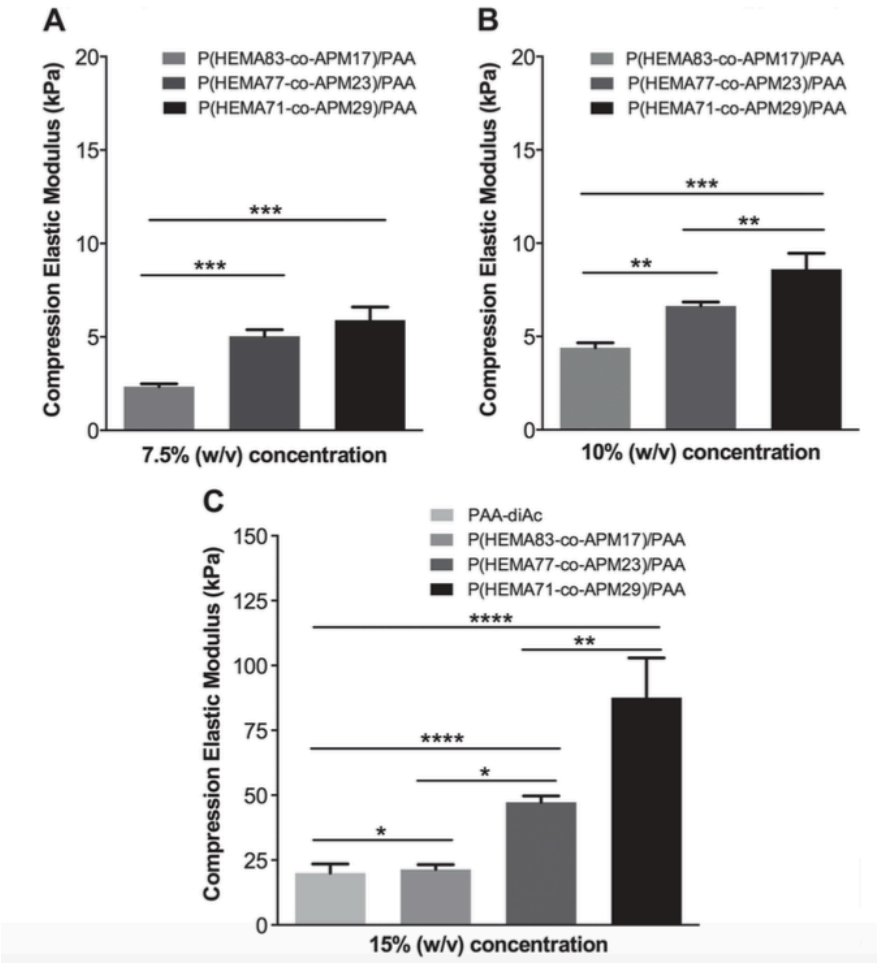

Figure 2-7 Compression elastic modulus (kPa) of P(HEMA-co-APM)/PAA and PAAdiAc hydrogels, obtained from photo-cross-linking polymers solutions in PBS 1× at 7.5 (A), 10 (B), and 15% (w/v) (C).

2.5.3 Degradation Kinetics

According to previous studies, degradation kinetics should be finely tuned in order to guarantee an adequate mechanical support for the encapsulated cells during the early stages of growth and proliferation. Indeed, the hydrogel network should primarily allow and support the extracellular matrix deposition, influencing therefore cells viability and differentiation (72,73). Degradation kinetics of P(HEMA-co-APM)/PAA hydrogels was investigated for the three comb-like polymers: P($HEMA_{83}$-co-APM_{17})/PAA, P($HEMA_{77}$-co-APM_{23})/PAA and P($HEMA_{71}$-co-APM_{29})/PAA, at the concentrations: 5, 7.5, 10% and 15% (w/w). P(HEMA- co-APM)/PAA hydrogels underwent gradual weight loss, by hydrolytic degradation of the agmatine-containing PAA segments (74). After 1 month, P(HEMA-co-APM)/PAA hydrogels lost 7% to 32% of their initial weight, depending on the BD and the concentration of the comb-like

polymers in solution (Figure 2-8). Hydrogels prepared from low-BD com-like polymers (for example: P(HEMA$_{83}$-co-APM$_{17}$)/ PAA) degraded faster than those obtained from high-BD ones, at the same concentrations. Results also show that lowering the concentration of the polymeric precursor in solution accelerates degradation kinetics (75,76). This double-control (i.e., the BD and the concentration of the polymeric precursor) allows fine tuning of the degradation kinetics of P(HEMA-co-APM)/PAA hydrogels. The degradation kinetics and compression properties of P(HEMA-co-APM)/PAAs render these matrixes a good candidate for the encapsulation of chondrocytes and for the regeneration of cartilaginous tissue (77,78).

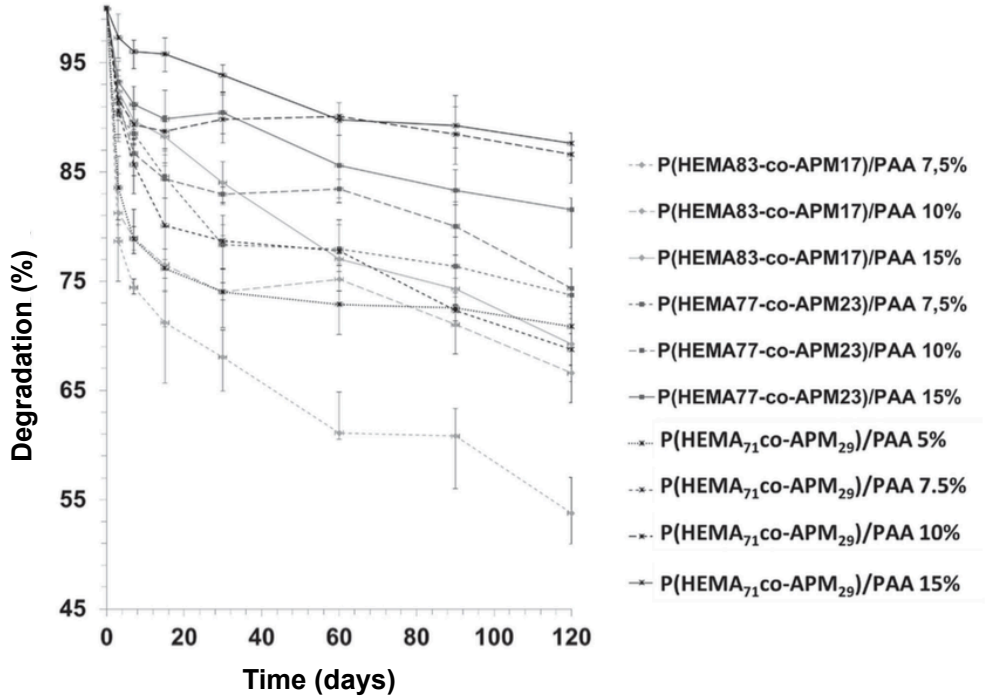

Figure 2-8 Degradation kinetics of the P(HEMA-co-APM)/PAA hydrogels, obtained from photo-cross-linking of the comb-like polymer solutions, in PBS 1×, at 5, 7.5, 10, 15% (w/w).

2.5.4 *IN VITRO* 3D CELL CULTURE

To assess *in vitro* 3D cell encapsulation capability of P(HEMA-co-APM)/PAA hydrogels, encapsulated cell behaviour was studied with 3T3 NIH cell line (Figure 2-9). In these experiments NIH 3T3 fibroblasts were encapsulated in 0.3 mm thickness and 10 mm diameter slab of P(HEMA-co-APM)/PAAs at the concentration of 15% (w/w). Photo-cross-linked PAAdiAc hydrogel could not be tested, as control, in 3D cell encapsulation experiments because of their poor optical transparency that hinder viability assay with confocal microscopy. We

chose Gelatine methacrylate GelMa hydrogels, a widely studied matrix for cell encapsulation, as a control for 3D cell culture in P(HEMA-co-APM)/PAAs, under the same experimental conditions (79). 3T3NIH cells viability was investigated qualitatively and semi-quantitatively through live/dead staining. After 48 h from encapsulation, the majority of the cells were viable in all gel conditions (Figures 2-9 A–D). We did not observe statistically significant differences between the control and our hydrogels (Figure 2-9 E). Therefore, these results confirm that P(HEMA-co-APM)/PAA hydrogels provide an appropriate 3D environment for cell encapsulation.

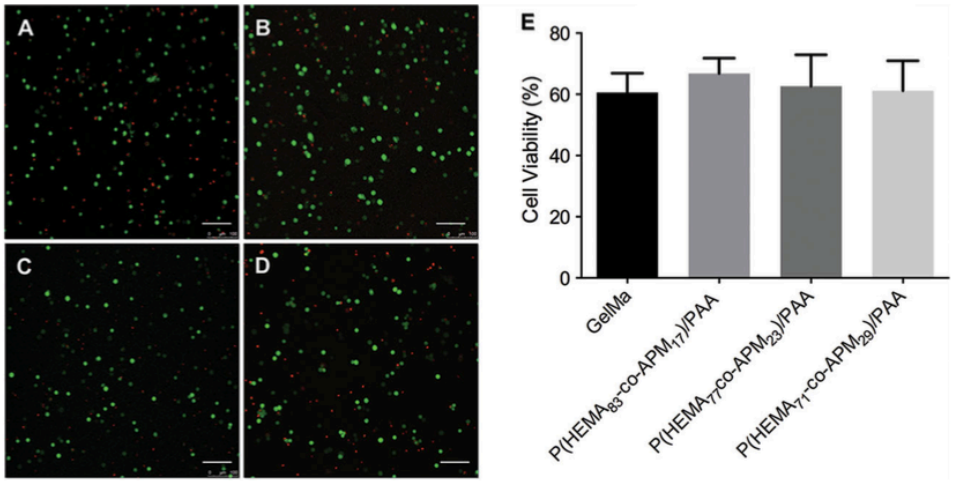

Figure 2-9 Confocal microscopy images, live/dead assay (green and red respectively) for 3T3-NIH fibroblast cells 48 h after encapsulation in different hydrogels substrates. A) GelMa, B) P(HEMA$_{83}$-co-APM$_{17}$)/PAA, C) P(HEMA$_{77}$co-APM$_{23}$)/PAA, and D) P(HEMA$_{71}$-co-APM$_{29}$)/PAA, (scale bar, 100 μm). Quantification of encapsulated cells viability for the different hydrogels at 48 h. E) Cell viability (%) after 48 h of encapsulation in GelMa and P(HEMA-co-APM) hydrogels: no significant difference between groups were observed.

2.5.5 Conclusions

In this study, a new polymeric precursor for cell encapsulation was successfully synthesized by selective grafting of P(HEMA-co-APM) mother backbone with RGD-mimetic PAA. We demonstrated that it is possible to finely tune the compression properties and degradation kinetics of the photo-cross-linked hydrogels P(HEMA-co-APM)/ PAA varying the molar ratio between the HEMA and APM co-monomers in the reactive mixture of the oligomeric mother backbone. Furthermore, we assessed the important role of the PHEMA-based mother backbone in the enhancement of the mechanical integrity of P(HEMA-co-

APM)/PAA hydrogels.

Ultimately, the polymeric precursor presented in this study showed to be compatible with cell encapsulation. We believe that our material could be used for the *in situ* gelling, overcoming the current limits of natural polymers, thanks to the possibility to finely tune degradation kinetics and mechanical properties in addition to the low production costs.

2.6 SUMMARY

In this chapter we presented two different approaches for the fabrication of RGD-mimetic PAA based hydrogels. Although PAA based hydrogels previously proved to have promising biological properties, they were affected by several limitations such as poor mechanical integrity and degradation properties. On the other hand, thanks to their chemistry, PAAs can be easily modified adding different co-monomers such as Jeffamine, as reported in the section 2.1, or can be used as a source of inexpensive adhesive binding sites using the grafting strategy, reported in the section 2.2. In this chapter, we demonstrated that with our approaches it is possible to tune the mechanical properties of our hydrogels keeping the adhesive properties typical of pure PAA. Mechanical stimuli and cell adhesion signals are two key parameters in the complex interplay between cells and ECM *in vivo*. Therefore, we believe that our platform of hydrogels could become a useful tool for the creation of tissue-like structure to be used as *in vitro* models to understand the complex mechanism underlying cell-ECM interaction.

2.7 REFERENCES

[1] Abbott A. Cell culture: biology's new dimension. Nature 2003;424:870–2.

[2] Cukierman E, Pankov R, Stevens DR, Yamada KM. Taking cell-matrix adhesions to the third dimension. Science 2001;294:1708–12.

[3] Baker BM, Chen CS. Deconstructing the third dimension: how 3D culture microenvironments alter cellular cues. J Cell Sci 2012;125(13):3015–24.

[4] Khademhosseini A, Langer R, Borenstein J, Vacanti JP. Microscale technologies for tissue engineering and biology. Proc Natl Acad Sci USA 2006;103(8):2480–7.

[5] DeForest CA, Anseth KS. Advances in bioactive hydrogels to probe and direct cell fate. Annu Rev Chem Biomol Eng 2012;3:421–44.

[6] Astashkina A, Mann B, Grainger DW. A critical evaluation of in vitro cell

culture models for high-throughput drug screening and toxicity. Pharmacol Ther 2012;134(1):82–106.

[7] Nyga A, Cheema U, Loizidou M. 3D tumour models: novel in vitro approaches to cancer studies. J Cell Commun Signal 2011;5(3):239–48.

[8] Engler AJ, Sweeney HL, Discher DE, Schwarzbauer JE. Extracellular matrix elasticity directs stem cell differentiation. J Musculoskelet Neuronal Interact 2007;7(4):335.

[9] Engler AJ, Sen S, Sweeney HL, Discher DE. Matrix elasticity directs stem cell lineage specification. Cell 2006;126(4):677–89.

[10] Tsang LV, Chen AA, Cho LM, Jadin KD, Sah RL, DeLong S, et al. Fabrication of 3D hepatic tissues by additive photopatterning of cellular hydrogels. FASEB J 2007;21(3):790–801.

[11] Du Y, Lo E, Ali S, Khademhosseini A. Directed assembly of cell-laden microgels for fabrication of 3D tissue constructs. Proc Natl Acad Sci USA 2008;105(28):9522–7.

[12] Murtuza B, Nichol JW, Khademhosseini A. Micro- and nanoscale control of the cardiac stem cell niche for tissuefabrication. Tissue Eng Part B Rev 2009;15(4):443–54.

[13] Burdick JA, Vunjak-Novakovic G. Engineered microenvironments for controlled stem cell differentiation. Tissue Eng Part A 2009;15(2):205–19.

[14] Huang G, Wang L, Wang S, Han Y, Wu J, Zhang Q, et al. Engineering three-dimensional cell mechanical microenvironment with hydrogels. Biofabrication 2012;4(4):042001.

[15] Grinnell F. Fibroblast biology in three-dimensional collagen matrices. Trends Cell Biol 2003;13:264–9.

[16] Eyrich D, Brandl F, Appel B, Wiese H, Maier G. Long-term stable fibrin gels for cartilage engineering. Biomaterials 2007;28:55–65.

[17] Ho ST, Cool SM, Hui JH, Hutmacher DW. The influence of fibrin based hydrogels on the chondrogenic differentiation of human bone marrow stromal cells. Biomaterials 2010;31:38–47.

[18] Khademhosseini A, Eng G, Yeh J, Fukuda J, Blumling 3rd J, Langer R, Burdick JA. Micromolding of photocrosslinkable hyaluronic acid for cell encapsulation and entrapment. J Biomed Mater Res A 2006;79(3):522–32.

[19] Brigham MD, Bick A, Lo E, Bendali A, Burdick JA, Khademhosseini A.

Mechanically robust and bioadhesive collagen and photocrosslinkable hyaluronic acid semi-interpenetrating networks. Tissue Eng Part A 2009;15(7):1645–53.
[20] Kleinman HK, Martin GR. Matrigel: basement membrane matrix with biological activity. Semin Cancer Biol 2005;15:378–86.
[21] Hughes CS, Postovit LM, Lajoie GA. Matrigel: a complex protein mixture required for optimal growth of cell culture. Proteomics 2010;10:1886–90.
[22] Nichol JW, Koshy ST, Bae H, Hwang CM, Yamanlar S, Khademhosseini A. Cell- laden microengineered gelatin methacrylate hydrogels. Biomaterials 2010;31(21):5536–44.
[23] Münster S, Jawerth LM, Leslie BA, Weitz JI, Fabry B, Weitz DA. Strain history dependence of the nonlinear stress response of fibrin and collagen networks. Proc Natl Acad Sci USA 2013;110(30):12197–202.
[24] Lee B, Zhou X, Riching K, Eliceiri KW, Keely PJ, Guelcher SA, et al. A three- dimensional computational model of collagen network mechanics. PLoS ONE 2014;9(11):e111896.
[25] Ferruti P, Marchisio MA, Duncan R. Poly(amido-amine)s: biomedical applications. Macromol Rapid Commun 2002;23:332–55.
[26] Jain R, Standley SM, Frechet JMJ. Synthesis and degradation of pH-sensitive linear poly(amidoamine)s. Macromolecules 2007;40:452–7.
[27] Emilitri E, Ranucci E, Ferruti P. New poly(amidoamine)s containing disulfide linkages in their main chain. J Polym Sci Pol Chem 2005;43:1404–16.
Lavignac N, Lazenby M, Franchini J, Ferruti P, Duncan R. Synthesis and preliminary evaluation of poly(amidoamine)-melittin conjugates as endosomolytic polymers and/or potential anticancer therapeutics. Int J Pharm 2005;300:102–12.
[28] Lavignac N, Lazenby M, Franchini J, Ferruti P, Duncan R. Synthesis and preliminary evaluation of poly(amidoamine)-melittin conjugates as endosomolytic polymers and/or potential anticancer therapeutics. Int J Pharm 2005;300:102–12.
[29] Magnaghi V, Conte V, Procacci P, Pivato G, Cortese P, Cavalli E, et al. Biological performance of a novel biodegradable polyamidoamine hydrogel as guide for peripheral nerve regeneration. J Biomed Mater Res 2011;98(1):19–30.
[30] Lin C, Zhong Z, Lok MC, Jiang X, Hennink WE, Feijen J, et al. Novel bioreducible poly(amido amine)s for highly efficient gene delivery. Bioconjug Chem 2007;18:138–45.
[31] Emilitri E, Guizzardi F, Lenardi C, Suardi M, Ranucci E, Ferruti P. Novel

poly(amidoamine)-based hydrogels as scaffolds for tissue engineering. Macromol Symp 2008;266:41–7.

[32] Dos Reis G, Fenili F, Gianfelice A, Bongiorno G, Marchesi D, Scopelliti PE, et al. Direct microfabrication of topographical and chemical cues for the guided growth of neural cell networks on polyamidoamine hydrogels. Macromol Biosci 2010;10:842–52.

[33] Martello F, Piest M, Engbersen JF, Ferruti P. Effects of branched or linear architecture of bioreducible poly(amido amine)s on their in vitro gene delivery properties. J Control Release 2012;164:372–9.

[34] Mauro N, Ranucci E, Procacci P, Laus M, Antonioli D, Mantovani C, et al. Degradable poly(amidoamine) hydrogels as scaffolds for in vitro culturing of peripheral nervous system cells. Macromol Biosci 2012;13:332–47.

[35] Ferruti P, Bianchi S, Ranucci E, Chiellini F, Piras AM. Novel agmatine-containing poly(amidoamine) hydrogels as scaffolds for tissue engineering. Biomacromolecules 2005;6:2229–35.

[36] Yeo Y, Geng W, Ito T, Kohane DS, Burdick JA, Radisic M. Photocrosslinkable hydrogel for myocyte cell culture and injection. J Biomed Mater Res B Appl Biomater 2007;81(2):312–22.

[37] Yang F, Williams CG, Wang DA, Lee H, Manson PN, Elisseeff J. The effect of incorporating RGD adhesive peptide in polyethylene glycoldiacrylate hydrogel on osteogenesis of bone marrow stromal cells. Biomaterials 2005;26(30): 5991–8.

[38] Ruoslahti E. RGD and other recognition sequences for integrins. Annu Rev Cell Dev Biol 1996;12:697–715.

[39] West JL, Hubbell JA. Polymeric biomaterials with degradation sites for prote- ases involved in cell migration. Macromolecules 1999;32:241–4.

[40] Gobin AS, West JL. Cell migration through defined, synthetic ECM analogs. FASEB J 2002;16:751e3.

[41] Mann BK, Gobin AS, Tsai AT, Schmedlen RH, West JL. Smooth muscle cell growth in photopolymerized hydrogels with cell adhesive and proteolytically degradable domains: synthetic ECM analogs for tissue engineering. Biomaterials 2001;22(22):3045–51.

[42] Burdick JA, Anseth KS. Photoencapsulation of osteoblasts in injectable RGD- modified PEG hydrogels for bone tissue engineering. Biomaterials

2002;23: 4315–23.

[43] Raeber GP, Lutolf MP, Hubbell JA. Molecularly engineered PEG hydrogels: a novel model system for proteolytically mediated cell migration. Biophys J 2005;89(2):1374–88.

[44] Miller JS, Shen CJ, Legant WR, Baranski JD, Blakely BL, Chen CS. Bioactive hydrogels made from step-growth derived PEG-peptide macromers. Biomaterials 2010;31:3736–43.

[45] Benton JA, Fairbanks BD, Anseth KS. Characterization of valvular interstitial cell function in three dimensional matrix metalloproteinase degradable PEG hydrogels. Biomaterials 2009;30(34). 6593-03.

[46] Kraehenbuehl TP, Zammaretti P, Van der Vlies AJ, Schoenmakers RG, Lutolf MP, Jaconi ME, et al. Three-dimensional extracellular matrix-directed cardioprogenitor differentiation: systematic modulation of a synthetic cell-responsive PEG-hydrogel. Biomaterials 2008;29(18):2757–66.

[47] Seliktar D, Zisch AH, Lutolf MP, Wrana JL, Hubbell JA. MMP-2 sensitive, VEGF- bearing bioactive hydrogels for promotion of vascular healing. J Biomed Mater Res A 2004;68(4):704–16.

[48] Lutolf MP, Weber FE, Schmoekel HG, Schense JC, Kohler T, Müller R, et al. Repair of bone defects using synthetic mimetics of collagenous extracellular matrices. Nat Biotechnol 2003;21(5):513–8.

[49] Zhang Y, Wang S, Eghtedari M, Motamedi M, Kotov NA. Inverted-colloidal-crystal hydrogel matrices as three-dimensional cell scaffolds. Adv Funct Mater 2005;15(5):725–31.

[50] Karpushkin E, Duskova-Smrckova M, Remmler T, Lapcikova M, Dusek K. Rheological properties of homogeneous and heterogeneous poly (2-hydroxyethyl methacrylate) hydrogels. Polym Int 2012;61:328–36.

[51] Martello F, Tocchio A, Tamplenizza M, Gerges M, Pistis V, Recenti V, et al. Poly(amidoamine)-based hydrogels with tailored mechanical properties and degradation rates for tissue engineering. Acta Biomater 2014;10(3):1206–15.

[52] Discher DE, Mooney DJ, Zandstra PW. Growth factors, matrices, and forces combine and control stem cells. Science 2009;324(5935):1673–7.

[53] Khademhosseini A, Vacanti JP, Langer R. Progress in tissue engineering. Sci Am 2009;300(5):64–71.

[54] Lutolf MP, Lauer-Fields JL, Schmoekel HG, Metters AT, Weber FE, Fields

GB, et al. Synthetic matrix metalloproteinase-sensitive hydrogels for the conduction of tissue regeneration: engineering cell-invasion characteristics. Proc Natl Acad Sci USA 2003;100(9):5413–8.

[55] E. Degiannis, D. M. Bowley, M. D. Smith, *Injury* 2004, *35*, 474.

[56] J. Yeh, Y. Ling, J. M. Karp, J. Gantz, A. Chandawarkar, G. Eng, J. Blumling, R. Langer, A. Khademhosseini, *Biomaterials* 2006, *27*, 5391.

[57] O. Jeon, S. J. Song, K. J. Lee, M. H. Park, S. H. Lee, S. K. Hahn, S. K. S. Kim, B. S. Kim, *Carbohydr. Polym.* 2007, *70*, 251.

[58] J. W. Nichol, S. T. Koshy, H. Bae, C. M. Hwang, S. Yamanlar, A. Khademhosseini, *Acta Biomater.* 2010, *31*, 5536.

[59] J. Ramón-Azcón, S. Ahadian, R. Obregón, G. Camci-Unal, S. Ostrovidov, V. Hosseini, V. H. Kaji, K. Ino, H. Shiku, A. Khademhosseini, T. Matsue, *Lab Chip* 2012, *12*, 2959.

[60] P. Ferruti, M. A. Marchisio, R. Barbucci, *Polymer* 1985, *26*, 1336.

[61] C. J. Lote, *Principles of Renal Physiology*, 4th ed., Chapman & Hall, London 2000.

[62] C. J. Hawker, R. Lee, J. M. Frechet, *J. Am. Chem. Soc.* 1991, *113*, 4583.

[63] B. Zhang, X. Ma, W. Murdoch, M. Radosz, Y. Shen, *Biotechnol. Bioeng.* 2013, *110*, 990.

[64] T. Canal, N. A. Peppas, *J. Biomed. Mater. Res.* 1989, *23*, 1183.

[65] T. Gan, Y. Zhang, Y. Guan, *Biomacromolecules* 2009, *10*, 1410.

[66] K. Cai, Y. Huang, J. Yang, *J. Eur. Ceram. Soc.* 2005, *25*, 1089.

[67] D. M. Bigg, *Polym. Eng. Sci.* 1988, *28*, 830.

[68] K. S. Anseth, C. N. Bowman, L. Brannon-Peppas, *Biomaterials* 1996, *17*, 1647.

[69] K. Y. Lee, J. A. Rowley, P. Eiselt, E. M. Moy, K. H. Bouhadir, D. J. Mooney, *Macromolecules* 2000,*33*, 4291.

[70] O. Jeon, K. H. Bouhadir, J. M. Mansour, E. Alsberg, *Biomate- rials* 2009, *30*, 2724.

[71] S. P. Zustiak, J. B. Leach, *Biomacromolecules* 2010, *11* , 1348.

[72] P. M. Kharkar, K. L. Kiick, A. M. Kloxin, *Chem. Soc. Rev.* 2013, *42*, 7335.

[73] A. Raza, L. Chien-Chi, *Macromol. Biosci.* 2013, *13*, 1048.

[74] P. Ferruti, J. Franchini, M. Bencini, E. Ranucci, G. P. Zara, L. Serpe, *Biomacromolecules* 2007, *8*, 1498.

[75] A. Metters, H. Jeffrey, *Biomacromolecules* 2005, *6*, 290.

[76] Y. Hong, H. Song, Y. Gong, Z. Mao, C. Gao, J. Shen, *Acta Biomater*. 2007, *3*, 23.

[77] S. J. Bryant, R. J. Bender, K. L. Durand, K. S. Anseth, *Biotechnol. Bioeng*. 2004, *86*, 747.

[78] S. J. Bryant, K. A. Davis-Arehart, N. Luo, R. K. Shoemaker, J. A. Arthur, K. S. Anseth, *Macromolecules* 2004, *37*, 6726.

[79] Y. C. Chen, R. Z. Lin, H. Qi, Y. Yang, H. Bae, J. M. Melero-Martin, A. Khademhosseini, *Adv. Funct.Mater*. 2012, *22*, 2027.

CHAPTER 3

3 BIOLOGICALLY AND MECHANICALLY DRIVEN DESIGN OF AN RGD-MIMETIC MACROPOROUS FOAM FOR ADIPOSE TISSUE ENGINEERING APPLICATIONS

Eleonora Rossi [a,b,c,d] et al.

a) SEMM, European School of Molecular Medicine, Campus IFOM-IEO, Via Adamello 16, 20139 Milano, Italy. b) Filarete Foundation, Viale Ortles 22/4, 20139 Milano, Italy. c) Department of Biomedicine, University Hospital of Basel, Hebelstrasse 20, 4031 Basel, Switzerland.

This chapter has been published:

Eleonora Rossi; Irini Gerges; Alessandro Tocchio; Margherita Tamplenizza; Paola Aprile; Camilla Recordati; Federico Martello; Ivan Martin; Paolo Milani; Cristina Lenardi. "Biologically and mechanically driven design of an RGD-mimetic Macroporous Foam for Adipose Tissue Engineering Applications". Biomaterials, 2016.

3.1 INTRODUCTION

Current clinical treatments in adipose tissue reconstruction, specifically for breast tissue, rely on commercially available fillers or autologous tissue flaps implantations (1). Despite these techniques have a certain grade of efficacy they are still challenged by drawbacks such as donor-site morbidity and volume loss over time (2, 3). Adipose tissue engineering is an emerging field that aim to address the clinical need of human tissue replacements in case of trauma or tumour resection (2). In this contest, tissue engineering, together with biomaterial science, may offer valuable solutions for the design of a scaffolding biomaterial able to match the specific requests for adipose tissue reconstruction in clinical applications, namely to allow host cell adhesion and proliferation (4, 5), support vascular network formation and maintenance (6, 7), mimicking the 3D structure and mechanical properties of the adipose tissue (6, 8).

However, several scaffolding biomaterials used to investigate the regeneration of adipose tissue were not specifically designed for this purpose. In fact, a strategy to recapitulate a suitable environment for adipose tissue reconstruction is still missing.

To date, both natural and synthetic materials have been tested to form new adipose tissue. On one hand, the use of natural materials offers advantages in terms of biocompatibility and biological properties as reported in studies investigating naturally derived scaffold made of collagen (9), fibrin (10), silk protein (11) and adipose decellularized extracellular matrix (ECM) (12). Unfortunately, the application of natural materials in clinics is still hampered by possible undesirable immune response, deriving from their allogenic or xenogenic origin, and the presence of impurities and endotoxins, depending on large-scale isolation techniques (13). On the other hand, synthetic polymers gather a series of advantages such as: versatility, low batch-to-batch variability, controlled degradability and adequate mechanical properties (14). In fact, well known polymers such as poly(glycolic acid) (15), poly(lactic-co-glycolic acid) (16) and polyethylene glycol diacrylate (17) have been used for 3D meshes, scaffolds, and/or grafts for *in vitro* and *in vivo* studies showing to be appropriate supports for adipogenesis (6).

In general, expensive surface design or chemical modifications (e.g. using RGD tripeptide) are required in order to improve cell adhesion capacity of synthetic materials (18-22). It has been shown that cell adhesion properties of synthetic polymers can be improved through co-polymerization with agmatine (23) as the guanidine moieties can be well recognized by RGD-dependent receptors, such as integrins, due to the similar chemical structure that share with the RGD-tripeptide. This approach boosted the use of synthetic polymers in tissue engineering, offering an alternative solution to promote cell adhesion, avoiding expensive modification with RGD tripeptide. Among synthetic biomaterials, the Agmatine-containing cross-linked poly(amidoamine)s (PAAs), showed excellent capacity to promote cell adhesion and proliferation on its surface (24, 25). Recently, we developed a wide library of Agmatine containing PAA based hydrogels (26, 27), characterized by enhanced mechanical properties and degradation kinetics. In particular, hydrogels obtained by free radical polymerization of diacrylamide-terminated poly(amidoamine)s oligomers (OPAA), containing RGD-mimetic

repeating units, showed excellent capacity to promote the adhesion of Madin-Darby canine kidney (MDCK) epithelial cells, NIH 3T3 fibroblasts and Human Vein Endothelial cells (HUVEC) in 2D studies (26, 27).

In addition to the cell adhesion properties, a scaffold for adipose tissue engineering should be designed with a high porosity and an interconnected open cell structure, to improve cellular infiltration and viability, enable nutrients mass transport, be structurally robust, and ideally, promote angiogenesis and normal cell signalling processes (28-30). Furthermore, the mechanical properties of a scaffold play fundamental role in cells fate, as reported by several recent works indicating that biomechanical cues can stimulate stem-cell differentiation toward a variety of cell lineages by mimicking the stiffness of the desired tissue (4, 8). For this purpose, a scaffold matching the mechanical properties of adipose tissue, namely having a Young's modulus in the range of 2-4 kPa (31, 32), would be most appropriate.

The specific aim of this work was thus to fabricate an RGD-mimetic macroporous foam specific for adipose tissue reconstruction, designed upon three main criteria: i) the induction of cell infiltration, adhesion and proliferation, ii) the support of in vivo vascularization and iii) the resemblance of native adipose tissue mechanical properties.

Starting from OPAA, we designed a method to fabricate macroporous foam by gas foaming technique, with improved cell infiltration dynamic and nutrient mass transport if compared with the PAA bulk hydrogels. We first hypothesised that we would obtain a sustainable adipogenesis both *in vitro* and *in vivo* by combining the high biocompatibility and adhesive potential of OPAA with a 3D network resembling the complex architecture and mechanical properties of the native tissue. To this purpose, we next extensively investigated the chemico-physical, biological and mechanical properties of our material. In the detail, we evaluated the *in vitro* biocompatibility of OPAAF with epithelial, preadipose and endothelial cells. Furthermore, we assessed OPAAF capability to support both *in vitro* and *in vivo* adipogenesis together with vessels infiltration in a murine model.

3.2 MATERIALS AND METHODS

3.2.1 MATERIALS

4-Aminobutylguanidine sulfate (Agmatine), ammonium persulfate (APS), lithium hydroxide monohydrate (LiOH), hydrochloric acid (HCl), ammonium bicarbonate (NH_4HCO_3) and poly(ethylene glycol) sorbitan monolaurate (Tween®20) were purchased from Sigma-Aldrich at the highest degree of purity available and used as received. Agmatine was purchased from BYOSINTH (Switzerland). Milli-Q grade water was used in all the experiments. Phosphate buffered saline (PBS) 1X contained 2.69 mM KCl, 136.89 mM NaCl, 3.21 mM Na_2HPO_4 and 1.47 mM KH_2PO_4. All solvents were purchased from Sigma-Aldrich and used without further purifications. 2,2'-Bis(acrylamide)acetic acid (BAC) was prepared as previously reported (33) and its purity (99.9%) determined by acid-base titration and by NMR spectroscopy. All biological materials were purchased from Sigma-Aldrich unless otherwise specified.

3.2.2 SYNTHESIS OF DIACRYLAMIDE-TERMINATED POLY(AMIDOAMINE)S OLIGOMER OPAA

In a 50 mL round-bottom flask, equipped with magnetic stirrer, BAC (9.0 g, 44.9 mmol) and LiOH (2.2 g, 51.3 mmol) were dissolved in 15 mL Milli-Q water. Agmatine (7.6g, 32.2 mmol) was then added to the reacting mixture under magnetic stirring. The reaction was kept in dark and proceeded under inert atmosphere at 35°C for one week and stopped by acidification till pH = 4 using HCl 1 M solution. The product was purified by ultrafiltration, using 1000 cut-off semi permeable membrane. OPAA was obtained as fine white powder after freeze-drying using Telstar Cryodos 50 lyophilizer. The reaction Yield was 84%. Average molecular weights (SEC-Pullulane standards): Mn = 2000, Mw = 2600, P.D. Index = 1,3. ^{1}*HNMR (D_2O)*: 1.57 (s, 2H, -C**H**$_2$-CH_2-NH-CNHNH$_2$); 1.70 (s, 2H, -N-CH_2-C**H**$_2$-); 2.71 (s, 2H, -C**H**$_2$-CONH); 3.07 (s, 2H, -C**H**$_2$-NH-CNHNH$_2$); 3.14 (t, 2H, -N-C**H**$_2$-); 3.61 (m, 2H, -NH-C**H**$_2$-$(CH_2)_2$-NHCO-); 5.48-5.68 (m, 2H, C**H**$_2$=CH-CONH-); 6.18(m, 1H, CH_2=C**H**-CONH-).

3.2.3 OPAAF FABRICATION

OPAAF was fabricated by APS-initiated free radical polymerization of OPAA. In the detail, a 25% (w/v) solution of OPAA was prepared in Milli-Q water and Tween®20 was added as a pore opening agent. Subsequently, NH_4HCO_3 was

added to the reactive mixture at 60°C. Open cell foams were obtained by thermal decomposition of NH_4HCO_3 in parallel with the crosslinking reaction initiated by APS. pH of the raw foams were adjusted to neutral, using 0,01M solution of citric acid. Discs of 10 mm diameter and 3 mm height have been cut and soaked at room temperature in 50% (w/w) ethanol aqueous solution for 2 days, and washed, at room temperature, in Milli-Q water on orbital shaker for other 3 days. Samples were then dried from ethanol under reduced pressure (0,01 bar) and UV-sterilized prior to cell seeding.

3.2.4 SCANNING ELECTRON MICROSCOPY

OPAAF's internal morphologically was characterized by a Carl ZEISS-Sigma scanning electron microscope, endowed with EDS-Brucker XFlash 5030-127 eV detector. Samples were dried under reduced pressure (0,01 mbar), for three days, sputter coated by gold/palladium prior to analyses.

3.2.5 SIZE EXCLUSION CHROMATOGRAPHY

Traces were recorded using Toso-Haas 486 columns, Waters 515 HPLC pump and UV detector operating at 230 nm. The mobile phase was 0.1 M Tris buffer saline, pH 8.00 ± 0.05. The follow rate was 1 ml/min. OPAAs average molecular weights were calculated using Pullulane standards.

3.2.6 NUCLEAR MAGNETIC RESONANCE NMR

^{1}HNMR spectra were acquired on Bruker 8 Advance 400 spectrometer, operating at 400.133 MHz.

3.2.7 EQUILIBRIUM SWELLING AND WEIGHT LOSS MEASUREMENTS

Tests were carried out in PBS 1X, using dry cylindrical samples of average weight 70 mg ± 10 mg. Samples were incubated at 37°C and weighed at fixed time intervals. At each time point, the swollen samples were removed from PBS, blotted gently to remove excess PBS. For weight loss measurements, samples were washed in Milli-Q water, to remove PBS from the swollen foams, finally freeze dried and weighted. Swelling capacity and weight loss were calculated according to the following formulas:

$$\text{Swelling degree } \% = (W_s - W_0)*100/W_0 \quad \text{(Equation 1)}$$

$$\text{Weight loss } \% = (W_0 - W_d)*100/W_0 \quad \text{(Equation 2)}$$

Where W_0, W_s and W_d in equations 1 and 2 are the initial, swollen and dried weight respectively.

3.2.8 MECHANICAL CHARACTERIZATION

The OPAAFs were mechanically tested in unconfined compression using a standard materials testing machine with a 5 N load cell (Zwick Z005, Roell, Germany). The test was performed in a phosphate buffered saline (PBS) bath at room temperature on cylindrical specimens (ø = 10 mm, h = 4 mm) previously brought to a swelling plateau. A preload of 0.05 N was applied to ensure that the surfaces of OPAAF were in direct contact with the impermeable loading platens and to ascertain the height of the specimens. A compression test in strain control was performed with a ramp of 0,001 mm/s until 10% of strain and hold until equilibrium was reached (~30–40 min) (34). A series of 4 steps of 10% strain has been applied up to 40% of total strain. Afterwards, a dynamic stimulation of the OPAAF was performed with 200 cycles of cyclic loading respectively at 0.1, 1 and 5 Hz (n=3).

3.2.9 CELL CULTURE AND SEEDING

Canine MDCK cells (NBL-2; ATCC) were cultured in Minimum Essential Medium with Earle's balanced Salts (MEM; Sigma) supplemented with 10% FBS, 2 mM L-Glutamine, 100 units/ml penicillin, 100 µg/mL streptomycin, 1 mM pyruvic acid (sodium salt), 1 g/L D-(+)-Glucose and MEM. Cells were cultured at 37°C in 5% CO_2 95% air-humidified incubator, harvested using 0.05% trypsin, centrifuged and resuspended in basal medium. Each scaffold, of 10 mm diameter and 2 mm thickness, was seeded with $1{,}5x10^6$ cells, resuspended in 100 μL of basal medium. Scaffolds were seeded adding drop-wise cells suspension, then were placed in the incubator for 1 hour to allow cell attachment. Thereafter, 1 mL of corresponding medium was added to each well, and the plates were incubated at 37°C in 5% CO_2 95% air-humidified incubator.

3T3L1 murine embryonic fibroblasts (ATCC-CL-173) were cultured in Dulbecco's Modified Eagle's Medium (DMEM) supplemented with 10% Fetal Bovine Serum (FBS; Sigma-Aldrich), 2 mM L-Glutamine, 100 units/mL penicillin and 100 μg/mL–streptomycin. Cells were cultured at 37°C in 5% CO_2 95% air-humidified incubator, harvested using 0.05% trypsin, centrifuged and resuspended in basal medium. Each scaffold was seeded with $2x10^6$ cells

following the procedure explained above for MDCK cells. Differentiation was induced in confluent cells (7 days after seeding) by replacing DMEM with differentiation media. Differentiation of preadipocytes was initiated with 10 μg/ml insulin, 1 μM dexamethasone, 100 μM indomethacin, and 500 μM 3-isobutyl-1-methyl xanthine (IBMX) (adipogenic induction medium). After 3 days, cells were switched to DMEM complete medium supplemented with 10 μg/ml insulin (adipogenic maintenance medium) for others 7 days with media replacement on every second day.

HUVECs (PromoCell Gmbh, Heidelberg, Germany) were cultured in M199 medium (Sigma-Aldrich) supplemented with 2 mM L-Glutamine, 100 units/mL penicillin and 100 μg/ml streptomycin and freshly added with 20% FBS, 50 ng/mL β-endothelial cell growth factor (ECGF) and 100 μg/mL Heparin. Cells were cultured at 37°C in 5% CO_2 95% air-humidified incubator, harvested using 0.05% trypsin, centrifuged and resuspended in basal medium. Each scaffold was seeded with $1{,}5x10^6$ cells following the procedure explained above for MDCK.

3.2.10 LIVE/DEAD ASSAY

Cellular viability was investigated at 1, 3 and 9 days of culture by using a live/dead assay solution consisting of Calcein-AM (1 μM) and Propidium Iodide (0.1 mM) prepared in PBS. Briefly, samples were rinsed in PBS, immersed in staining solution for 15-20 minutes and incubated at 37°C. Staining solution was removed, samples washed twice with PBS and immersed in PBS before imaging. Live imaging was performed using a confocal microscope (Leica Confocal Microscopy TCS SP5) incubator equipped using 490/515 nm (excitation/emission) for Calcein-AM (Life Technologies) and 535/617 nm (excitation/emission) for propidium iodide. Maximum intensity projection images were obtained using ImageJ software. Cells viability and organization on scaffolds were validated on 3 independent experiments for cell type.

3.2.11 BODIPY STAINING

Constructs were analysed for BODIPY staining for fatty acid during all the phases of adipogenic differentiation (proliferation, induction and maintenance). Constructs were washed with PBS solution, fixed with 4% paraformaldehyde for 30 minutes at room temperature (RT), rinsed with PBS, incubated with BODIPY® (Life Technologies) 5 μM in PBS solution for 30 minutes and finally

stained with DAPI (Life technologies). 3T3L1 positivity for BODIPY staining was evaluated at each phase of adipogenic differentiation on 3 independent experiments.

3.2.12 GENE EXPRESSION ANALYSIS

Total RNA isolation was performed using Quick-RNA Mini Prep (ZYMO RESEARCH, Germany) according to the manufacturer's protocol. RNA measurement at 260 nm was performed using a Nanodrop spectrophotometer (Thermo Scientific). Reverse transcription into cDNA and polymerization was performed using a SuperScript III Reverse Transcriptase Kit (Invitrogen) and a Veriti Thermal Cycler (Life Technologies).

Quantitative real-time reverse transcriptase–polymerase chain reaction (qRT–PCR; Applied Biosystems 7500 Real- Time PCR System, Life Technologies) were carried out to quantify the expression of peroxisome proliferator-activated receptor gamma (PPARγ). Expression levels of gene of interest were normalized to the housekeeping gene glyceraldehyde-3-phosphate dehydrogenase (GAPDH).

3.2.13 IN VIVO BIOCOMPATIBILITY, ADIPOSE AND VASCULAR TISSUE INFILTRATION

Female CD1 mice (Charles River) aged 8 weeks (25-31 g) were used for this study. Under general anaesthesia, a 10 mm-long incision was made in the skin of the medial femoral region. Scaffolds were placed subcutaneously, over the femoral artery, between the inguinal ligament and *hiatus adductorius*, keeping the perfusion of the distal leg intact. Mice were sacrificed 14 and 50 days post implant, and scaffolds, together with surrounding tissues, were excised and fixed in 10% neutral buffered formalin. Formalin-fixed samples were embedded in paraffin wax, sectioned at 4 μm thicknesses, stained with hematoxylin and eosin (HE), and evaluated under a light microscope for the assessment of host reaction and adipose tissue ingrowth.

For the evaluation of macrophagic infiltrate and vascularization, sections were immunostained for Iba1 and CD31, respectively. Sections were deparaffinised in xylol, rehydrated through graded ethanols, and rinsed in distilled water. Endogenous peroxidase activity was blocked by incubating sections in 3% H_2O_2 for 15 min. Antigen retrieval was performed using citrate buffer pH 6 in a pressure cooker. Slides were rinsed and treated with PBS containing 10% normal

rabbit or goat serum for 30 min to reduce nonspecific background staining and then incubated for 1 hour at room temperature with the following primary antibodies: rat monoclonal anti-CD31 (Dianova, clone SZ31), and rabbit polyclonal anti-Iba1 (Wako). Appropriate biotinylated secondary antibodies (goat anti-rabbit or rabbit anti-rat; Vector Laboratories, Burlingame, CA, USA) were then added for 30 min. Sections were labelled by the avidin-biotin-peroxidase (ABC) procedure with a commercial immunoperoxidase kit (Vectastain Standard Elite, Vector Laboratories). The immunoreaction was observed with 3,3'-diaminobenzidine substrate (DAB, Vector Laboratories) for 10 min and sections were counterstained with Mayer's haematoxylin. Known positive control sections were included in each immunolabeling assay.

For the evaluation of vessels infiltration, sections were immunostained for alpha smooth muscle actin (α-SMA), erythrocytes and nuclei. Sections were deparaffinised, washed in PBS, permeabilized with Triton X-100 0,1% for 5 minutes and blocked with 2% bovine serum albumin (BSA) for 1h at RT. First, α-SMA monoclonal (Sigma Aldrich) was added in 2% BSA solution and slides incubated over night at 4°C. Slides were rinsed in PBS and incubated for 45 minutes at RT with Alexa 546 (Invitrogen) secondary antibody for α-SMA. Alexa 488 (Invitrogen) was added to the mixture to stain a-specifically erythrocytes. Slides were then rinsed in PBS and counterstained with DAPI.

3.2.14 Statistical analysis

Samples were tested at least 4 times and data are expressed as sample arithmetic mean ± standard deviation. The significance of differences was determined by Ordinary one-way ANOVA (*$p \leq 0.05$, **$p \leq 0.005$, ***$p \leq 0.0005$).

3.3 Results

3.3.1 OPAAF synthesis and morphology

OPAA oligomers were cross-linked by free radical polymerization, exploiting the unsaturated acrylamide terminal groups, as schematically represented in figures 3-1 A and B. The reaction was initiated by APS in presence of NH_4HCO_3 ammonia gas. The thermal decomposition of NH_4HCO_3, which released NH_3 and CO_2 gas bubbles in the reactive solution, in parallel with cross-linking reaction generated OPAA foam with an interconnected porous structure. Tween® 20, was added as

a non-ionic surfactant in order to enhance bubbles stability and uniformity in the reactive solution (Figure 3-1 C). The foaming method was selected, among other common fabrication techniques, to optimally match OPAA chemistry. In fact, foaming can be performed in water or protic polar solvents and does not require prolonged purification process that may damage the soft scaffold (20). As demonstrated by SEM micrographs (Figures 3-2 A and B), OPAAF's homogeneous morphology is characterized by a highly interconnected primary macroporous structure (average diameter 300-500 μm), through secondary mesopores (average diameter 40-100 μm).

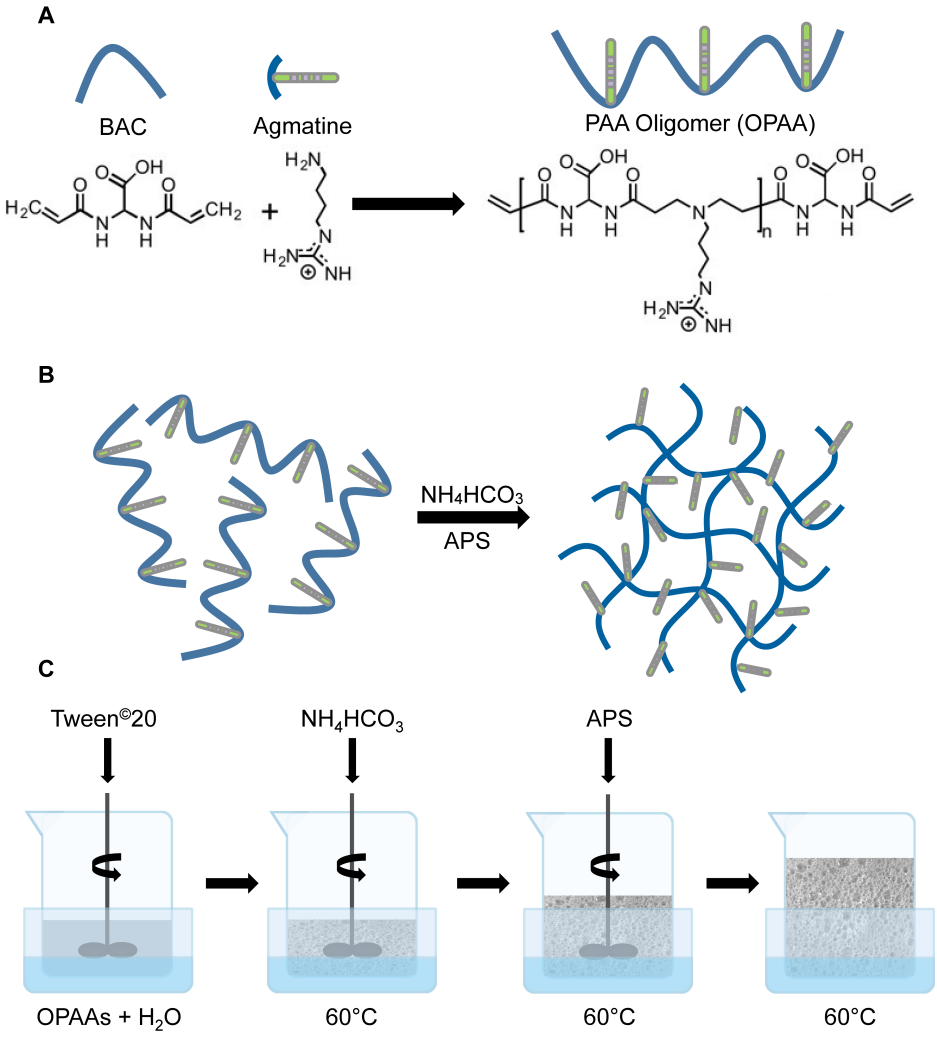

Figure 3-1 Schematic representation of OPAA synthesis and OPAAF fabrication. OPAA chemical structure (A), OPAAF cross-linking by free radical polymerization (B) and 3D fabrication by foaming technique (C).

3.3.2 Swelling Capacity and Degradation Kinetics

OPAAF reached maximum swelling capacity "Plateau" during the first two hours of incubation in PBS 1X at 37°C, and maintained it until the end of the test (72H)

(Figures 3-2 C). Compared to OPAA-based bulk hydrogels (26), OPAAF's water uptake capacity is higher, thanks to its wider specific surface area given by the 3D porous structure. OPAAF's degradation kinetics, showed a 35% weight loss during the first month and proceeded gradually to reach 55% within the sixth month of incubation in PBS 1X at 37°C (Figures 3-2 D).

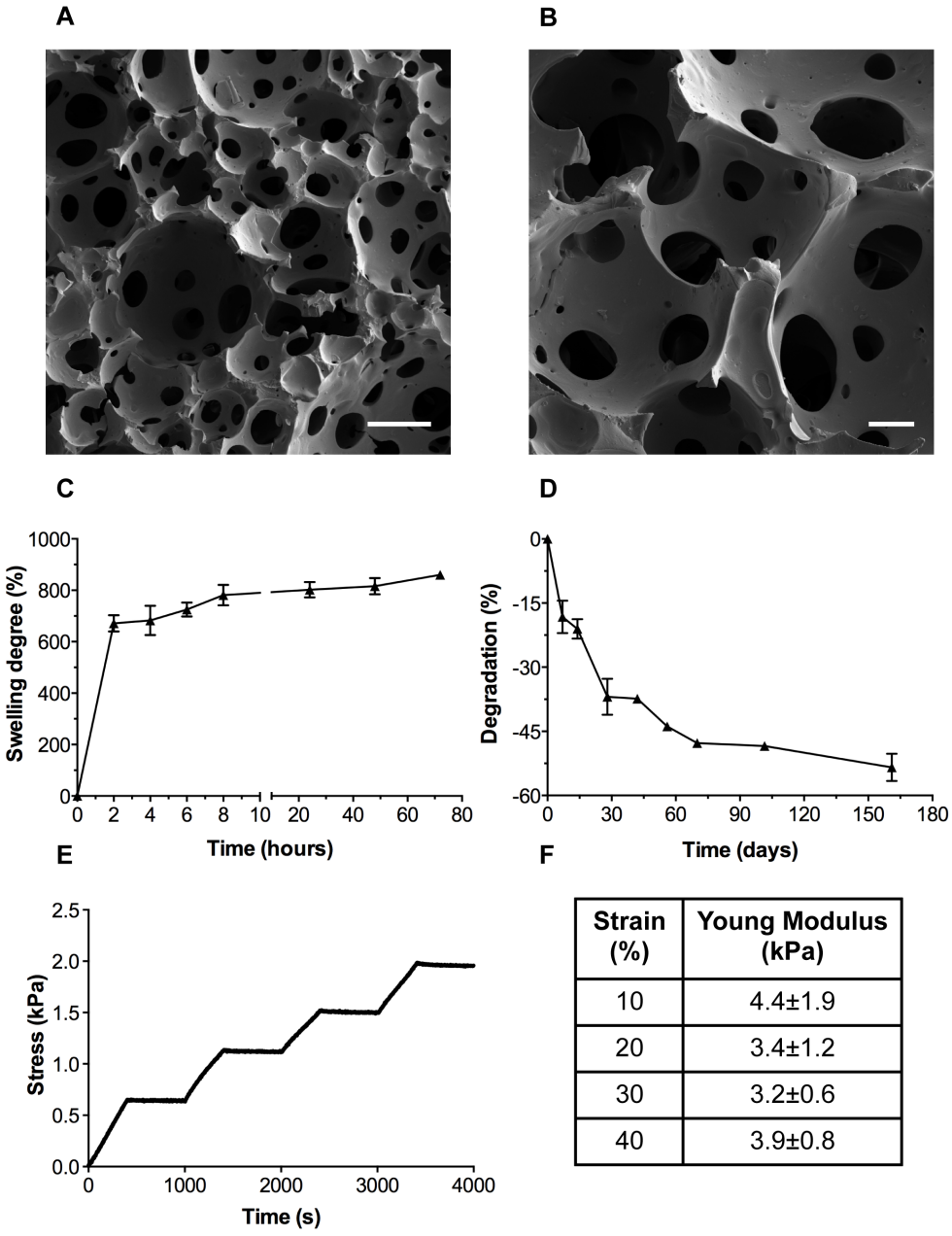

Strain (%)	Young Modulus (kPa)
10	4.4±1.9
20	3.4±1.2
30	3.2±0.6
40	3.9±0.8

Figure 3-2 OPAAF structural and chemico-physical characterization. SEM micrographs of OPAAF (A and B), (scale bars: 200 and 100 μm, respectively). Swelling (C) and degradation kinetics (D) of OPAAF in PBS 1X at 37°C. Mechanical characterization of OPAAF. Representative Stress *vs* Time curve during compression test in controlled strain (E); Table with Young's Moduli at different level of strain (F).

3.3.3 MECHANICAL PROPERTIES

The elastic behaviour of OPAAFs was evaluated with a compression test on the fully swollen scaffolds, at strain values of 10, 20, 30 and 40% in order to investigate scaffold's stiffness in response to progressive deformations. Results from the compressive test showed that the Young's modulus of OPAAFs did not significantly change with the application of increasing strains (Figures 3-2 E). OPAAF was then stimulated with more than 200 cycles of cyclic loading respectively at a frequency of 0.1, 1 and 5Hz to assess the viscoelastic response of the material by observing possible progressive deformation of the scaffold during the dynamic stimulation (Figures 3-3 A-F). Interestingly, OPAAF didn't show the stress relaxation response peculiar of viscoelastic materials (35), at none of the frequencies tested (Figures 3-3 A, C and E). Moreover, the Dynamic, Storage and Loss moduli, together with the Tanδ generally maintained similar values during the cycles of the dynamic stimulation at each frequency tested (Figures 3 B, D and F). The OPAAF's elastic behaviour at high levels of strain and at different frequencies demonstrates the efficacy of the fabrication process. In fact, the reported results suggest a high conversion degree of the cross-linking reaction that favours the scaffolds capability to regain the original shape after deformation. Finally, by comparing the Young's elastic modulus of the foamed OPAA to that of the bulk hydrogels, previously characterized (26), we observed that OPAAF is one fold softer, and hence resembles that of adipose tissue (36). Given that, previous studies evidenced that proper elastic modulus and adequate mechanical support can strongly influence cell morphology and orientation and induce changes in signal transduction system and secondary messengers (8). The designed mechanical characteristics of OPAAF suggested its use for adipose tissue regeneration (32, 36, 37).

A

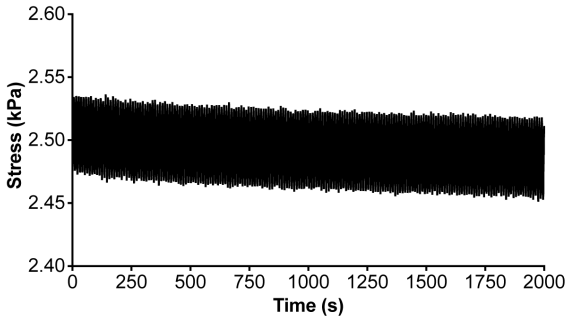

B

Cycle	10	100	200
Dynamic Modulus	8.4±0.6	8.6±0.4	9.2±0.9
Storage Modulus	4.3±0.7	4.4±0.7	4.4±0.7
Loss Modulus	1.9±0.2	1.9±02	2.1±0.1
Tanδ	0.5±0.1	0.4±0.1	0.4±0.1

C

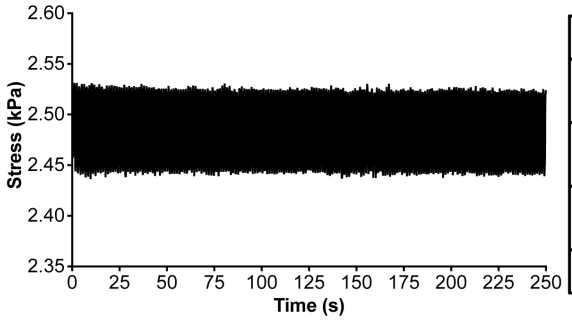

D

Cycle	10	100	200
Dynamic Modulus	9.9±1.3	9.9±1.3	9.8±1.9
Storage Modulus	5.4±0.9	5.4±1.0	5.3±1.1
Loss Modulus	1.8±0.2	1.8±02	1.8±0.1
Tanδ	0.3±0.1	0.3±0.1	0.3±0.1

E

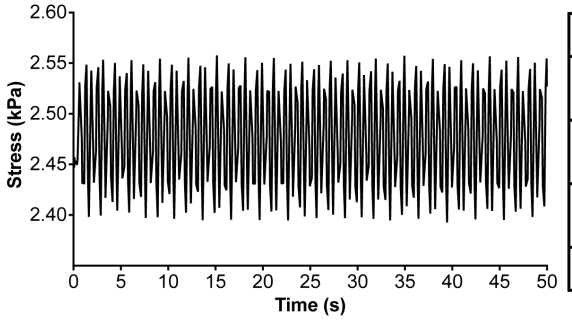

F

Cycle	10	100	200
Dynamic Modulus	8.7±1.8	7.3±2.1	8.9±1.6
Storage Modulus	4.9±1.0	4.7±1.1	5.0±0.8
Loss Modulus	1.8±0.4	1.5±01	1.8±0.1
Tanδ	0.4±0.1	0.3±0.1	0.3±0.1

Figure 3-3 Mechanical characterization of OPAAF. Dynamic mechanical analysis. Representative Stress *vs* Time curve and table with Dynamic, Storage, Loss moduli and Tanδ respectively at 0.1Hz (A and B), 1Hz (C and D) and 5Hz (E ad F). Values reported in the tables are expressed in kPa.

3.3.4 In vitro evaluation of cells adhesion, viability and adipogenesis

OPAA hydrogels previously demonstrated the ability to promote cell adhesion and viability thanks to the RGD-mimetic structure of its repeating units (26, 27). In this work, the biological properties of OPAAF in a 3D cell culture were extensively evaluated, with a focus on the cell-scaffold interactions (cell adhesion, morphology and viability). To this aim MDCK, 3T3L1 and HUVEC cells were cultured on OPAAF. Cell viability was visualized over time by confocal laser

scanning microscopy after live/dead assay (Figures 3-4 and 6). Biological response was determined on OPAAFs with MDCK at 1, 3 and 9 days (Figures 3-4 A-F). After 1 day of culture in OPAAF, MDCK were well attached showing a polygonal-like morphology, typical of adherent phenotype (Figures 3-4 A and B). From day 3 to day 9, cell proliferation and a strong prevalence of live cells on dead cells were observed. At day 9, cells were homogeneously distributed and organized around the pores edges. A spindle-like morphology was observed in the areas around the pores edges, while a polygonal-like morphology is maintained in the centre of the cell layer (Figures 3-4 E and F). Overall these results confirmed OPAAF's good adhesion properties as already showed in the literature with MDCK, NIH 3T3 and HUVEC on OPAA-based bulk hydrogels (26, 27).

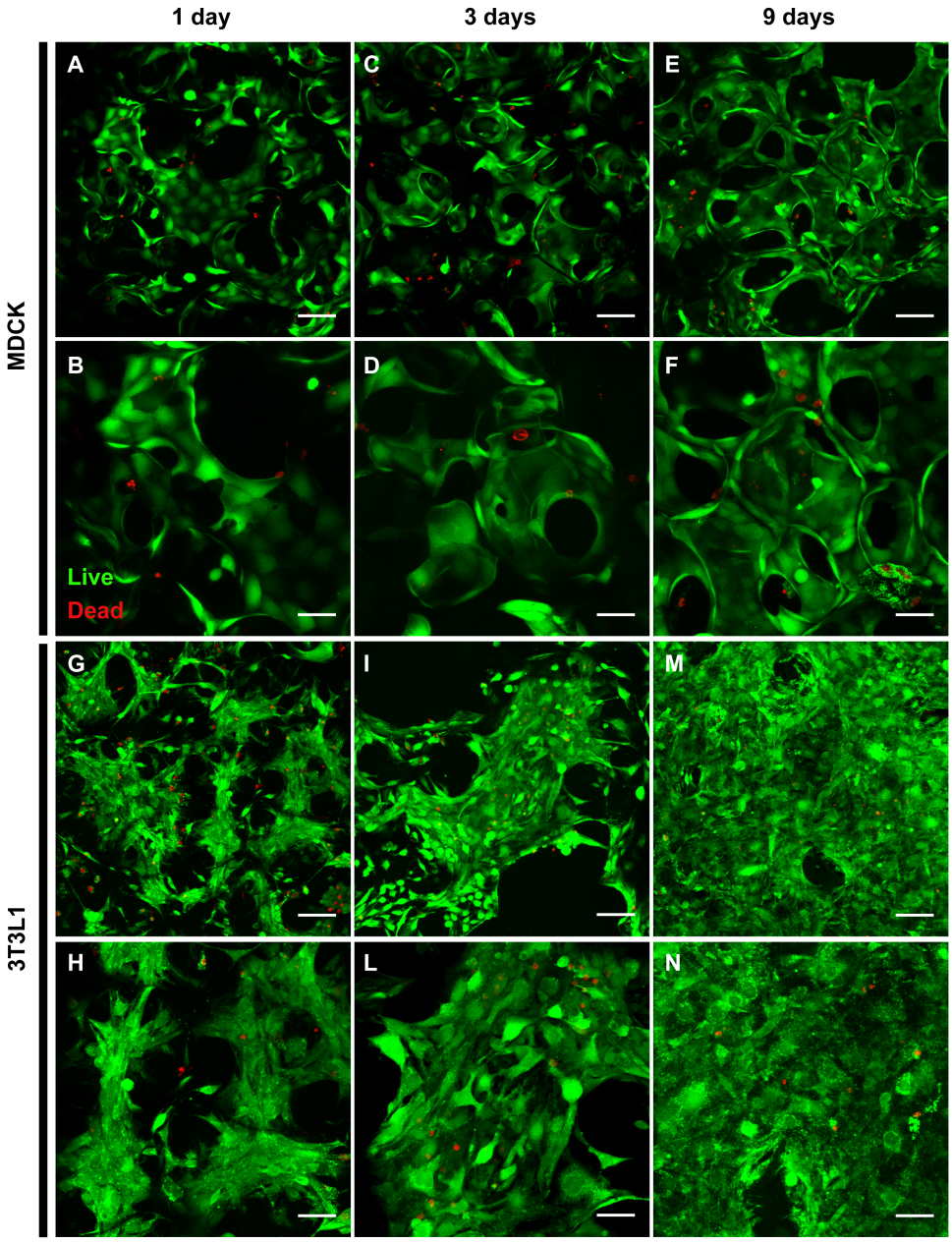

Figure 3-4 MDCK and 3T3L1 cells viability. Confocal microscope images, live/dead assay for MDCKs seeded on OPAAF after 1 (A and B), 3 (C and D) and 9 (E and F) days of culture. Live/dead assay for 3T3L1s seeded on OPAAF after 1 (G and H), 3 (I and L) and 9 (M and N) days of culture (scale bars, 100 μm for images A, C, E, G, I and M; scale bars 50 μm for images B, D, F, H, L and N).

OPAAF's ability to support adipogenesis was explored *in vitro* using 3T3L1 preadipose cell line. As first step to establish the adipogenic differentiation protocol, we analysed cells morphology and proliferation by Live/Dead assay. At day 1, 3T3L1 showed a fibroblast-like morphology on OPAAF (Figures 3-4 G and H) while, from day 3 to day 9 (Figures 3-4 I-N), 3T3L1 switched to more rounding shape typical of preadipocyte (38). At day 9, 3T3L1 had formed a cell monolayer on OPAAF surrounding also the wide part of the pores (Figures 3-4 M and N).

Current protocols for 3T3L1 adipogenic differentiation are based on a three phases approach (38, 39), in which a first proliferation phase is followed by an adipogenic induction phase, and, eventually, by a maintenance phase. Starting from the information obtained from the Live/Dead assay, we designed a differentiation protocol adapted to our 3D model (Figures 3-5). 3T3L1 adipogenic differentiation has been evaluated by BODIPY staining for fatty acid (FA) (Figures 3-5 A-F) and by qRT-PCR analysis for PPARγ (Figure 3-5 G) a master regulator of adipogenic differentiation (40). As we can observe from BODIPY staining, 3T3L1 are already positive for BODIPY staining after the proliferation phase (Figures 3-5 A and B) indicating an onset of fatty acid production in preadipose cells. During the induction phase, small and numerous lipid droplets could be seen in the cytoplasm of 3T3L1. Eventually, in the maintenance phase we observed an increase in lipid droplets size and the formation of unilocular droplet, typical of mature adipocyte. qRT-PCR analysis for PPARγ confirmed the adipogenic differentiation of 3T3L1, with a significant increase of PPARγ expression after the maintenance phase (Figure 3-5 G). Therefore, we can conclude that 3T3L1 are able to differentiate into mature adipocyte on OPAAF.

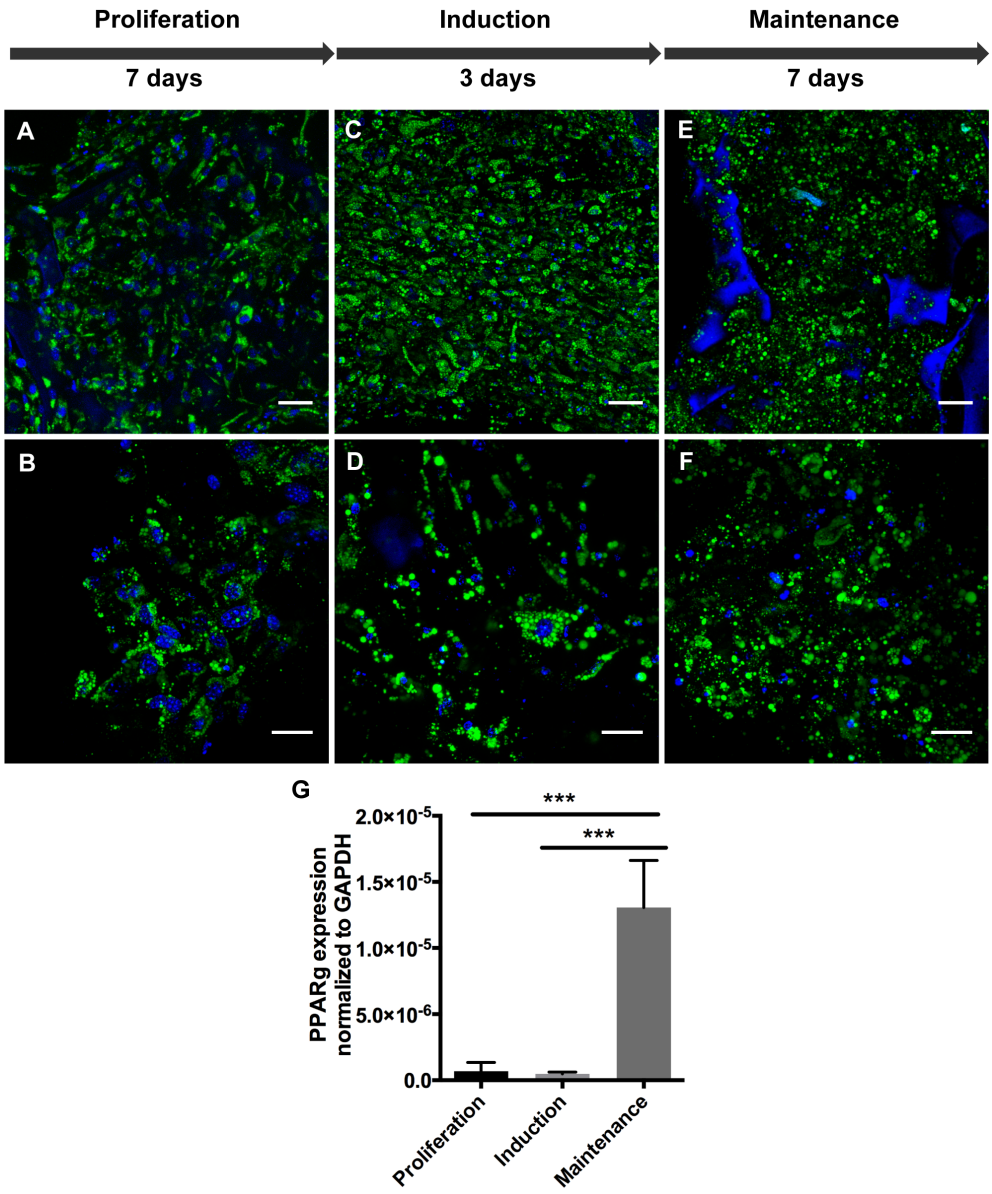

Figure 3-5 3T3L1 adipogenic differentiation. Confocal microscope images, BODIPY/DAPI staining for 3T3L1s during the adipogenic differentiation protocol. 3T3L1s after proliferation phase (A and B), adipogenic induction phase (C and D) and maintenance phase (E and F) (A, C and E, scale bar 50 μm; B, D and F, scale bar 30 μm). qRT-PCR analysis for PPARγ during the adipogenic differentiation (G).

In order to evaluate OPAAF's capability to support endothelial cells adhesion and proliferation, HUVEC cells have been seeded and monitored over time by Live/Dead assay. After 1 day of 3D culture, HUVEC showed high adhesion affinity toward OPAAF (Figures 3-6 A and B). Cells organize around pores edge at day 3 (Figures 3-6 C and D) and appeared homogeneously distributed on scaffold's surface at day 9 exhibiting a spindle-like morphology (Figures 3-6 E and F). Here we reported that OPAAFs supported HUVEC adhesion and spreading probably for the RGD-mimic structure of the OPAA polymer. As

reported in literature (41-43), HUVECs need the presence of adhesive peptide for the attachment and survival on 3D surfaces. The RGD-mimic together with the open pores structure seemed to trigger cells proliferation inducing also a change in HUVEC morphology toward a spindle-like shape.

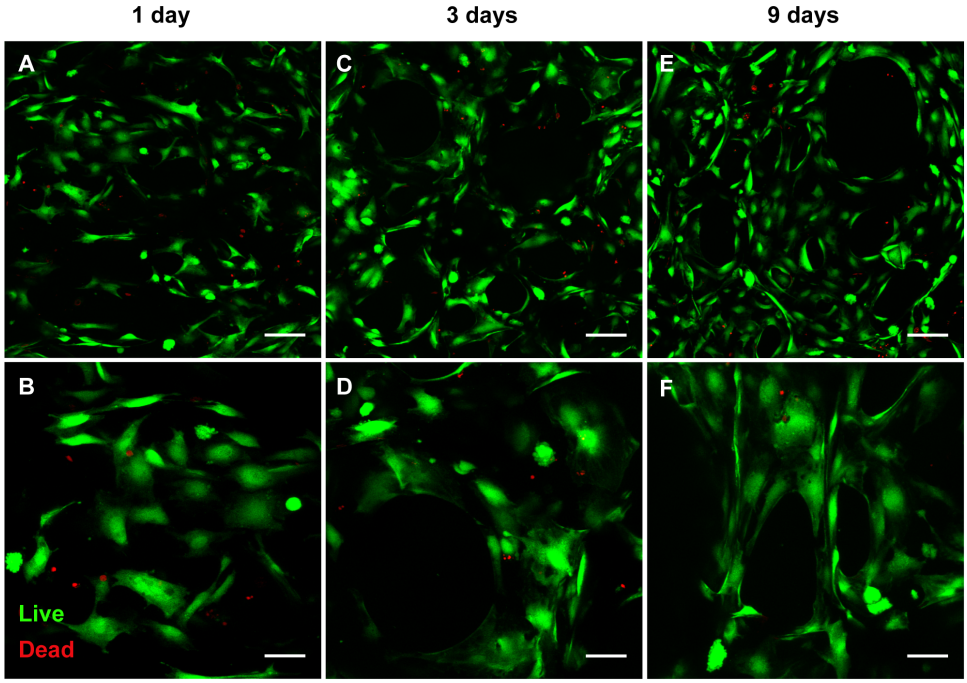

Figure 3-6 HUVEC cells viability. Confocal microscope images, live/dead assay for HUVECs seeded on OPAAF after 1 (A and B), 3 (C and D) and 9 (E and F) days of culture (scale bars, 100 μm for images A, C and E; scale bars 50 μm for images B, D and F).

3.3.5 In vivo biocompatibility, adipose and vascular tissue infiltration

The biocompatibility of OPAAF was assessed *in vivo* in a mouse model by subcutaneous implantation in the medial femoral region using an arteriovenous flow-through vessel loop for angiogenesis (44). At 14 and 50 days after implantation, scaffolds were paraffin-embedded and stained with HE, or immunostained for Iba1, CD31 and αSMA, in order to evaluate host tissue infiltration, immune reaction and vascularization, respectively (Figures 3-7 A-P and Figure 3-8). OPAAF appeared dark-red to brown in HE stained sections and was characterized by a homogenous structure where newly formed tissue was evident within the pores. Unstained small-sized vacuoles were occasionally observed. At 14 and 50 days after implantation, the scaffolds were well integrated in the murine subcutaneous tissue and their overall structure remained intact (Figures 3-7 A and B). Fibrous encapsulation and inflammation were overall mild,

localized at the periphery of the scaffold (Figures 3-7 C and E). Limited host reaction was observed along the surface in contact with underlying skeletal muscles, while surrounding adipose tissue appeared almost unaffected by the presence of the OPAAF. The inflammatory cell infiltrate was mainly composed of macrophages and multinucleated giant cells (Figures 3-7 G and L), which is consistent with a foreign body response. In the details, we observed significant reduction of the foreign body response after 50 days (Figures 3-7 I and L) of implantation, compared to the one at 14 days (Figures 3-7 G and H). Notably, OPAAF pores were infiltrated by well-vascularized connective tissue (Figure 3-7 M) at 14 days, substituted by adipose tissue (Figure 3-7 O) at 50 days, growing over the surface of the material and occupying the cavity of pores. The immunohistochemical analysis of endothelial cells (Figures 3-7 N and P), together with the immunofluorescence analysis for alpha smooth muscle actin (Figure 3-8), revealed the presence of organized vascular structures filled with erythrocytes, extending deep into the inner core of the scaffolds. The presented results suggest that OPAAF supported the infiltration of host's vessels favouring also cell viability and survival.

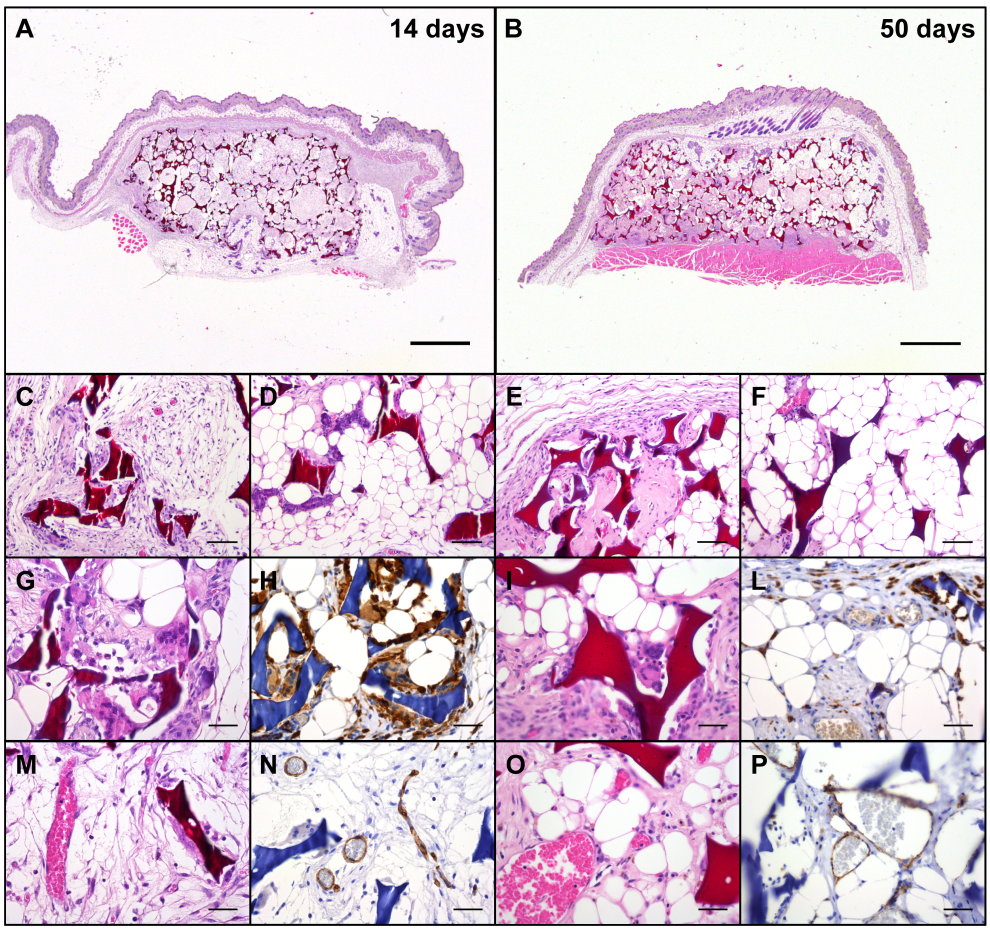

Figure 3-7 Histological examination of OPAAF at 14 and 50 days after implantation. H&E staining (A-B, C-F, G, I, M and O) and immunoperoxidase staining for anti-Iba1 (H and L), and CD31 (N and P). OPAAF integration (A and B) and encapsulation (C and E) in the implantation sites. Adipose tissue colonizing the pores of OPAAF (D and F). Inflammatory infiltrate mainly composed of macrophages and multinucleated giant cells (D, E, M and N). Central pores colonized by vascularized loose connective tissue at 14 days (M), and vascularized adipose tissue at 50 days (O). Vascularization of central pores (N and P). (Scale bars: A and B 1000 μm; C-F 100 μm; G-P 50 μm).

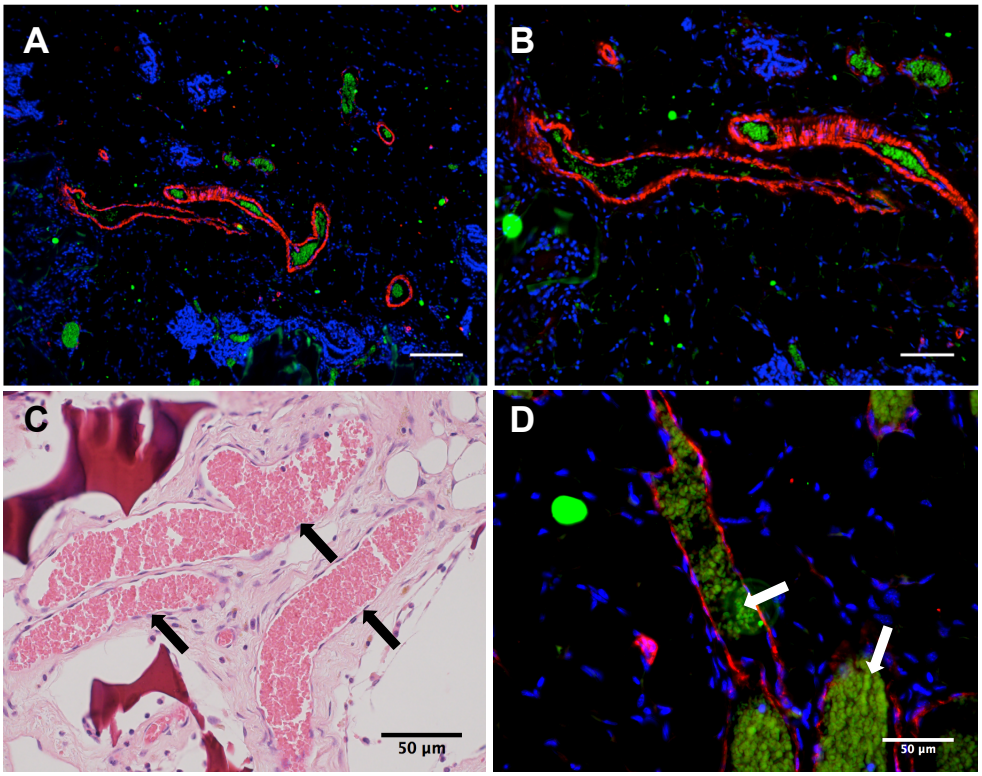

Figure 3-8 Host vessels infiltration at 50 days after implantation. Immunofluorescent images. αSMA (red) stained blood vessels walls; DAPI (blue) stained nuclei, Alexa 488 (green) stained erythrocytes (A and B, scale bars 100 and 50 µm respectively). Erythrocytes population is readily visible with the H&E staining (C) and immunofluorescence analysis for αSMA/erythrocytes/nuclei (D).

3.4 Discussion

In this work, we adopted a design driven approach to fabricate an RGD-mimetic macroporous foam (OPAAF) specific for adipose tissue reconstruction. OPAAF was designed to fulfil three main target criteria: i) induction of cell infiltration, adhesion and proliferation, ii) support of *in vivo* vascularization and iii) resemblance of the native adipose tissue mechanical properties.

To this aim, we selected the most promising formulation for cell adhesion properties from our library of RGD-mimetic PAA bulk hydrogels (26) and fabricated it into macroporous scaffold with improved cell infiltration dynamic and nutrient mass transport, if compared with the bulk counterpart. It is well known that scaffold geometry and pores architecture, have a large impact on cell seeding, proliferation and differentiation (45). Therefore, in order to obtain a uniform and interconnected porous structure, the well-established gas foaming technique (46) has been tuned to match the chemistry of OPAA oligomers. The reaction took place in water, resulting in short purification process. In particular,

the obtained scaffold is characterized by a double porous structure ideal to support cell growth, interaction and proliferation in the first phase, through the secondary mesopores (40-100 μm), and to allow fat tissue ingrowth in the second phase, through the primary macroporous structure (300-500 μm) which mimic native adipose tissue lobules dimension (32, 47).

The biocompatibility and capability of OPAAF to support cells infiltration, adhesion and proliferation have been evaluated with epithelial, fibroblast and endothelial cells. An important prerequisite for a scaffold in tissue engineering applications is to be compatible with cell culture procedure and to allow fast transfer of nutrients (29). In this contest, the swelling behaviour of OPAAF played a pivotal role in determining a homogeneous cell seeding, distribution and viability. OPAA based hydrogels have already shown to be hydrophilic with a relevant swelling behaviour (26, 27). Here, the 3D organization of OPAA oligomers in porous foam further enhanced the hydrophilic profile of the polymer, offering a suitable environment for cell culture. Indeed, MDCK, 3T3L1 and HUVEC homogeneously infiltrated, adhered and proliferated on OPAAF forming layers of viable cells. The reported results suggest that the combination of the RGD-mimetic moieties and the hydrophilic interconnected porous network could resemble the features of the ECM environment providing a powerful tool for tissue engineering studies.

In order to regenerate adipose tissue, an ideal construct should be able to mimic the native one both in function and in structure, which include the incorporation of fat tissue and blood vessels (6). Current strategies, in both reconstructive and cosmetic surgery, are centred on the use of autologous flap reconstruction or fat grafting, where the crucial point is the fat survival in terms of effective volume persistence (48). In the last decade, the above-mentioned strategies have been integrated with the use of cells from donor (49), natural biomaterials (10, 50) or growth factors (51, 52), besides, fat tissue resorption still remains an unpredictable risk. In this contest, scaffolds are required as support for either donor or host cells differentiation, for maintaining volume after implantation and assisting cell invasion and ingrowth of host tissue.

To this aim, we evaluated OPAAF capability to support *in vitro* adhesion and growth of the two main cell components of adipose tissue, adipose and endothelial cells. The reported results show that OPAAF efficiently supported adipogenic

differentiations of 3T3L1 preadipose cell line and endothelial cells adhesions and organization around the pores.

When implanted *in vivo,* a scaffold has to initially support cell infiltration and survival and then it is typically broken down as the new tissue is remodelled (53). Notably, OPAAF was characterized by a progressive hydrolytic degradation that is compatible with initial implantation requirements and could also play an important role in the long-term implantation, tissue formation and remodelling. In addition, we investigated OPAAF capability to support *in vivo* adipose and vascular tissue infiltration and organization, showing that the macroporous structure of OPAAF allowed host adipocytes infiltration forming lobules-like structure similar to the native adipose tissue organization.

The presence of a sustainable vascular network is fundamental for scaffold engraftment and maintenance. Interestingly, during the *in vivo* implantation of OPAAF, we observed extensive blood vessels infiltration, proving that a sustainable diffusion of nutrients and oxygen is possible even in the inner core of the scaffold. We also evaluated the host immune reaction to OPAAF, as the immunological response is important for a scaffold to be used in clinical application (54). In particular, we observed a mild inflammation and fibrous encapsulation in the first phase, considerably reduced in the time point at 50 days.

The lack of vascular supply and the donor site morbidity are among the first causes of tissue resorption and complications in the autologous transplantation approaches (55). The use of a cell-free scaffold able to allow host cells infiltration and new adipose and vascular tissue formation may be, therefore, a valuable alternative to the current strategies offering possible solution to the abovementioned drawbacks.

In a physiological environment, the ECM and the surrounding tissue play a pivotal role both in cell support and biomechanical stimulation (56, 57). Therefore, in designing a scaffold for adipose tissue engineering, it is fundamental to resemble the native tissue structure and mechanical properties, firstly, to provide important cue for cell commitment toward a specific lineage (4), and secondly, to support mechanically, adipose and vascular tissue ingrowth in *in vivo* studies. To date, both synthetic and natural scaffolds have been designed and tested mechanically in order to reproduce stiffness values close to that of adipose tissue (44, 58-60). However, an extensive characterization of scaffold response to

large deformation and dynamic stimuli, which a soft tissue, such as breast, frequently undergoes, is still missing. For this reason, we modulated the fabrication's process of OPAAF in order to achieve a scaffold with mechanical properties close to the one of adipose tissue in term of stiffness, able to resist to high level of strain and to response linearly to dynamic stimulation. The use of the gas foaming technique allowed us to reduce the Young's modulus of previously characterized OPAA hydrogels (26, 27), obtaining a scaffold with mechanical properties in the range of the native tissue (31, 32). In addition, we designed a protocol for the mechanical stimulation of OPAAF in order to evaluate its properties both in static and dynamic conditions. The compression test assessed the capability of OPAAF to support high level of deformations without any relaxation reaction thanks to the efficient crosslinking process. Furthermore, the dynamic analysis at different frequencies highlighted the linear response of OPAAF to cyclic and progressive stimuli.

From the clinical point of view, a strategy able to offer adipose tissue reconstruction together with a stable mechanical support for the new tissue is still missing. Indeed, the autologous fat transplantation strategies are affected by a consistent variability for volume retention, while synthetic prosthesis implantation can be impaired by rupture and contraction (61). In this context, the resistance to strain and the elastic behaviour of OPAAF may overcome the issues related to the mechanical support.

3.5 Conclusion

Our study showed that OPAAF is able to support *in vitro* the growth of several cell types together with the adipogenic differentiation of preadipose cells, and *in vivo* the infiltration of fat and vascular tissue. The increasing clinical demand for innovative therapeutic approaches able to compensate volume and function of damaged tissues, in case of trauma or tumour resection, represents an important challenging field where scaffolds morphology, biomechanics and cell-substrate interaction drastically influence the phenotype, signal transduction and cell differentiation. In this context, OPAAF with its biological and mechanical properties can provide a possible safe tool for breast tissue reconstruction.

3.6 REFERENCES

1. Patrick CW. Adipose tissue engineering: the future of breast and soft tissue reconstruction following tumor resection. Seminars in surgical oncology.19(3):302-11.
2. Patrick CW. Tissue engineering strategies for adipose tissue repair. The Anatomical record. 2001;263(4):361-6.
3. Patrick CW. Breast tissue engineering. Annual review of biomedical engineering. 2004;6:109-30.
4. Gardel M, Schwarz U. Cell-substrate interactions. Journal of physics Condensed matter : an Institute of Physics journal. 2010;22(19):190301-.
5. Lin C-Y, Li L-T, Su W-T. Study of subcellular dynamics on cell-substrate interactions by live cell imaging. Journal of biomedical materials research Part A. 2014;102(4):1149-54.
6. Choi JH, Gimble JM, Lee K, Marra KG, Rubin JP, Yoo JJ, et al. Adipose tissue engineering for soft tissue regeneration. Tissue engineering Part B, Reviews. 2010;16(4):413-26.
7. Wittmann K, Dietl S, Ludwig N, Berberich O, Hoefner C, Storck K, et al. Engineering vascularized adipose tissue using the stromal-vascular fraction and fibrin hydrogels. Tissue engineering Part A. 2015;21(7-8):1343-53.
8. Young DA, Choi YS, Engler AJ, Christman KL. Stimulation of adipogenesis of adult adipose-derived stem cells using substrates that mimic the stiffness of adipose tissue. Biomaterials. 2013;34(34):8581-8.
9. Gentleman E, Nauman Ea Fau - Livesay GA, Livesay Ga Fau - Dee KC, Dee KC. Collagen composite biomaterials resist contraction while allowing development of adipocytic soft tissue in vitro. (1076-3279 (Print)).
10. Cho SW, Kim SS, Rhie JW, Cho HM, Choi CY, Kim BS. Engineering of volume-stable adipose tissues. Biomaterials. 2005;26(17):3577-85.
11. Kang JH, Gimble Jm Fau - Kaplan DL, Kaplan DL. In vitro 3D model for human vascularized adipose tissue. (1937-335X (Electronic)).
12. Flynn LE. The use of decellularized adipose tissue to provide an inductive microenvironment for the adipogenic differentiation of human adipose-derived stem cells. Biomaterials. 2010;31(17):4715-24.
13. Mano JF, Silva GA, Azevedo HS, Malafaya PB, Sousa RA, Silva SS, et al. Natural origin biodegradable systems in tissue engineering and regenerative

medicine: present status and some moving trends. Journal of the Royal Society, Interface / the Royal Society. 2007;4(17):999-1030.

14. Moroni L, de Wijn Jr Fau - van Blitterswijk CA, van Blitterswijk CA. Integrating novel technologies to fabricate smart scaffolds. (0920-5063 (Print)).

15. Fischbach C, Spruss T, Weiser B, Neubauer M, Becker C, Hacker M, et al. Generation of mature fat pads in vitro and in vivo utilizing 3-D long-term culture of 3T3-L1 preadipocytes. Experimental cell research. 2004;300(1):54-64.

16. Neubauer M, Hacker M Fau - Bauer-Kreisel P, Bauer-Kreisel P Fau - Weiser B, Weiser B Fau - Fischbach C, Fischbach C Fau - Schulz MB, Schulz Mb Fau - Goepferich A, et al. Adipose tissue engineering based on mesenchymal stem cells and basic fibroblast growth factor in vitro. (1076-3279 (Print)).

17. Alhadlaq A, Tang M Fau - Mao JJ, Mao JJ. Engineered adipose tissue from human mesenchymal stem cells maintains predefined shape and dimension: implications in soft tissue augmentation and reconstruction. (1076-3279 (Print)).

18. Angelova N, Hunkeler D. Rationalizing the design of polymeric biomaterials. Trends in biotechnology. 1999;17(10):409-21.

19. Hu Y, Winn SR, Krajbich I, Hollinger JO. Porous polymer scaffolds surface-modified with arginine-glycine-aspartic acid enhance bone cell attachment and differentiation in vitro. Journal of biomedical materials research Part A. 2003;64(3):583-90.

20. Kim TG, Park TG. Biomimicking extracellular matrix: cell adhesive RGD peptide modified electrospun poly(D,L-lactic-co-glycolic acid) nanofiber mesh. Tissue engineering. 2006;12(2):221-33.

21. Blit PH, Shen YH, Ernsting MJ, Woodhouse KA, Santerre JP. Bioactivation of porous polyurethane scaffolds using fluorinated RGD surface modifiers. Journal of biomedical materials research Part A. 2010;94(4):1226-35.

22. Guarnieri D, De Capua A, Ventre M, Borzacchiello A, Pedone C, Marasco D, et al. Covalently immobilized RGD gradient on PEG hydrogel scaffold influences cell migration parameters. Acta biomaterialia. 2010;6(7):2532-9.

23. Tanahashi K, Mikos AG. Protein adsorption and smooth muscle cell adhesion on biodegradable agmatine-modified poly(propylene fumarate-co-ethylene glycol) hydrogels. Journal of biomedical materials research Part A. 2003;67(2):448-57.

24. Ferruti P BS, and Ranucci E. Novel Agmatine-Containing Poly(amidoamine) Hydrogels as Scaffolds for Tissue Engineering. Biomacromolecules 2005, 6, 2229-2235.

25. Franchini J, Ranucci E, Ferruti P, Rossi M, Cavalli R. Synthesis, physicochemical properties, and preliminary biological characterizations of a novel amphoteric agmatine-based poly(amidoamine) with RGD-like repeating units. Biomacromolecules. 2006;7(4):1215-22.

26. Martello F, Tocchio A, Tamplenizza M, Gerges I, Pistis V, Recenti R, et al. Poly(amido-amine)-based hydrogels with tailored mechanical properties and degradation rates for tissue engineering. Acta Biomater. 2014;10(3):1206-15.

27. Tocchio A, Martello F, Tamplenizza M, Rossi E, Gerges I, Milani P, et al. RGD-mimetic poly(amidoamine) hydrogel for the fabrication of complex cell-laden micro constructs. Acta Biomater. 2015.

28. Hollister SJ. Porous scaffold design for tissue engineering. Nature materials. 2005;4(7):518-24.

29. Drury JL, Mooney DJ. Hydrogels for tissue engineering: scaffold design variables and applications. Biomaterials. 2003;24(24):4337-51.

30. O'Brien FJ, Harley BA, Yannas IV, Gibson LJ. The effect of pore size on cell adhesion in collagen-GAG scaffolds. Biomaterials. 2005;26(4):433-41.

31. Samani A, Bishop J Fau - Luginbuhl C, Luginbuhl C Fau - Plewes DB, Plewes DB. Measuring the elastic modulus of ex vivo small tissue samples. (0031-9155 (Print)).

32. Comley K, Fleck NA. A micromechanical model for the Young's modulus of adipose tissue. International Journal of Solids and Structures. 2010;47(21):2982-90.

33. Ferruti PR, E.; Trotta, F.; Gianasi, E.; Evagorou, E. G.; Wasil, M.; Wilsona, G.; Duncan, R. Synthesis, characterisation and antitumour activity of platinum(II) complexes of novel functionalised poly(amido amine)s. Macromol Chem Phys 1999;200, 1644–1654.

34. Buckley CT, Thorpe SD, O'Brien FJ, Robinson AJ, Kelly DJ. The effect of concentration, thermal history and cell seeding density on the initial mechanical properties of agarose hydrogels. Journal of the mechanical behavior of biomedical materials. 2009;2(5):512-21.

35. Anseth KSB, C.N.; Brannon-Peppas, L. Mechanical properties of hydrogel and their experimental determination . Biomaterials. 1995;Vol. 17 No. 17.

36. Geerligs M, Peters GW, Ackermans PA, Oomens CW, Baaijens FP. Linear viscoelastic behavior of subcutaneous adipose tissue. Biorheology. 2008;45(6):677-88.

37. Patel PN, Smith CK, Patrick CW, Jr. Rheological and recovery properties of poly(ethylene glycol) diacrylate hydrogels and human adipose tissue. J Biomed Mater Res A. 2005;73(3):313-9.

38. Zebisch K, Voigt V, Wabitsch M, Brandsch M. Protocol for effective differentiation of 3T3-L1 cells to adipocytes. Analytical biochemistry. 2012;425(1):88-90.

39. Pittenger MF, Mackay Am Fau - Beck SC, Beck Sc Fau - Jaiswal RK, Jaiswal Rk Fau - Douglas R, Douglas R Fau - Mosca JD, Mosca Jd Fau - Moorman MA, et al. Multilineage potential of adult human mesenchymal stem cells. (0036-8075 (Print)).

40. Rosen ED, MacDougald OA. Adipocyte differentiation from the inside out. (1471-0072 (Print)).

41. Choi WS, Bae JW, Lim HR, Joung YK, Park J-C, Kwon IK, et al. RGD peptide-immobilized electrospun matrix of polyurethane for enhanced endothelial cell affinity. Biomedical materials (Bristol, England). 2008;3(4):044104-.

42. Lee YB, Shin YM, Lee J-H, Jun I, Kang JK, Park J-C, et al. Polydopamine-mediated immobilization of multiple bioactive molecules for the development of functional vascular graft materials. Biomaterials. 2012;33(33):8343-52.

43. Yu J, Gu Y, Du KT, Mihardja S, Sievers RE, Lee RJ. The effect of injected RGD modified alginate on angiogenesis and left ventricular function in a chronic rat infarct model. Biomaterials. 2009;30(5):751-6.

44. Wiggenhauser PS, Muller Df Fau - Melchels FPW, Melchels Fp Fau - Egana JT, Egana Jt Fau - Storck K, Storck K Fau - Mayer H, Mayer H Fau - Leuthner P, et al. Engineering of vascularized adipose constructs. (1432-0878 (Electronic)).

45. Loh QL, Choong C. Three-dimensional scaffolds for tissue engineering applications: role of porosity and pore size. Tissue Eng Part B Rev. 2013;19(6):485-502.

46. Dehghani F, Annabi N. Engineering porous scaffolds using gas-based techniques. (1879-0429 (Electronic)).

47. Abrahamson DR. Recent studies on the structure and pathology of basement membranes. (0022-3417 (Print)).

48. Ross RJ, Shayan R Fau - Mutimer KL, Mutimer Kl Fau - Ashton MW, Ashton MW. Autologous fat grafting: current state of the art and critical review. (1536-3708 (Electronic)).

49. Matsumoto D, Sato K Fau - Gonda K, Gonda K Fau - Takaki Y, Takaki Y Fau - Shigeura T, Shigeura T Fau - Sato T, Sato T Fau - Aiba-Kojima E, et al. Cell-assisted lipotransfer: supportive use of human adipose-derived cells for soft tissue augmentation with lipoinjection. (1076-3279 (Print)).

50. Piasecki JH, Moreno K Fau - Gutowski KA, Gutowski KA. Beyond the cells: scaffold matrix character affects the in vivo performance of purified adipocyte fat grafts. (1527-330X (Electronic)).

51. Topcu A, Aydin Oe Fau - Unlu M, Unlu M Fau - Barutcu A, Barutcu A Fau - Atabey A, Atabey A. Increasing the viability of fat grafts by vascular endothelial growth factor. (1538-3660 (Electronic)).

52. Khouri RK, Eisenmann-Klein M Fau - Cardoso E, Cardoso E Fau - Cooley BC, Cooley Bc Fau - Kacher D, Kacher D Fau - Gombos E, Gombos E Fau - Baker TJ, et al. Brava and autologous fat transfer is a safe and effective breast augmentation alternative: results of a 6-year, 81-patient, prospective multicenter study. (1529-4242 (Electronic)).

53. Lavik E, Langer R. Tissue engineering: current state and perspectives. (0175-7598 (Print)).

54. Anderson JM, Rodriguez A Fau - Chang DT, Chang DT. Foreign body reaction to biomaterials. (1044-5323 (Print)).

55. Wu LC, Bajaj A Fau - Chang DW, Chang Dw Fau - Chevray PM, Chevray PM. Comparison of donor-site morbidity of SIEA, DIEP, and muscle-sparing TRAM flaps for breast reconstruction. (1529-4242 (Electronic)).

56. Swinehart IT, Badylak SF. Extracellular matrix bioscaffolds in tissue remodeling and morphogenesis. (1097-0177 (Electronic)).

57. Engler AJ, Sen S, Sweeney HL, Discher DE. Matrix elasticity directs stem cell lineage specification. Cell. 2006;126(4):677-89.

58. Yu C, Bianco J, Brown C, Fuetterer L, Watkins JF, Samani A, et al. Porous decellularized adipose tissue foams for soft tissue regeneration. Biomaterials. 2013;34(13):3290-302.

59. Cheung HK, Han TT, Marecak DM, Watkins JF, Amsden BG, Flynn LE. Composite hydrogel scaffolds incorporating decellularized adipose tissue for soft tissue engineering with adipose-derived stem cells. Biomaterials. 2014;35(6):1914-23.

60. Bellas E, Lo Tj Fau - Fournier EP, Fournier Ep Fau - Brown JE, Brown Je Fau - Abbott RD, Abbott Rd Fau - Gil ES, Gil Es Fau - Marra KG, et al. Injectable silk foams for soft tissue regeneration. (2192-2659 (Electronic)).

61. Handel N, Garcia Me Fau - Wixtrom R, Wixtrom R. Breast implant rupture: causes, incidence, clinical impact, and management. (1529-4242 (Electronic)).

CHAPTER 4

4 DECORATION OF RGD-MIMETIC POROUS SCAFFOLD WITH ENGINEERED DEVITALIZED ADIPOSE MATRIX

Eleonora Rossi [a,b] et al.

a) SEMM, European School of Molecular Medicine, Campus IFOM-IEO, Via Adamello 16, 20139 Milano, Italy. b) Department of Biomedicine, University Hospital of Basel, Hebelstrasse 20, 4031 Basel, Switzerland.

4.1 INTRODUCTION

Breast cancer is the most common form of female cancers worldwide and patients affected by this pathology usually undergo mastectomy as part of the surgical treatment for cancer resection (1). Breast reconstruction following this procedure is currently an optional treatment, which helps women to recover from the physical and psychological point of view (1, 2). Current approaches for breast reconstruction, such as the use of silicon prosthesis and the autologous flap implantation, are still impaired by drawbacks such as incompatibility with radiotherapy and significant donor site morbidity (2, 3). Another promising technique, emerging in the last years, is the fat grafting that consists in the transfer of patients fat tissue from liposuction in the site of the defect (4). This technique is relying on the adipogenic and adipoinductive potential of human adipose stromal cells (hASCs) that are an abundant and promising cell type present in fat tissue (5). Unfortunately, there are still some concerns for the use of fat grafting after mastectomy such as the potential associated risk of hASCs with tumour seed activation, neoplastic formation and the volume loss over time that occurs because of the lack of vascular supply (4, 6, 7).

Adipose tissue engineering is trying to address this issue by exploiting alternative strategies to the abovementioned techniques. In the past years, different biomaterials, from synthetic and natural origins, have been tested and combined with several cell sources in adipose tissue engineering (8-13) but a strategy able to efficiently reconstruct fat tissue is still missing.

Biological scaffolds composed of extracellular matrix (ECM) are commonly used

for a variety of reconstructive surgical applications and are increasingly used in regenerative medicine strategies for tissue and organ replacement (14, 15). The ECM represents the secreted products of resident cells of each tissue and organ and has been shown to provide cues that affect cell migration, proliferation, and differentiation in a tissue specific manner (15-17). Recent studies demonstrated that scaffolds obtained out of decellularized adipose matrix could provide an adipoinductive substrate for hASCs differentiation in absence of differentiation factors (9, 11, 18, 19). Although the ECM is by definition the nature's ideal biological scaffold material, its fast degradation rate and poor mechanical properties make its clinical application difficult (10, 20).

Synthetic scaffolds, on the other hand, can overcome these problems offering a tunable range of degradation and mechanical properties (21-23). We recently developed a promising synthetic porous scaffold designed, from the biological and mechanical point of view, to be suitable for adipose tissue engineering applications (24). OPAAF is an RGD-mimetic macroporous foam with an interconnected porous network and mechanical properties resembling the native adipose tissue. In the previous chapter, we demonstrated that OPAAF is able to support and induce adipogenic differentiation of preadipocyte cell line *in vitro* together with adipose tissue infiltration *in vivo* (24).

Our aim was to combine the positive features of a structural synthetic polymer and of an engineered, devitalized ECM to obtain an adipoinductive hybrid construct for adipose tissue regeneration. We decorated the OPAAF with adipose ECM deposited by human hASCs *in vitro*. We subsequently devitalized the constructs and investigated the adipoinductive potential of the hybrid ECM-OPAAF *in vitro* and *in vivo*. We also addressed whether the level of maturation of the matrix could regulate the adipoinductive potential of the hybrid. Our hypothesis is that the hybrid construct could be a promising *off-the-shelf* material for adipose tissue reconstruction providing the proper mechanical support and adipogenic stimuli both *in vitro* and *in vivo*.

4.2 Materials and Methods

4.2.1 OPAA Syntheses and OPAAF Fabrication

OPAAF was fabricated as reported in the Chapter 3.

4.2.2 CELL SOURCE AND EXPANSION

Samples of human adipose tissue were collected either as lipoaspirates or as dermolipectomies obtained during routine surgical procedures after informed consent from the patient and following protocol approval by the local ethical committee. The tissue was processed as reported in literature (25) in order to retrieve hASCs. hASCs were then plated for expansion (seeding density of $3*10^3$ cells/cm^2) and cultured in complete medium (CM) which consisted of a-Modified Eagle's Medium, 10% fetal bovine serum, 100 mM HEPES buffer solution, 1 mM sodium pyruvate, 100 U/ml penicillin, 100 mg/ml streptomycin and 292 mg/ml L-glutamine (GIBCO, Switzerland) supplemented with 5 ng/ml fibroblast growth factor-2 (FGF-2; R&D systems, USA). Cells were cultured at 37°C in 5% CO_2 95% air-humidified incubator, harvested using 0.05% trypsin, centrifuged and resuspended in basal medium. Medium was changed twice a week. Upon confluence, cells were enzymatically retrieved and counted for use in the following experiments.

4.2.3 GENERATION OF DECELLULARIZED HYBRID ECM-OPAAF

4.2.3.1 3D CELL CULTURE FOR ECM DECORATION

Using a previously developed perfusion bioreactor system (26) for cell seeding and culture of 3D scaffolds, hASCs were perfused overnight through OPAAF (8 mm diameter and 3 mm thickness) at a superficial velocity of 1000 mm/s. After 24 h (cell seeding phase), the superficial velocity was reduced to 100 mm/s for perfusion culture of hASCs. For the adipogenic differentiation, $4x10^6$ cells were cultured for two weeks in DMEM supplemented with 10 μg/ml insulin, 1 μM dexamethasone, 100 μM indomethacin, and 500 μM 3-isobutyl-1-methyl xanthine (IBMX) (adipogenic induction medium) and one week in Dulbecco's modified Eagle medium (DMEM supplemented with 10 μg/ml insulin (adipogenic mantainance medium). Culture medium was changed twice a week. This protocol was used for the OPAAF decoration with the adipose ECM.

For the decoration with the stromal ECM, $2x10^6$ cells were cultured for two weeks in CM supplemented with FGF-2 and 0,1 mM L-ascorbic acid-2-phosphate (AA, R&D systems, USA).

4.2.3.2 HYBRID ECM-OPAAF CONSTRUCTS DECELLULARIZATION

After ECM deposition, samples were devitalized to obtain hybrid ECM-OPAAF constructs according to previous protocols (27). Briefly, samples underwent three freeze and thaw (F/T) cycles in liquid nitrogen and 37°C water bath (10 min each), respectively. Samples were rinsed in sterile PBS after each thaw step as well as in double distilled water after the second thaw in order to hypotonically lyse remaining cells. To eliminate cellular debris, a perfusion-based washing step was added subsequent to the F/T: the constructs were placed into the bioreactor system and perfused at 100 mm/s in PBS for 30 min at room temperature (RT).

4.2.4 Evaluation of hASCs-OPAAF interaction in vitro

4.2.4.1 Live/Dead assay

Cellular viability was investigated by using a live/dead assay solution consisting of Calcein-AM (1 μM) and Propidium Iodide (0.1 mM) prepared in PBS. Briefly, samples were rinsed in PBS 1X, immersed in staining solution for 15 minutes and incubated at 37°C. Staining solution was removed, samples washed twice with PBS and immersed in PBS before imaging. Live imaging was performed using a confocal microscope (Zeiss LSM 710 Rocky).

4.2.4.2 Immunostaining for Actin-Vinculin-DAPI

After 7 days in culture, constructs were fixed with 4% paraformaldehyde over night at 4°C and rinsed with PBS. Cells were permeabilized with 0.1% Triton X-100, blocked with 2% BSA and then incubated over night with monoclonal anti-vinculin primary antibody (Invitrogen), for 40 minutes at RT with Alexa Fluor 488 goat anti-mouse IgG1(c1) secondary antibody (Invitrogen) and 0,11uM Alexa fluor 555 directly conjugated to phalloidin (Invitrogen), for filamentous actin staining. After washing in PBS, nuclei were stained with 9.4 mM of bis-Benzimide H 33258 (Hoechst).

4.2.4.3 BODIPY staining

After the adipogenic differentiation, constructs were analyzed by BODIPY staining for fatty acid. Constructs were washed with PBS, fixed with 4% paraformaldehyde for 30 minutes at RT, rinsed with PBS, incubated with BODIPY® (Life Technologies) 5 uM in PBS for 30 minutes and finally stained with DAPI (life technologies).

4.2.5 ECM CHARACTERIZATION

4.2.5.1 SCANNING ELECTRON MICROSCOPY

Hybrid constructs were fixed over night in 4% paraformaldehyde at 4°C and then dehydrated in graded ethanol changes (30, 50, 75, and 100% EtOH concentration) followed by critical point drying. Samples were then sputtered with gold (Baltec MED020, 25 mA by 2 10^{-2} mBar) before examination under a Philips XL 30 ESEM microscope.

4.2.5.2 IMMUNOFLUORESCENCE ANALYSIS FOR COLLAGEN IV, LAMININ AND FIBRONECTIN

Before and after F/T, constructs were fixed with 4% paraformaldehyde over night at 4°C, rinsed with PBS and blocked with 2% BSA. Constructs were incubated over night with monoclonal anti-Collagen IV, Laminin or Fibronectin primary antibody (Abcam) and for 40 minutes at RT with Alexa Fluor 488 goat anti-human secondary antibody (Invitrogen).

4.2.5.3 ELISA

Samples were frozen at -80°C, mechanically disrupted in liquid nitrogen and dissolved in radio-immunoprecipitation assay (RIPA) buffer (Sigma Aldrich). The total amount of proteins was assessed by BCA protein assay (Termofisher Scientific). Samples were then diluted and assessed for human collagen 1A1 (R&D), laminin, fibronectin (Abcam) and collagen IV (Luminex, R&D). Each assay was performed according to the manufacturers' instruction. Results were normalised by the total amount of protein. All values are presented as mean ± standard deviation. Differences between experimental groups were statistically assessed using T-tests parametric. $P < 0.05$ was considered to indicate statistically significant differences.

4.2.6 GENE EXPRESSION ANALYSIS

Total RNA isolation was performed using Quick-RNA Mini Prep (ZYMO RESEARCH, Germany) according to the manufacturer's protocol. RNA measurement at 260 nm was performed using a Nanodrop spectrophotometer (Thermo Scientific). Reverse transcription into cDNA and polymerization was performed using a SuperScript III Reverse Transcriptase Kit (Invitrogen) and a Veriti Thermal Cycler (Life Technologies).

Quantitative real-time reverse transcriptase–polymerase chain reaction (qRT–

PCR; Applied Biosystems 7500 Real-Time PCR System, Life Technologies) were carried out to quantify the expression of the following genes of interest: PPARg, CEBPA and FABP4. Expression levels of genes of interest were normalized to the housekeeping gene glyceraldehyde-3-phosphate dehydrogenase (GAPDH). All values are presented as mean ± standard deviation. Differences between experimental groups were statistically assessed using one-way ANOVA tests. $P < 0.05$ was considered to indicate statistically significant differences.

4.2.7 In vivo implantation

Samples were implanted in subcutaneous pouches of nude mice (CD-1 nu/nu, 1-month old; Charles River Laboratories, Wilmington, MA) and retrieved after 8 weeks. The ectopic implantation was performed in accordance with institutional guidelines. Eight weeks after implantation, mice were sacrificed, and the constructs were harvested and fixed over night in 4% formalin, paraffin embedded, and sectioned (8 μm thick sections). Sections were then stained by hematoxylin and eosin (H&E) and observed microscopically for adipose tissue infiltration.

4.3 Results

4.3.1 In vitro Evaluation of cell-polymer interaction

OPAAF previously demonstrated the ability to promote cell adhesion and viability of epithelial, fibroblast and vascular cells, together with the adipogenic differentiation of 3T3L1 cell line, thanks to its RGD-mimetic porous structure (22, 23). In this work, we evaluated the biological properties of OPAAF with human primary cells by using a perfusion bioreactor system (26, 27). In order to investigate cell-polymer interactions, hASCs were seeded and cultured in proliferation medium for 7 days and cell viability and morphology were visualized by confocal microscopy. Thanks to the seeding and culture in perfusion, viable cells homogeneously distributed on the OPAAF (Figure 4-1 B). Moreover, IF analysis for Vinculin/Actin/DAPI demonstrated that hASCs adhered on the scaffold keeping mesenchymal morphology (Figure 4-1 C). These results confirmed the OPAAF potential as scaffold for the establishment of an *in vitro* 3D model starting from hASCs.

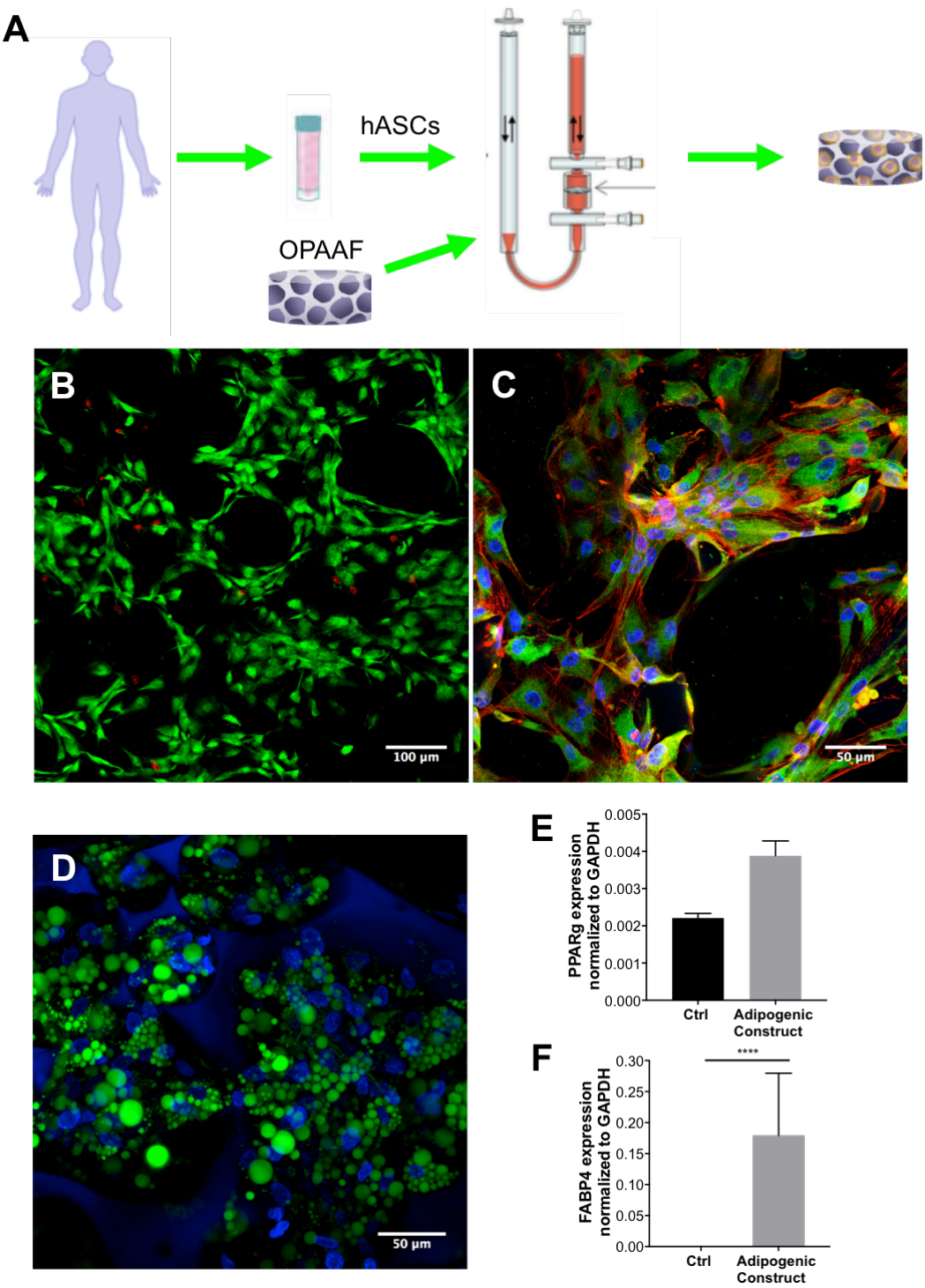

Figure 4-1 *In vitro* 3D model for adipose tissue generation. Schematic representation of the perfusion culture system (A). Live/dead staining (green and red, respectively) for cells viability 1 week after culture in proliferation medium (B). IF analysis for actin (red), vinculin (green) and DAPI (blue) 1 week after culture in proliferation medium (C). BODIPY/DAPI staining for FA after the adipogenic differentiation protocol (D). qRT-PCR analysis for PPARg and FABP4 after the differentiation protocol (E and F, respectively); undifferentiated hASCs serve as negative control.

4.3.2 IN VITRO ADIPOGENESIS

OPAAF ability to support adipose tissue formation was explored *in vitro* using an optimized protocol for adipogenic differention. Typically, protocols for adipogenic differentiation are based on a three-phase approach (28, 29) in which a first proliferation phase is followed by adipogenic induction, and, eventually, by the adipogenic maintenance. We seeded hASCs at higher density (see 4.2.3.1) and we directly stimulated cells with the adipogenic induction medium for two weeks. After a one-week maintenance phase, hASCs adipogenic differentiation was evaluated by BODIPY staining for fatty acid (FA) (Figure 4-1 D) and by qRT-PCR analysis for PPARg, an early marker of adipogenic differentiation, and FABP4, a late marker of differentiation (Figures 4-1 E and F, respectively) (30-32). hASCs efficiently differentiated into mature adipocytes with unilocular lipid droplets (Figure 4-1 D).

In the qRT-PCR analysis we compared the expression of PPARg and of FABP4 in undifferentiated hASCs and after the 3D differentiation protocol. Both PPARg and FABP4 were strongly expressed after the 3D differentiation, confirming the results of the FA staining. Overall these results demonstrated that OPAAF could support adipogenesis *in vitro* and generate mature adipose tissue-like constructs.

4.3.3 OPAAF DECORATION AND GENERATION OF DECELLULARIZED HYBRID ECM-OPAAF

OPAAF decoration was performed by hASCs mediated ECM deposition. Two different protocols were adopted for the decoration, in order to investigate the role of a differentiated or stromal matrix on adipogenic induction. The adipogenic differentiation protocol allowed for the decoration by specific matrix produced by mature adipocytes, while a proliferation protocol provided the decoration with a stromal matrix (Figure 4-2 A). In order to generate the hybrid ECM-OPAAF, a decellularization approach was employed to remove cells without affecting the deposited ECM. A previously established protocol for decellularization (27) was adopted in which: i) devitalization of the cellular component proceeded through a succession of freeze and thaw cycles with intermediate rinse in hypotonic solution and ii) the cellular debris were washed away by gentle perfusion of an isotonic solution through the construct with the bioreactor system (Figure 4-2 B). The hybrids ECM-OPAAF obtained were identified as Adipo-OPAAF and Stromal-

OPAAF according to the specific matrix deposited. We first analysed the structural integrity of deposited matrix, before and after F/T, by SEM analysis (Figure 4-3). The Stromal-OPAAF presented a much denser matrix as compared to the Adipo-OPAAF (Figures 4-3 E-F and A-B).

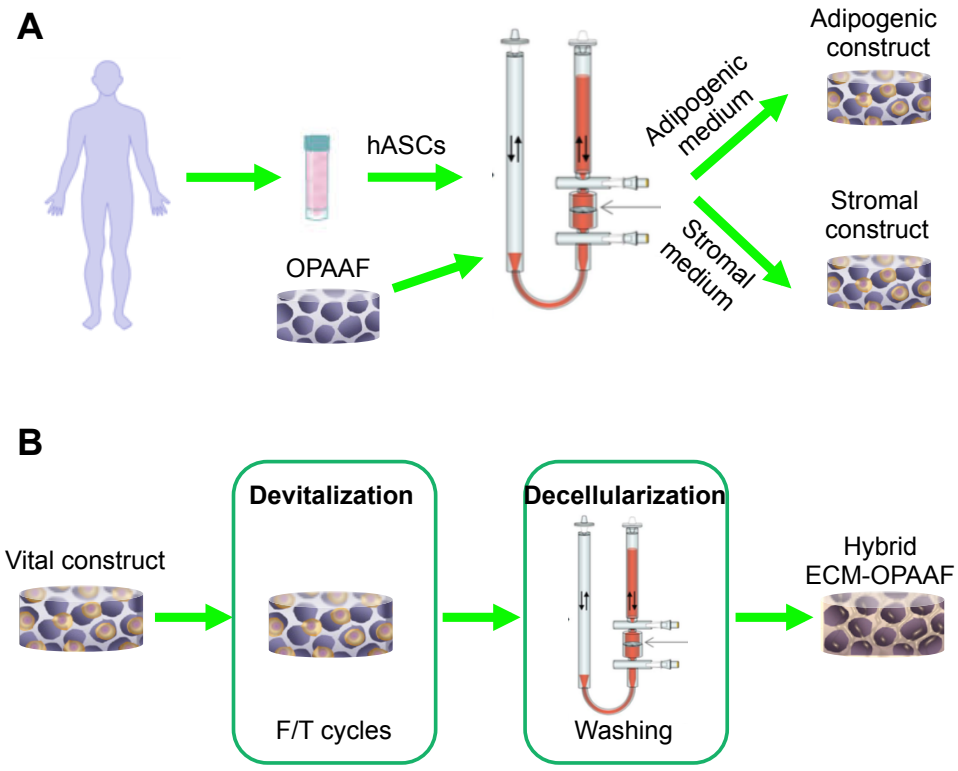

Figure 4-2 Schematic representation of the decoration protocols. ECM deposition by hASCs in adipogenic and stromal medium (A). Decellularization processes for the generation of the hybrid constructs (B).

Overall, the decellularization protocol minimally affected ECM integrity in both conditions tested. We also analysed, qualitatively, the matrix composition, by performing an IF analysis for Col IV, laminin and fibronectin. We found Col IV and laminin, two of the major component of the adipose tissue basal membrane (32, 33), in the Adipo-OPAAF (Figures 4-4 B and D), while only fibronectin was detected in the Stromal-OPAAF (Figure 4-4 F). Furthermore, we quantified the protein content and composition of hybrid constructs by ELISA (Figure 4-5). The BCA assay for the total amount of protein confirmed the result observed by SEM analysis, highlighting the higher density of the stromal matrix (data not shown). We found a higher expression of collagen IV in the Adipo-OPAAF (Figure 4-5 A). Fibronectin was significantly higher in the Stromal-OPAAF (Figure 4-5 B) while no differences were detected for collagen type I and laminin (Figure 4-5 C and D). Overall these results proved that the decellularization protocol could

preserve the structural and biological composition of the ECM. Furthermore, using different deposition protocols we obtained two types of hybrids ECM-OPAAF characterized by distinct protein compositions.

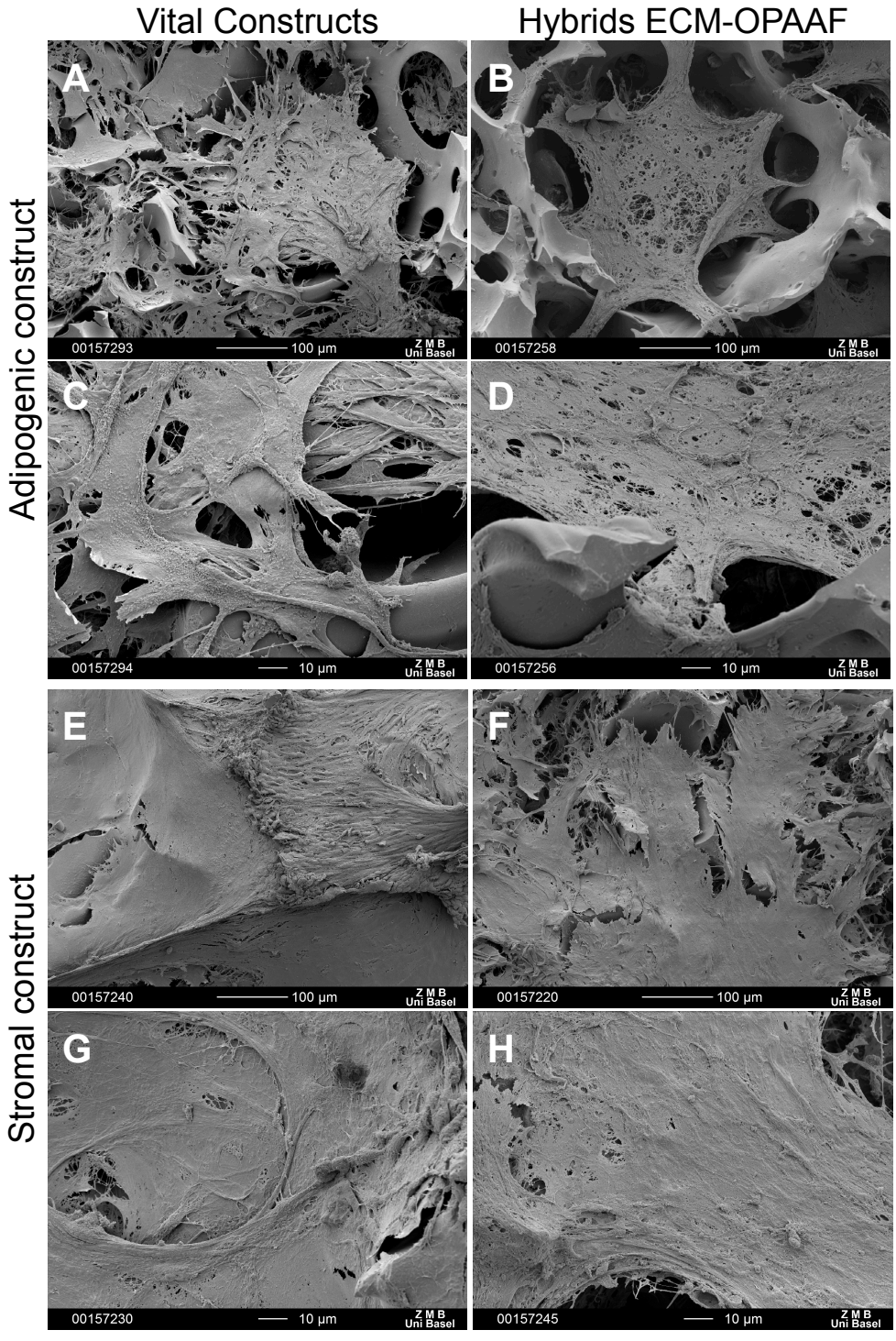

Figure 4-3 SEM analysis of the decorated constructs. Adipogenic construct before (A and C) and after devitalization (B and D). Stromal construct before (E and G) and after devitalization (F and H).

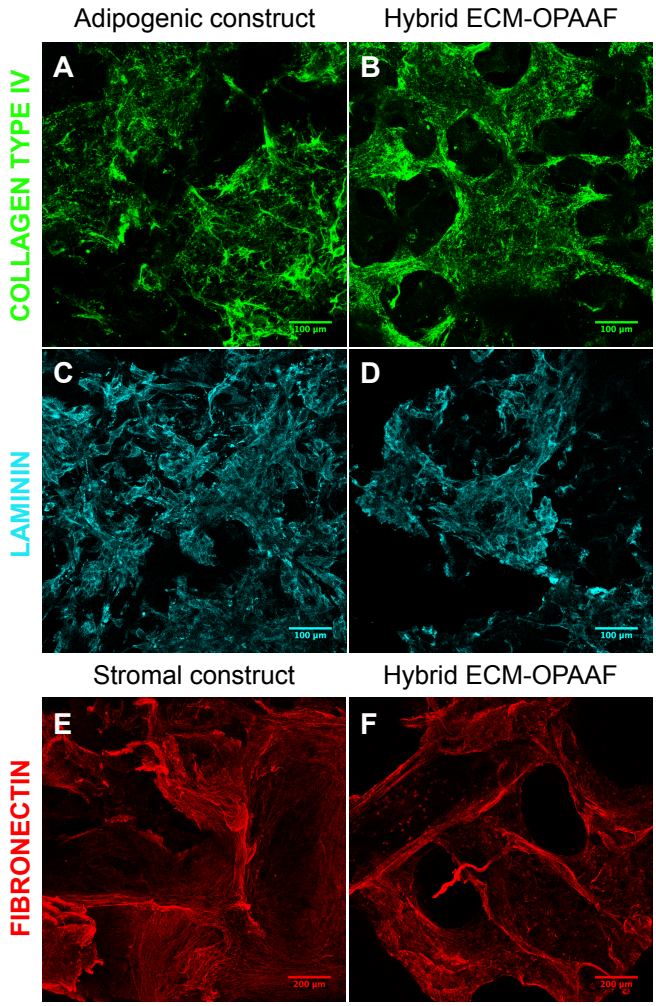

Figure 4-4 IF analysis for the ECM proteins. Adipogenic constructs IF analysis for collagen IV and laminin before (A and C, respectively) and after (B and D, respectively) decellularization. Stromal constructs IF analysis for fibronectin before (E) and after (F) decellularization.

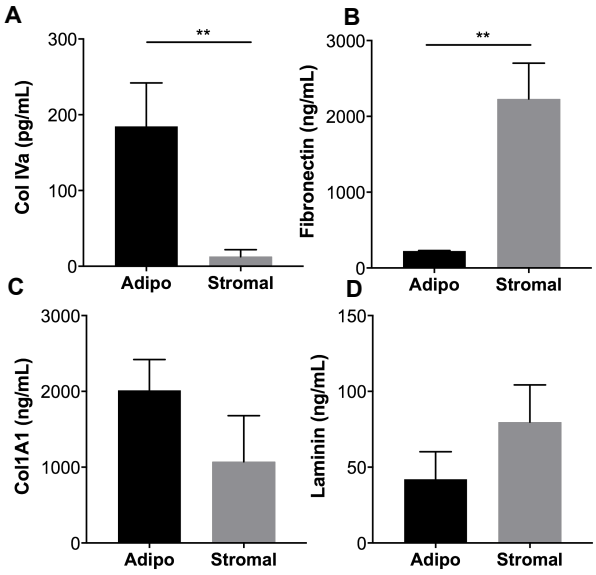

Figure 4-5 Quantitative analysis of ECM composition for Adipo-OPAAF and Stromal-OPAAF. Luminex analysis for collagen IV (A) and ELISA analysis for collagen 1A1,

fibronectin and laminin (B, C and D, respectively).

4.3.4 IN VITRO EVALUATION OF THE ADIPOINDUCTIVE POTENTIAL OF THE HYBRIDS ECM-OPAAF

In order to evaluate the adipoinductive potential of the hybrids ECM-OPAAF, we seeded hASCs on Adipo-OPAAF and Stromal-OPAAF, using the OPAAF as control condition. Cells were kept in culture in DMEM for two weeks, without any growth factor, to investigate the effect the scaffold decoration on cells commitment. We analysed cells behaviour qualitatively by BODIPY/DAPI/Actin staining, to investigate at the same time the adipogenic differentiation together with cell morphology. Cells were positive for BODIPY in all conditions tested. Cells showed a preadipocytic morphology, characterized by a round shape with small lipid droplets localized around the nuclei (Figures 4-6 B-G). A higher cell density was observed on the Stromal-OPAAF compared to the Adipo-OPAAF. Interestingly, cells underwent adipogenic commitment also on the nude OPAAF. We verified cells differentiation by qRT-PCR for early, mid and late gene in the adipogenic differentiation (PPARg, CEBPA and FABP4 respectively)(30-32), using hASCs cultured in 2D without any growth factor as negative control (Figures 4-6 H-L).

PPARg was basally expressed by hASCs in all the conditions tested with a significant increase in the decorated conditions (Figure 4-6 H). We observed differences in CEBPA expression between the 2D and the 3D conditions (Figure 4-6 I). Interestingly, cells cultured on the hybrids ECM-OPAAF showed a higher expression of FABP4, highlighting the adipoinductive effect of the ECM deposited. Therefore, we proved that the decoration strongly enhanced the adipoinductive potential of the OPAAF *in vitro*. Ultimately, our 3D model could be a promising tool for the investigation of the complex interplay between adipose ECM and adipogenic commitment.

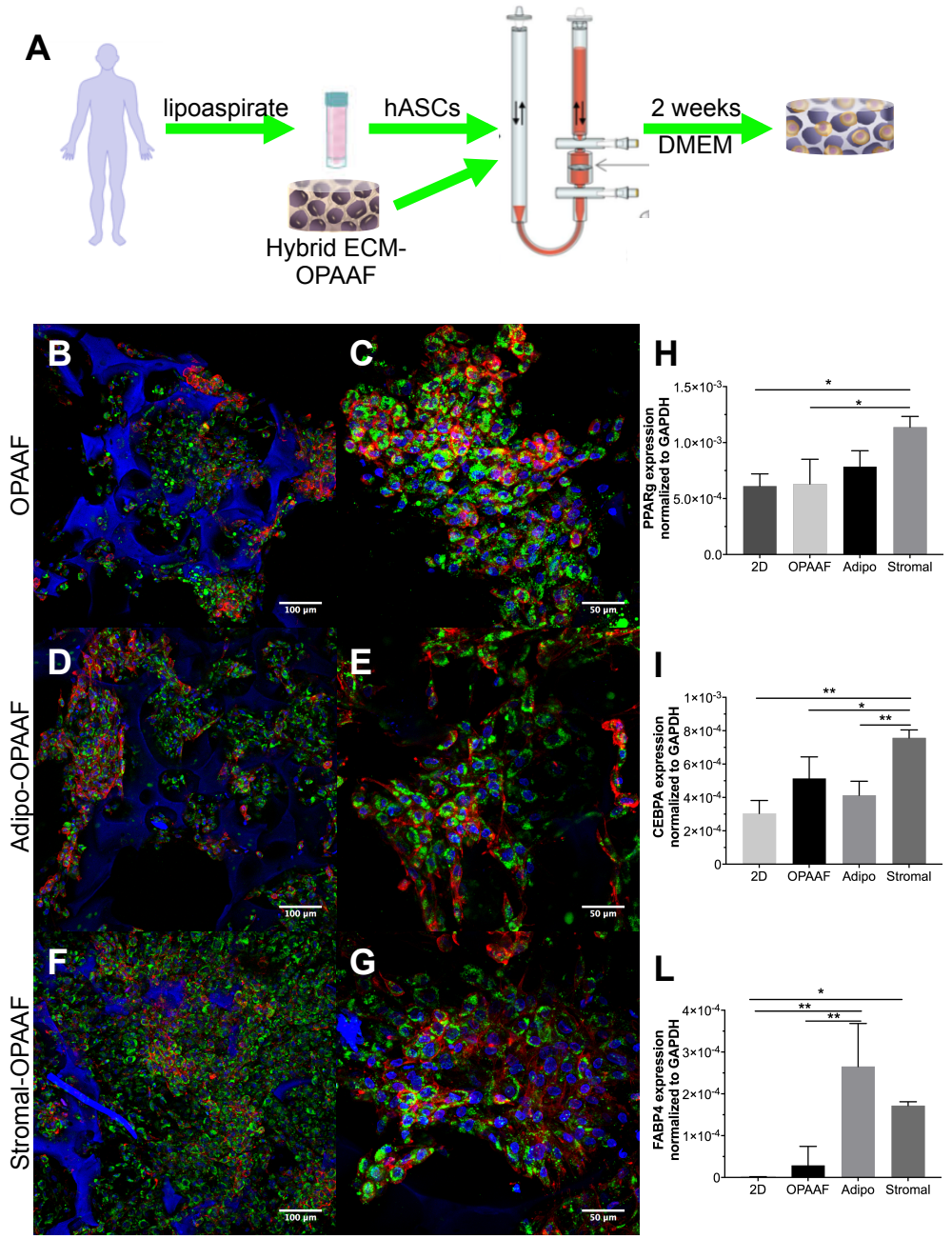

Figure 4-6 *In vitro* adipoinductive potential of hybrids ECM-OPAAF. Schematic representation of culture protocol (A). BODIPY/Actin/DAPI staining for OPAAF (B and C), Adipo-OPAAF (D and E) and Stromal-OPAAF (F and G). qRT-PCR analysis for PPARg (H), CEBPA (L) and FABP4 (I).

4.3.5 In vivo evaluation of the adipoinductive potential of the hybrid constructs

The adipoinductive potential of the hybrid constructs was tested *in vivo* by subcutaneous implantation in a nude mouse model. OPAAF was implanted as control. One month after implantation, the constructs were paraffin-embedded and stained for H&E to evaluate adipose tissue infiltration. Interestingly, decorated scaffolds were infiltrated by adipose tissue (Figures 4-7 D-L), while in the

OPAAF a poor infiltration of connective tissue was observed (Figures 4-7 A-C). No obvious differences were observed between the Adipo- and Stromal-OPAAF. These results proved that ECM decoration enhanced host tissue infiltration.

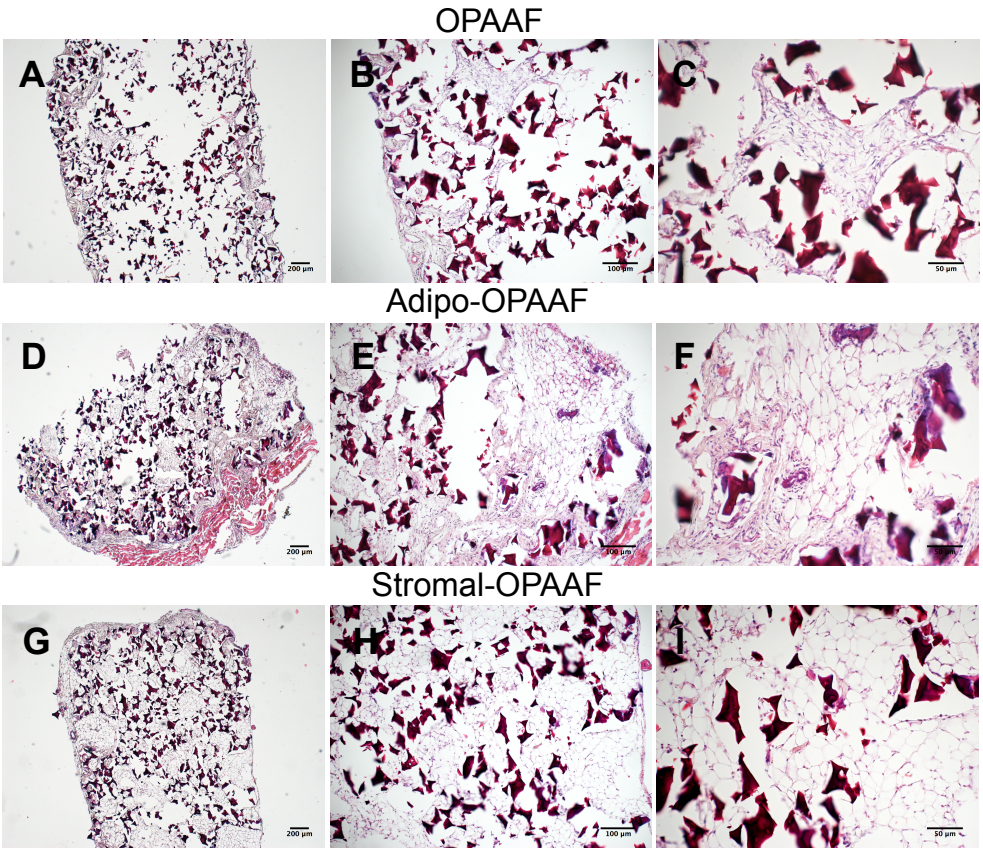

Figure 4-7 *In vivo* adipoinductive potential of hybrids ECM-OPAAF. H&E staining for OPAAF (A-C), Adipo-OPAAF (D-F) and Stromal-OPAAF (G-I) one month after implantation.

4.4 Discussion

In this work we combined the mechanical properties of the OPAAF and the biological cues of an engineered, decellularized ECM in order to obtain a hybrid construct for adipose tissue reconstruction.

We decorated our RGD-mimetic macroporous scaffold, OPAAF, with adipose ECM deposited by hASCs and we decellularized the resulting constructs by F/T. The hybrid ECM-OPAAF showed adipoinductive potential both *in vitro*, on hASCs in absence of any differentiation factor, and *in vivo*, after implantation in a nude mouse model.

Taken together, these results indicate that the hybrid ECM-OPAAF is a promising *off-the-shelf* material for adipose tissue reconstruction.

To date, several scaffolding biomaterials have been used to investigate the regeneration of adipose tissue but none was specifically designed for this purpose. In our previous work we biologically and mechanically designed the OPAAF scaffold to be suitable for adipose tissue engineering application. Here we combined our material with a human cell source for the establishment of an *in vitro* 3D model in a perfusion bioreactor system. This system already proved to be effective for long-term cell culture, providing a homogeneous cell seeding and supporting cells viability (27, 34). We reported for the first time a 3D *in vitro* model for the adipogenic differentiation in perfusion and we proved the efficacy of the system for the generation of adipose tissue-like constructs.

ECM is recognized as an ideal scaffold for tissue reconstruction, incorporating biochemical stimuli for cells adhesion, proliferation and differentiation in a tissue specific manner (14, 15). Unfortunately, ECM mechanical and degradation properties are not always suitable for tissue reconstruction (10, 20). A widely used approach, in the biomaterials field, is the modification of synthetic polymer with ECM protein, such as fibronectin, collagen or laminin, by coating or crosslinking (35). Although these techniques can enhance the biological performance of synthetic biomaterials, the biochemical stimulation induced by a single protein can poorly resemble the complex ECM environment (14, 21). An alternative strategy to present a more realistic environment to cells is the decoration approach, which is based on the innate cells capacity of producing ECM. This approach has been already investigated in our group, in the context of bone regeneration and in this work we successfully applied it also for adipose tissue engineering (27). Our approach demonstrated to be effective for matrix deposition and decellularization, preserving the structural and biological composition of the deposited ECM while providing a structural support to cells.

Decellularized ECMs are complex systems in which it is difficult to define the players involved in cells stimulation (14, 36). Since the function of the ECM tightly depends on its molecular assembly, it is important to know which are the main components of adipose ECM. Studies indicate that fibronectin and collagens are the most abundant proteins of interstitial fibers, while collagen IV and laminin are mainly present in the pericellular basement membranes of AT (32, 37). We analysed the deposited ECM and we confirmed the presence of the main structural proteins of AT in hybrid constructs.

However, it is unknown whether the tissue-specific composition and architecture of ECM scaffolds are necessary to maintain the phenotype and three-dimensional arrangement of cells compared with immature matrixes with different compositions (36). For this reason, we decided to use two different protocols for matrix deposition in order to mimic and compare a specific matrix produced by differentiated adipocytes to a stromal matrix deposited by proliferating stromal cells. Despite their different compositions, the matrices showed similar adipoinductive effect on hASC in the absence of any growth factor. Here we proved that our material has an intrinsic adipoinductive potential, probably because of its mechanical properties resembling the one of native adipose tissue. Interestingly, decorating our scaffold with adipose decellularized ECM we further enhanced the adipoinductive potential, as it is clear from the gene expression analysis. Indeed, late marker of adipogenic differentiation was found to be upregulated in the hybrid constructs rather than in the nude OPAAF. In addition, we observed a strong increase in adipose tissue infiltration in the hybrid construct compared to the nude OPAAF *in vivo*. These results are in line with previous works reporting the adipoinductive effect of adipose ECM (11, 18, 38). On the other hand, we didn't observe differences in the adipoinductive potential of the two matrixes deposited. We presume that other key factors secreted specifically by hASCs could be involved in the adipogenic commitment. Further experiments will be needed to elucidate the mechanism and the factors involved in the adipogenic commitment.

The use of autologous tissue for breast reconstruction is ideal, being the fat tissue itself a source of stem cells, ECM and growth factors (1). Unfortunately, the use of the fat grafting technique is still hampered by the volume loss issue (1, 5). Our system provides an alternative solution to the fat grafting technique exploiting the potential of hASCs for matrix and growth factors production. Decorating a synthetic scaffold instead of directly using fat tissue would overcome the problems related to volume resorption, providing the mechanical support needed in the first phase of tissue regeneration together with an adipoinductive environment for the infiltration and commitment of host cells.

4.5 Conclusion

The developed hybrid ECM-OPAAF regulated hASCs adipogenic commitment *in vitro* together with adipose tissue infiltration *in vivo*. Our approach is an

alternative strategy to be exploited for adipose tissue reconstruction, bridging the knowledge of synthetic and natural biomaterials. The use of bioreactors will potentially streamline the manufacturing process and provide standardized, clinically compliant and cost-effective products. Our hybrid ECM-OPAAF could also be used as 3D model to investigate the complex interplay between cells and ECM in adipose tissue development and homeostasis.

4.6 REFERENCES

1. Combellack EJ, Jessop ZM, Naderi N, Griffin M, Dobbs T, Ibrahim A, et al. Adipose regeneration and implications for breast reconstruction: update and the future. (2227-684X (Print)).
2. Tachi M, Yamada A. Choice of flaps for breast reconstruction. (1341-9625 (Print)).
3. Wu LC, Bajaj A Fau - Chang DW, Chang Dw Fau - Chevray PM, Chevray PM. Comparison of donor-site morbidity of SIEA, DIEP, and muscle-sparing TRAM flaps for breast reconstruction. (1529-4242 (Electronic)).
4. Ross RJ, Shayan R Fau - Mutimer KL, Mutimer Kl Fau - Ashton MW, Ashton MW. Autologous fat grafting: current state of the art and critical review. (1536-3708 (Electronic)).
5. Toyserkani NM, Quaade ML, Sorensen JA. Cell-Assisted Lipotransfer: A Systematic Review of Its Efficacy. (1432-5241 (Electronic)).
6. Chan CW, McCulley Sj Fau - Macmillan RD, Macmillan RD. Autologous fat transfer--a review of the literature with a focus on breast cancer surgery. (1878-0539 (Electronic)).
7. Eto H, Kato H Fau - Suga H, Suga H Fau - Aoi N, Aoi N Fau - Doi K, Doi K Fau - Kuno S, Kuno S Fau - Yoshimura K, et al. The fate of adipocytes after nonvascularized fat grafting: evidence of early death and replacement of adipocytes. (1529-4242 (Electronic)).
8. Bellas E, Panilaitis BJ, Glettig DL, Kirker-Head CA, Yoo JJ, Marra KG, et al. Sustained volume retention in vivo with adipocyte and lipoaspirate seeded silk scaffolds. Biomaterials. 2013;34(12):2960-8.
9. Cheung HK, Han TT, Marecak DM, Watkins JF, Amsden BG, Flynn LE. Composite hydrogel scaffolds incorporating decellularized adipose tissue for soft tissue engineering with adipose-derived stem cells. Biomaterials. 2014;35(6):1914-23.

10. Choi JH, Gimble JM, Lee K, Marra KG, Rubin JP, Yoo JJ, et al. Adipose tissue engineering for soft tissue regeneration. Tissue engineering Part B, Reviews. 2010;16(4):413-26.

11. Flynn LE. The use of decellularized adipose tissue to provide an inductive microenvironment for the adipogenic differentiation of human adipose-derived stem cells. Biomaterials. 2010;31(17):4715-24.

12. Stillaert FB, Di Bartolo C, Hunt JA, Rhodes NP, Tognana E, Monstrey S, et al. Human clinical experience with adipose precursor cells seeded on hyaluronic acid-based spongy scaffolds. Biomaterials. 2008;29(29):3953-9.

13. Wittmann K, Dietl S, Ludwig N, Berberich O, Hoefner C, Storck K, et al. Engineering vascularized adipose tissue using the stromal-vascular fraction and fibrin hydrogels. Tissue engineering Part A. 2015;21(7-8):1343-53.

14. Badylak SF. The extracellular matrix as a biologic scaffold material. Biomaterials. 2007;28(25):3587-93.

15. Badylak SF, Freytes Do Fau - Gilbert TW, Gilbert TW. Extracellular matrix as a biological scaffold material: Structure and function. (1878-7568 (Electronic)).

16. Bissell Mj Fau - Hall HG, Hall Hg Fau - Parry G, Parry G. How does the extracellular matrix direct gene expression? (0022-5193 (Print)).

17. Ingber D. Extracellular matrix and cell shape: potential control points for inhibition of angiogenesis. (0730-2312 (Print)).

18. Flynn LE, Prestwich GD, Semple JL, Woodhouse KA. Proliferation and differentiation of adipose-derived stem cells on naturally derived scaffolds. Biomaterials. 2008;29(12):1862-71.

19. Han TT, Toutounji S, Amsden BG, Flynn LE. Adipose-derived stromal cells mediate in vivo adipogenesis, angiogenesis and inflammation in decellularized adipose tissue bioscaffolds. Biomaterials. 2015;72:125-37.

20. Mano JF, Silva GA, Azevedo HS, Malafaya PB, Sousa RA, Silva SS, et al. Natural origin biodegradable systems in tissue engineering and regenerative medicine: present status and some moving trends. Journal of the Royal Society, Interface / the Royal Society. 2007;4(17):999-1030.

21. Drury JL, Mooney DJ. Hydrogels for tissue engineering: scaffold design variables and applications. Biomaterials. 2003;24(24):4337-51.

22. Martello F, Tocchio A, Tamplenizza M, Gerges I, Pistis V, Recenti R, et al. Poly(amido-amine)-based hydrogels with tailored mechanical properties and degradation rates for tissue engineering. Acta Biomater. 2014;10(3):1206-15.

23. Tocchio A, Martello F, Tamplenizza M, Rossi E, Gerges I, Milani P, et al. RGD-mimetic poly(amidoamine) hydrogel for the fabrication of complex cell-laden micro constructs. Acta Biomater. 2015.

24. Rossi E, Gerges I, Tocchio A, Tamplenizza M, Aprile P, Recordati C, et al. Biologically and mechanically driven design of an RGD-mimetic macroporous foam for adipose tissue engineering applications. (1878-5905 (Electronic)).

25. Mehrkens A, Di Maggio N, Gueven S, Schaefer D, Scherberich A, Banfi A, et al. Non-adherent mesenchymal progenitors from adipose tissue stromal vascular fraction. Tissue engineering Part A. 2014;20(5-6):1081-8.

26. Wendt D, Marsano A, Jakob M, Heberer M, Martin I. Oscillating perfusion of cell suspensions through three-dimensional scaffolds enhances cell seeding efficiency and uniformity. Biotechnology and bioengineering. 2003;84(2):205-14.

27. Sadr N, Pippenger BE, Scherberich A, Wendt D, Mantero S, Martin I, et al. Enhancing the biological performance of synthetic polymeric materials by decoration with engineered, decellularized extracellular matrix. Biomaterials. 2012;33(20):5085-93.

28. Pittenger MF, Mackay Am Fau - Beck SC, Beck Sc Fau - Jaiswal RK, Jaiswal Rk Fau - Douglas R, Douglas R Fau - Mosca JD, Mosca Jd Fau - Moorman MA, et al. Multilineage potential of adult human mesenchymal stem cells. (0036-8075 (Print)).

29. Zebisch K, Voigt V, Wabitsch M, Brandsch M. Protocol for effective differentiation of 3T3-L1 cells to adipocytes. Analytical biochemistry. 2012;425(1):88-90.

30. Hausman DB, DiGirolamo M Fau - Bartness TJ, Bartness Tj Fau - Hausman GJ, Hausman Gj Fau - Martin RJ, Martin RJ. The biology of white adipocyte proliferation. (1467-7881 (Print)).

31. MacDougald OA, Mandrup S. Adipogenesis: forces that tip the scales. (1043-2760 (Print)).

32. Gregoire FM SC, and Sul HS. Understanding Adipocyte Differentiation. American Physiology Society. 1998.

33. Ikuyo Nakajima TYKO, Hisashi Aso. Adipose tissue extracellular matrix: newly organized by adipocytes during differentiation. Differentiation. 1998.

34. Papadimitropoulos A, Scherberich A Fau - Guven S, Guven S Fau - Theilgaard N, Theilgaard N Fau - Crooijmans HJA, Crooijmans Hj Fau - Santini F, Santini F Fau - Scheffler K, et al. A 3D in vitro bone organ model using human progenitor cells. (1473-2262 (Electronic)).

35. Caliari SR, Burdick JA. A practical guide to hydrogels for cell culture. (1548-7105 (Electronic)).

36. Swinehart IT, Badylak SF. Extracellular matrix bioscaffolds in tissue remodeling and morphogenesis. (1097-0177 (Electronic)).

37. Comley K, Fleck NA. A micromechanical model for the Young's modulus of adipose tissue. International Journal of Solids and Structures. 2010;47(21):2982-90.

38. Yu C, Bianco J, Brown C, Fuetterer L, Watkins JF, Samani A, et al. Porous decellularized adipose tissue foams for soft tissue regeneration. Biomaterials. 2013;34(13):3290-302.

CHAPTER 5

5 CONCLUSION AND FUTURE PERSPECTIVES

Eleonora Rossi [a,b]

a) SEMM, European School of Molecular Medicine, Campus IFOM-IEO, Via Adamello 16, 20139 Milano, Italy. b) Department of Biomedicine, University Hospital of Basel, Hebelstrasse 20, 4031 Basel, Switzerland.

In this PhD thesis we have developed an alternative strategy for adipose tissue reconstruction.

We focused our attention on a synthetic class of polymers, the RGD-mimetic PAA, because of their promising cell-adhesive properties and chemical tunability. We first designed and investigated the potential of RGD-mimetic PAA based hydrogels for 3D *in vitro* cell culture. To this aim, we exploited two different approaches for the fabrication of hydrogels with tunable mechanical and degradation properties. In the first approach, the RGD-mimetic PAA oligomers were conjugated with Jeffamine® generating the triblock copolymer PJP. In the second approach, PAA was combined by grafting with a new polymeric precursor, the P(HEMA-co-APM), to obtain hydrogels matching the adhesive properties of PAA with the mechanical integrity of PHEMA. We demonstrated that with our approaches it is possible to tune the mechanical features of our hydrogels keeping the adhesive properties typical of PAA.

Mechanical stimuli and cell adhesion signals are two key parameters in the complex interplay between cells and ECM *in vivo*. Therefore, we decided to fabricate a porous scaffold resembling the mechanical cues of adipose tissue while preserving the biological properties of PAA. PAA oligomers were formed into soft scaffolds with hierarchical porosity through a combined free radical polymerization and foaming reaction. Our study showed that OPAAF is able to support *in vitro* the growth of several cell types together with the adipogenic differentiation of preadipose cells, and *in vivo* the infiltration of fat and vascular tissue.

In order to further engineer the OPAAF, we decided to decorate it with devitalized adipose matrix deposited by hASCs obtaining a hybrid scaffold ECM-OPAAF. Two different protocols have been adopted for the decoration, in order to

investigate the role of a differentiated and stromal matrix in adipogenic induction. With our approach we efficiently generated hybrid scaffolds combining the positive features of both synthetic and natural biomaterials. Our system proved to be efficient in preserving the structural and biological composition of the ECM deposited. Furthermore, the developed hybrids ECM-OPAAF showed to regulate hASCs adipogenic commitment *in vitro* together with adipose tissue infiltration *in vivo*.

hASCs are known to play an immunomodulatory role through the secretion of growth factors and cytokines. In this scenario, a detailed analysis of Adipo- and Stromal-ECM composition would be highly relevant in order to define possible differences in the deposited ECM and implications in the regenerative processes. Therefore, further studies are needed to evaluate the *in vivo* adipoinductive potential of the hybrids together with the host inflammatory response and tissue remodeling in time.

Overall, the reported results have important implications in adipose tissue engineering, especially in the design of an alternative approach for breast reconstruction. The volume retention in adipose tissue reconstruction is still a crucial aspect. Therefore, synthetic scaffolds as OPAAF can overcome this problem offering a stable mechanical support and controllable degradation rate. Furthermore the decoration with devitalized adipose ECM can bridge the gap between synthetic and natural materials combining mechanical support and adipogenic stimuli fundamental for hASCs recruitment and differentiation.

A successful implementation of this study might pave the way towards the use of an alternative strategy for adipose tissue reconstruction based on the use of patients cells for the generation of custom made hybrid scaffolds. At the same time the hybrid ECM-OPAAF could be an interesting *in vitro* model to understand signals and conditions relevant for fat tissue development. Ultimately, the *in vitro* bioreactor system could provide a useful platform to test the effect of compounds involved in regulation of fat tissue homeostasis.

APPENDIX

6 A 3D IN VITRO BONE MODEL FOR THE INVESTIGATION OF THE ROLE OF TRIGGERING RECEPTOR EXPRESSED ON MYELOID CELLS 2 (TREM-2) IN BONE HOMEOSTASIS

Eleonora Rossi [a] et al.

a) Department of Biomedicine, University Hospital of Basel, Hebelstrasse 20, 4031 Basel, Switzerland.

This work was carried on in collaboration with Roche Pharmaceuticals, Basel, Switzerland.

6.1 INTRODUCTION

TREM-2 is a transmembrane immunoglobulin-like receptor expressed by different myeloid cells, including microglia, macrophages, dendritic cells and (pre-)osteoclasts (1, 2). In the central nervous system (CNS) TREM-2 is fundamental for microglial cells phagocytosis and regulation of the inflammatory response (3-5). In humans, missense mutations in TREM-2 gene significantly increase susceptibility for late-onset of Alzheimer's disease (AD) (6-9). Recent experimental studies showed that TREM-2 may play a protective role in AD by suppressing inflammatory responses as well as promoting phagocytosis of damaged neurons and removal of extracellular neurotic plaques containing amyloid-beta peptides (3, 9-11). Furthermore, TREM-2 has been shown to promote several microglial functions in response to amyloid-beta peptides deposition (9, 11, 12). Based on the potential protective actions of TREM-2 in AD pathogenesis, targeting TREM-2 may provide new opportunities for AD diagnosis and treatment.

TREM-2 also plays a pivotal role in bone homeostasis, being a crucial regulator of osteoclastogenesis (13). Complete loss-of-function of TREM-2 results also in a rare syndrome called Nasu-Hakola disease (NHD), that is characterized by bone cysts and presenile dementia (14). In cells isolated from these patients, osteoclasts (OC) differentiation is dramatically arrested, resulting in large aggregates of immature OCs, that exhibit impaired bone resorptive activity (15). *In-vitro*, knock-down of TREM-2 impairs proliferation and beta-catenin activation in OC

precursors in response to macrophage colony-stimulating factor (13). Investigations of the molecular mechanisms confirmed that, through cross-talk between osteoblastic and osteoclastic cells, effective osteoclastogenesis requires functional TREM-2-DAP12, which cooperates with RANK to induce intracellular calcium signaling and additional downstream effectors that are required for OCs differentiation.

In contrast to the numerous loss-of-function studies, it is currently unknown whether and how gain-of-function of TREM-2 affects bone homeostasis. This is likely related to the fact that the nature of endogenous TREM-2 ligand(s) is still elusive (9, 16). However, considering the therapeutic strategy to agonize TREM-2-mediated signalling for neuroprotection, it would be of highest relevance to identify the TREM-2 ligand and assess the effect of TREM-2 over-activation on the differentiation of myeloid precursors into functional multinucleated OCs and bone homeostasis.

In order to investigate the mechanisms underlying physiological and pathological cellular processes in bone, animal models are often considered not satisfactory. In fact, in addition to the high costs and large degree of systemic complexity, they often do not faithfully recapitulate the biological programs specific of the human species and fail to be predictive of a clinical outcome (17). In this context, it appears that while human TREM-2 activates osteoclastogenesis, mouse TREM-2 has an inhibitory role in the formation of OCs (16).

3D organotypic culture models based on human cells may provide an alternative solution to this issue, reducing the use of complex and costly animal models, while providing a more physiological outcome. Several *in vitro* models have been proposed to mimic the process of bone turnover using human progenitors (18, 19). Current models for the study of TREM-2 pathway are mainly relying on *in vivo* mouse model or 2D cell culture (3, 6, 13). A model able to recapitulate the complex interplay between OBs and OCs and TREM-2 role in this scenario is still missing.

While targeting TREM-2 may provide new opportunities for AD diagnosis and treatment, it is relevant to assess the effect of over-activation in bone homeostasis. Towards this aim, here we established a perfusion based 3D model using human progenitors differentiated into OBs and OCs. Cells were cultured in perfusion on collagen type I scaffold in order to allow a long-term cell culture and to achieve

bone-like matrix deposition. ECM turnover was monitored over time together with TREM2 expression in OCs.

6.2 Materials and Methods

6.2.1 Cell source and expansion

Bone marrow aspirates were obtained from the iliac crest of healthy donors during routine orthopedic surgical procedures, in accordance with the local ethical committee (University Hospital Basel) and subsequent to informed consent. Nucleated cells were isolated from aspirates by means of red blood cells lyses buffer (pH 7.2) containing 0.15 M NH_4Cl, 1 mM $KHCO_3$ (SigmaeAldrich, USA) and 0.1 mM Na_2EDTA (Fluka, Switzerland). Freshly isolated cells were plated at a density of $1*10^5$ nucleated cells/cm2. Cell expansion was carried out in complete medium (CM) which consisted of a-Modified Eagle's Medium, 10% fetal bovine serum, 100 mM HEPES buffer solution, 1 mM sodium pyruvate, 100 U/ml penicillin, 100 mg/ml streptomycin and 292 mg/ml L-glutamine (GIBCO, Switzerland) supplemented with 100 nM dexamethasone (SigmaeAldrich, USA) and 5 ng/ml fibroblast growth factor-2 (FGF-2; R&D systems, USA). Medium was changed twice a week. At confluence, bone marrow-derived hMSC were replated for expansion (seeding density of $3*10^3$ cells/cm^2). Upon confluence, cells were enzymatically retrieved and counted for use in the following experiments.

6.2.2 Peripheral blood derived CD14+ monocytes

Mononuclear cells were isolated from human peripheral blood buffy coats from healthy donors (different from bone marrow donors) by gradient centrifugation (Ficoll, Histopaque 1077, Sigma-Aldrich, St. Louis, MO, USA). Subsequently, CD14+ monocytes were sorted using anti-CD14-coated magnetic beads (Miltenyi Biotec, Auburn, CA, USA), according to the manufacturer's instructions.

6.2.3 3D co-culture system

3D co-cultures were established using a perfusion bioreactor system, previously developed for cell seeding and cultivation into 3D scaffolds (18, 20) following a two-phase strategy, as shown in Fig. 1. In the first phase, $3x10^6$ hBMCs resuspended in 8 mL of *complete medium* were perfused through 6 mm diameter,

1.5 mm thick disks of collagen type I crosslinked scaffold (Optimaix®). hBMCs were perfused overnight through the scaffolds at a superficial velocity of 1000 mm/s. After 24 h (cell seeding phase), the superficial velocity was reduced to 100 mm/s for perfusion culture. Cells were differentiated for 3 weeks in osteogenic medium (OM), which consists in a-MEM CM supplemented with 10nM Dexametasone, 0.1 mM L-ascorbic acid-2-phosphate and 10 mM ß-glycerophosphate. In the second phase, $3x10^6$ freshly isolated CD14+ monocytes were seeded into each osteogenic construct at a superficial velocity of 400 μm/s. Cells were then cultured for further 3 weeks in the presence of CM supplemented with macrophage colony-stimulating factor (MCSF, 25 ng/ mL, R&D systems, Minneapolis, MN, USA), to promote adhesion and proliferation of monocytes and receptor activator for κB factor ligand (RANK-ligand, 50 ng/ mL, R&D systems) to promote osteoclast differentiation (*osteoclastogenic medium*) and refreshed every 4 days for an additional period of 21 days at a superficial velocity of 100 μm/s (the total culture time for phases 1 and 2 was 42 days).

6.2.4 In vitro functionality of the 3D co-culture system

6.2.4.1 Cytofluorimetric analysis

At the end of each time point of the second phase, cells were extracted by substituting the CM with a solution of 0.3% collagenase (collagenase) and perfusing the constructs for 40 min followed by 0.05% trypsin/0.53 mM EDTA solution (trypsin) for additional 15 min both at 400 mm per second. The fraction of dead cells, preliminarily assessed by assessed by Trypan blue exclusion (Sigma, Switzerland). The resulting cells were rinsed and incubated at 4°C for 30 minutes with antibodies against human CD14 and TREM-2 (BD Bioscience). Cells were then analyzed using an Accuri flow cytometer (BD Bioscience).

6.2.4.2 Supernatant analysis

Prior to each medium refresh, the media were collected, centrifuged at 400 g for 5 min and the resulting supernatant stored at -20 °C. The samples were then thawed and assessed for C-terminus procollagen type I (CICP), crosslinked N-telopeptides of collagen type I (NTx-I, Osteomark® NTx Serum), (both from TecoMedical Group, Sissach, Switzerland), tartrate-resistant acid phosphatase isoform 5b (TRAP5b, BoneTRAP® Immunodiagnostic Systems, Boldon Business Park, UK), shed-TREM-2 (Roche Pharmaceuticals, Basel, Switzerland) and

phosphate levels (BioVision, USA). Each assay was performed according to the manufacturers' instructions.

6.2.4.3 HISTOLOGICAL STAINING AND IMMUNOHISTOCHEMISTRY

After *in vitro* culture, constructs were fixed in 4% paraformaldehyde and embedded in paraffin. Sections (8 μm thick) were stained for Haematoxylin and Eosin (H&E) (J.T. Baker/Avantor, Philipsburg, NJ, USA), for Alizarin Red, for Masson's Trichrome and for TRAP activity using the leukocyte acid phosphatase kit (Sigma-Aldrich). Immunohistochemical analysis was performed to assess the composition of ECM human bone sialoprotein (BSP; Enzo Life Sciences, Exeter, U.K.). The immunobinding was detected with biotinylated secondary antibodies and using the appropriate Vectastain ABC kits (Vector Labs, Burlingame, CA, USA). The red signal was developed with the Fast Red kit (Dako Cytomation, Glostrup, Denmark) and sections counterstained by Haematoxylin. Negative controls were performed for each analysis by omitting the primary antibodies. Histological and immunohistochemical sections were analysed using an Olympus BX-63 microscope (Olympus, Tokyo, Japan).

6.2.5 STIMULATION WITH TREM-2 AGONIST

In order to preliminarily evaluate the effect of TREM-2 over-activation on bone metabolism, the 3D co-culture system was stimulated with a TREM-2 agonist (Roche Pharmaceuticals, Basel, Switzerland). The agonist was used at 5ug/mL concentration and cells were stimulated for 12 hours. Supernatants were collected and assessed for CICP, NTX-I, TRAP5b, shTREM-2 and phosphate levels.

6.2.6 STATISTICAL ANALYSES

All values are presented as mean ± standard deviation. Differences between experimental groups were statistically assessed using one-way ANOVA tests. $P < 0.05$ was considered to indicate statistically significant differences.

6.3 RESULTS

6.3.1 ESTABLISHMENT OF THE 3D CO-CULTURE SYSTEM

In order to generate a 3D co-culture system, osteoblastic and osteoclastic progenitors derived from human bone marrow and peripheral blood were sequentially loaded into porous collagen-based scaffolds using a perfusion-based bioreactor system, as described in the Materials and Methods section and

graphically illustrated in figure 6-1.

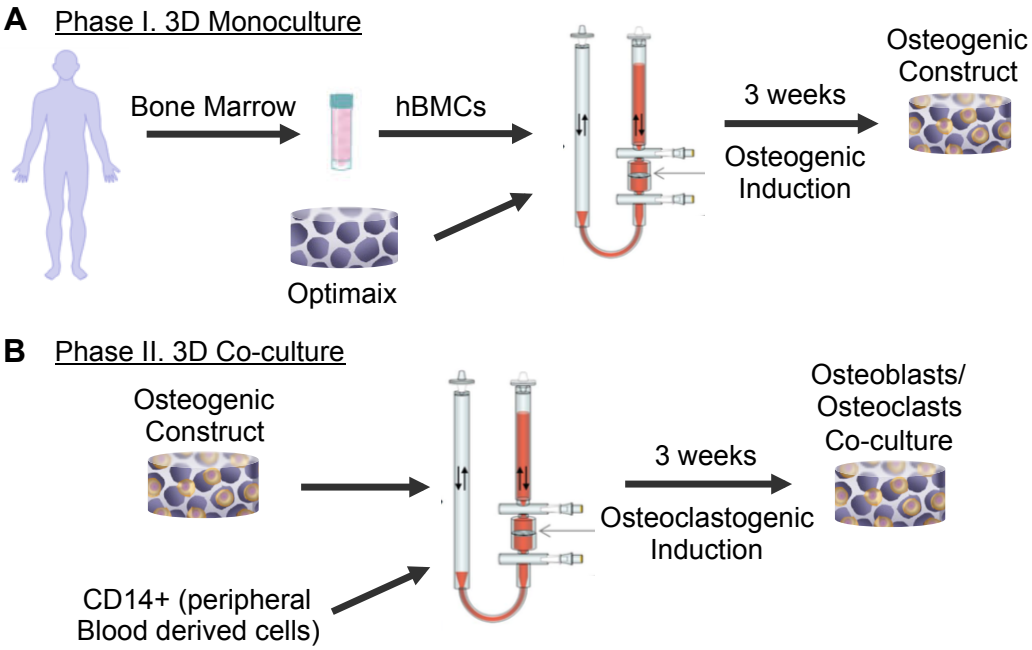

Figure 6-1 3D co-culture system. hBMCs seeding and differentiation in osteogenic medium (A). CD14+ cells seeding and differentiation in osteoclastogenic medium on the osteogenic construct (B).

In details, hBMCs were seeded and cultured in osteogenic medium for 3 weeks in order to obtain an osteogenic construct (Figure 6-1 A). In a second phase the osteogenic construct was seeded with CD14+ cells from peripheral blood and cells were cultured in osteoclastogenic medium for 3 weeks (Figure 6-1 B). As evidenced from the histological analysis, after the first phase we obtained a tissue-like construct in which ECM rich in collagen (Figures 6-2 A and E) was deposited. hBMCs differentiated into osteoblast as assessed by immunohistochemical analysis for BSP (Figures 6-3 E-H) and deposited a mineralized matrix (Figures 6-3 A-D). The state of the co-culture system was monitored over time by histological analysis for ECM (Figures 6-2 A-F), mineralized matrix (Figures 6-3 A-D), osteoblasts and osteoclasts differentiation (Figures 6-3 E-H and 6-4 A-F, respectively). Histological analysis of the 3D model confirmed the stability of the co-culture system.

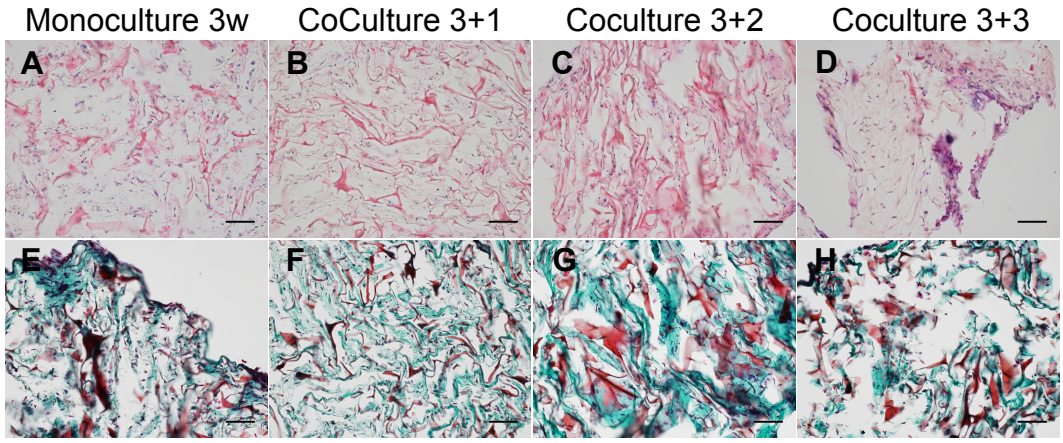

Figure 6-2 Histological analysis for ECM deposition. H&E staining for the monoculture with hBMCs (A) and for the co-culture over time (B-D). Masson's trichrome staining for the monoculture (E) and for the co-culture (F-H). Scale bars 50 μm.

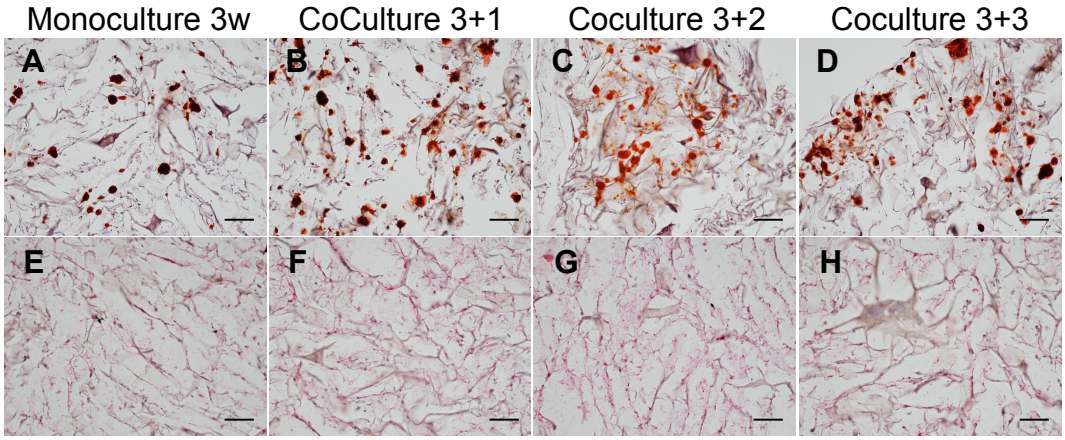

Figure 6-3 Histological analysis for osteogenic construct. Alizarin red staining for the monoculture with hBMCs (A) and for the co-culture over time (B-D). BSP immunohistochemistry for the monoculture (E) and for the co-culture (F-H). Scale bars 50 μm.

6.3.2 Evaluation of osteoclast differentiation and TREM-2 monitoring

CD14+ cells differentiation into OCs was monitored over time up to 3 weeks of co-culture. OCs distribution was investigated by TRAP staining (Figures 6-4 A-F) while their activity was assessed quantitatively by TRAP5b isoenzyme analysis (Figure 6-5 C). TREM-2 positive cells were detected by FACS analysis up to 2 weeks of co-culture (Figures 6-4 G and H). The detection of TREM-2 positive cells by FACS analysis was no longer possible at the third week of co-culture. This result is due to difficulties in cells retrieval caused by their embedding in the matrix. Overall, these results supported the stability of the co-culture system providing a tool for the detection of TREM-2 positive cells and distribution of

TRAP positive OCs.

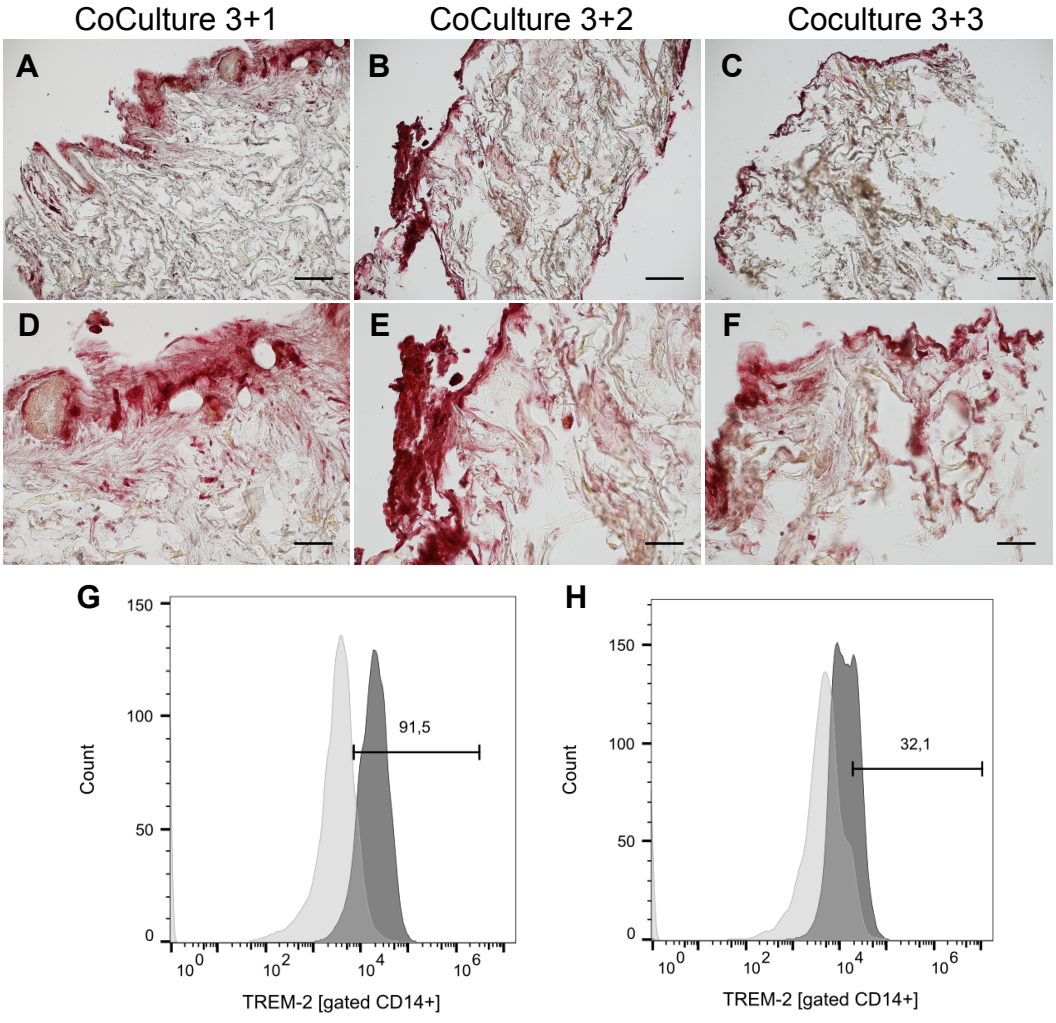

Figure 6-4 Analysis of OCs differentiation and TREM-2 levels. TRAP staining for OCs activity over time (A-F). TREM-2 FACS analysis at 1 (G) and 2 weeks (H) of co-culture. Scale bars 100 μm for images A-C; scale bars 50 μm for images D-F.

6.3.3 Assessment of ECM turnover using non-invasive tools

In order to non-invasively monitor the process of ECM deposition and resorption over culture time, typical markers of bone remodelling were assessed in the supernatant. Increasing levels of procollagen-I (CICP) were measured at different time points, indicating active and sustained deposition of ECM by mesenchymal/osteoblastic cells (Figure 6-5 A). The levels of NTX-I, increased with time indicating osteoclast-driven degradation product of Col-I (Figure 6-5 B). The production of procollagen-I (CICP) increased over time, indicating active ECM synthesis (Figure 6-5 A). Levels of the isoenzyme TRAP5b increased with culture time up to 2 weeks of co-culture, indicating an increase in the number of OCs (Figure 6-5 C). Surprisingly, levels of sTREM-2 increased with time

following the same trend of TRAP5b and NTX-I indicating the possible role of TREM-2 receptor in osteoclastogenic differentiation and ECM resorption. A reduction in the levels of NTX-I, TRAP5b and sTREM-2 was observed after 2 weeks of co-culture (Figures 6-5 B-D).

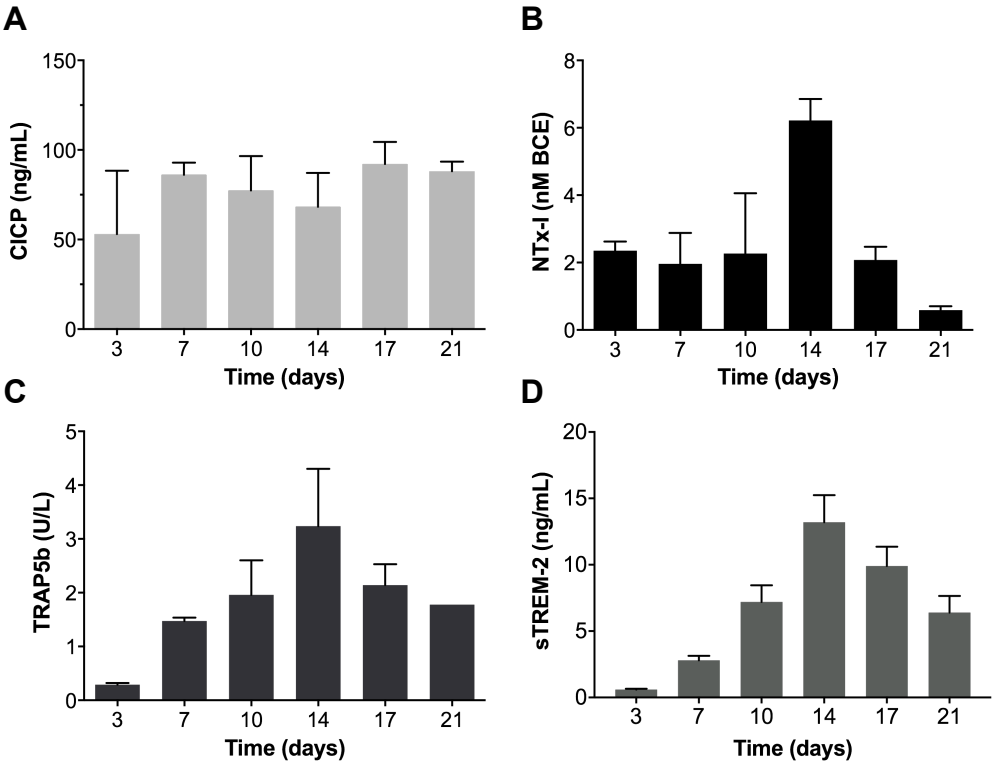

Figure 6-5 ECM turnover in the co-culture system. Supernatant analysis for CICP (A), NTX-I (B), TRAP5b (C) and sTREM-2 (D) up to 3 weeks of co-culture.

6.3.4 3D CO-CULTURE STIMULATION WITH TREM-2 AGONIST

Once established the 3D model, together with the non-invasive tools for the analysis, we preliminarily stimulated the model with a TREM-2 agonist provided by Roche Pharmaceuticals. Starting from the data obtained by ELISA analysis for TRAP5b and sTREM-2, we defined a window for OCs stimulation at 6 days of co-culture. We stimulated the system for 12 hours and we subsequently analyzed ECM turnover. No relevant effect was observed on collagen deposition and resorption (Figures 6-6 A and B). We also investigated the possible degradation of inorganic matrix components by phosphate levels analysis. Phosphate levels in supernatants increased in response to TRAP5b activity (Figures 6-6 C and D) without differences between the agonist stimulation and the control condition. These results provide a proof of principle of the applicability of our 3D co-culture system for the investigation of TREM-2 agonists effect on bone metabolism and

ECM turnover.

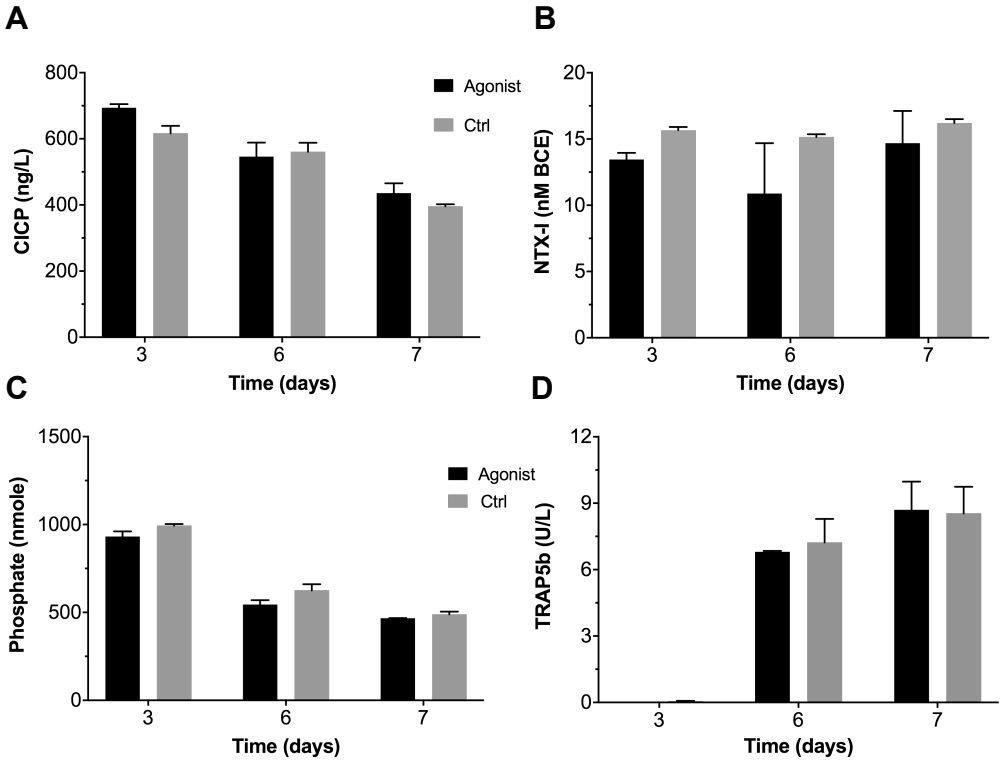

Figure 6-6 ECM turnover after stimulation with the agonist. Supernatant analysis for CICP (A), NTX-I (B), phosphate levels (C) and TRAP5b (D).

6.4 DISCUSSION

In this work we established a 3D co-culture model starting from human progenitors differentiated into OCs and OBs. Our goal was to create a system for the investigation of TREM-2 role in bone homeostasis to be used as a possible platform for drug testing. This model efficiently recapitulated the interplay between OCs and OBs, providing a tool for the monitoring of TREM-2 in its transmembrane and shed form.

Current models for the investigation of TREM-2 role on bone homeostasis are relying on *in vitro* 2D cell cultures of OCs and *in vivo* knockout mouse models (3, 4, 6, 11). *In vitro* 2D cultures are failing to recapitulate the ECM turnover occurring *in vivo*, while *in vivo* models are usually not suitable for the investigation of specific ligands and pathways (3-5, 17). We reported for the first time a 3D bone-like model with OBs and OCs for the investigation of TREM-2 role in bone homeostasis. The use of human cell sources can provide a more

physiological environment for the study of TREM-2 offering also the possibility of testing drugs in a donor specific manner.

TREM-2 is composed of a single extracellular immunoglobulin-like domain, one transmembrane domain and a short cytoplasmic tail (9). The soluble form of TREM-2 can originate by shedding of the receptor extracellular portion or by alternative splicing of TREM-2 transcript leading to secretion (2, 21). Recent study investigating the effect of a chimeric TREM-2 protein on OCs reported interference in osteoclastogenesis (22). Although the role of sTREM-2 is still unknown, a possible mechanism of action has been proposed in which sTREM-2 would act to counter-regulate the receptor activity by binding the endogenous ligand (21, 22). This hypothesis would explain also the sTREM-2 profile that we observed, with a progressive increase in response to OCs activity and a subsequent reduction. Moreover, the sTREM-2 might also be responsible of the absence of effect that we observed after the stimulation with the agonist. Further studies are needed in order to elucidate the possible mechanism underlying the role of sTREM-2 in OCs activity and ECM turnover.

TREM-2 has emerged as a possible promising pathway to explore for diagnosis and treatment of AD (9). Unfortunately, the endogenous ligand of this receptor is still unknown and available 2D and *in vivo* models are lacking in addressing this issue. We believe that this *in vitro* 3D model would provide a useful tool for the investigation of the endogenous ligand and the role of the soluble form taking in account the complex interplay between OCs and OBs.

6.5 Conclusion

Before TREM-2 can be considered as a potential target for AD treatment, its role in bone homeostasis has to be elucidated. Here we present a 3D *in vitro* bone model based on the co-culture of OBs and OCs in an engineered bone-like environment. Our model recapitulates the dynamic interplay of bone components, providing a useful tool to study the effect of the TREM-2 pathway on bone homeostasis.

6.6 References

1. Bouchon A, Hernandez-Munain C Fau - Cella M, Cella M Fau - Colonna M, Colonna M. A DAP12-mediated pathway regulates expression of CC

chemokine receptor 7 and maturation of human dendritic cells. (0022-1007 (Print)).

2. Schmid CD, Sautkulis Ln Fau - Danielson PE, Danielson Pe Fau - Cooper J, Cooper J Fau - Hasel KW, Hasel Kw Fau - Hilbush BS, Hilbush Bs Fau - Sutcliffe JG, et al. Heterogeneous expression of the triggering receptor expressed on myeloid cells-2 on adult murine microglia. (0022-3042 (Print)).

3. Kleinberger G, Yamanishi Y, Suarez-Calvet M, Czirr E, Lohmann E, Cuyvers E, et al. TREM2 mutations implicated in neurodegeneration impair cell surface transport and phagocytosis. (1946-6242 (Electronic)).

4. Poliani Pl Fau - Wang Y, Wang Y Fau - Fontana E, Fontana E Fau - Robinette ML, Robinette Ml Fau - Yamanishi Y, Yamanishi Y Fau - Gilfillan S, Gilfillan S Fau - Colonna M, et al. TREM2 sustains microglial expansion during aging and response to demyelination. (1558-8238 (Electronic)).

5. Yuan P, Condello C, Keene CD, Wang Y, Bird TD, Paul SM, et al. TREM2 Haplodeficiency in Mice and Humans Impairs the Microglia Barrier Function Leading to Decreased Amyloid Compaction and Severe Axonal Dystrophy. (1097-4199 (Electronic)).

6. Guerreiro R, Wojtas A Fau - Bras J, Bras J Fau - Carrasquillo M, Carrasquillo M Fau - Rogaeva E, Rogaeva E Fau - Majounie E, Majounie E Fau - Cruchaga C, et al. TREM2 variants in Alzheimer's disease. (1533-4406 (Electronic)).

7. Jiang T, Yu Jt Fau - Zhu X-C, Zhu Xc Fau - Tan L, Tan L. TREM2 in Alzheimer's disease. (1559-1182 (Electronic)).

8. Jonsson T, Stefansson H Fau - Steinberg S, Steinberg S Fau - Jonsdottir I, Jonsdottir I Fau - Jonsson PV, Jonsson Pv Fau - Snaedal J, Snaedal J Fau - Bjornsson S, et al. Variant of TREM2 associated with the risk of Alzheimer's disease. (1533-4406 (Electronic)).

9. Colonna M, Wang Y. TREM2 variants: new keys to decipher Alzheimer disease pathogenesis. (1471-0048 (Electronic)).

10. Hickman SE, El Khoury J. TREM2 and the neuroimmunology of Alzheimer's disease. (1873-2968 (Electronic)).

11. Wang Y, Ulland TK, Ulrich JD, Song W, Tzaferis JA, Hole JT, et al. TREM2-mediated early microglial response limits diffusion and toxicity of amyloid plaques. (1540-9538 (Electronic)).

12. Yaghmoor F, Noorsaeed A, Alsaggaf S, Aljohani W, Scholtzova H, Boutajangout A, et al. The Role of TREM2 in Alzheimer's Disease and Other Neurological Disorders. LID - 160 [pii]. (2161-0460 (Print)).

13. Otero K, Shinohara M Fau - Zhao H, Zhao H Fau - Cella M, Cella M Fau - Gilfillan S, Gilfillan S Fau - Colucci A, Colucci A Fau - Faccio R, et al. TREM2 and beta-catenin regulate bone homeostasis by controlling the rate of osteoclastogenesis. (1550-6606 (Electronic)).

14. Bianchin MM, Capella Hm Fau - Chaves DL, Chaves Dl Fau - Steindel M, Steindel M Fau - Grisard EC, Grisard Ec Fau - Ganev GG, Ganev Gg Fau - da Silva Junior JP, et al. Nasu-Hakola disease (polycystic lipomembranous osteodysplasia with sclerosing leukoencephalopathy--PLOSL): a dementia associated with bone cystic lesions. From clinical to genetic and molecular aspects. (0272-4340 (Print)).

15. Paloneva J, Mandelin J Fau - Kiialainen A, Kiialainen A Fau - Bohling T, Bohling T Fau - Prudlo J, Prudlo J Fau - Hakola P, Hakola P Fau - Haltia M, et al. DAP12/TREM2 deficiency results in impaired osteoclast differentiation and osteoporotic features. (0022-1007 (Print)).

16. Colonna M, Turnbull I Fau - Klesney-Tait J, Klesney-Tait J. The enigmatic function of TREM-2 in osteoclastogenesis. (0065-2598 (Print)).

17. Pearce AI, Richards Rg Fau - Milz S, Milz S Fau - Schneider E, Schneider E Fau - Pearce SG, Pearce SG. Animal models for implant biomaterial research in bone: a review. (1473-2262 (Electronic)).

18. Papadimitropoulos A, Scherberich A Fau - Guven S, Guven S Fau - Theilgaard N, Theilgaard N Fau - Crooijmans HJA, Crooijmans Hj Fau - Santini F, Santini F Fau - Scheffler K, et al. A 3D in vitro bone organ model using human progenitor cells. (1473-2262 (Electronic)).

19. Tortelli F, Pujic N Fau - Liu Y, Liu Y Fau - Laroche N, Laroche N Fau - Vico L, Vico L Fau - Cancedda R, Cancedda R. Osteoblast and osteoclast differentiation in an in vitro three-dimensional model of bone. (1937-335X (Electronic)).

20. Wendt D, Marsano A, Jakob M, Heberer M, Martin I. Oscillating perfusion of cell suspensions through three-dimensional scaffolds enhances cell seeding efficiency and uniformity. Biotechnology and bioengineering. 2003;84(2):205-14.

21. Piccio L, Buonsanti C Fau - Cella M, Cella M Fau - Tassi I, Tassi I Fau - Schmidt RE, Schmidt Re Fau - Fenoglio C, Fenoglio C Fau - Rinker J, 2nd, et al. Identification of soluble TREM-2 in the cerebrospinal fluid and its association with multiple sclerosis and CNS inflammation. (1460-2156 (Electronic)).

22. Kim Y, Sato K Fau - Asagiri M, Asagiri M Fau - Morita I, Morita I Fau - Soma K, Soma K Fau - Takayanagi H, Takayanagi H. Contribution of nuclear factor of activated T cells c1 to the transcriptional control of immunoreceptor osteoclast-associated receptor but not triggering receptor expressed by myeloid cells-2 during osteoclastogenesis. (0021-9258 (Print)).